National Technical University of Athens

Department of Naval Architecture and Marine Engineering

Laboratory of Ship and Marine Hydrodynamics

Diploma Thesis

Implementation of Algorithm for Modeling of Cavitation in Marine Applications using Computational Fluid Dynamics

---

Georgios Anastasopoulos

Supervised by

Assistant Professor George Papadakis

Athens, July 2022

Abstract

Cavitation is a phenomenon with a series of negative effects for marine propulsion systems, such as erosion, noise, vibrations and performance deterioration. The occurrence of cavitation in these marine applications is certain and thus it has to be accounted for in the design process. In order to improve the understanding of the phenomenon, it is common to carry out experimental tests, which are both challenging to conduct and limited as to the information they can provide regarding this poly parametric and complex phenomenon. Recent technological advances and surge in computational power have constituted numerical simulations of cavitation a very useful tool that can aid the understanding and prediction capability of the phenomenon and play an important role in the design process of a series of marine applications. This thesis focuses on implementing a numerical methodology to simulate and predict the effects of cavitating flow.

Under the present scope, the Eulerian solver MaPFlow that solves the unsteady Reynolds-Averaged Navier-Stokes equations is employed. The objective of the research is the implementation of the Kunz transport equation model for the modeling of mass transfer and the simulation of cavitating flows. To achieve this goal, the Kunz cavitation model is calibrated and validated around a set of two-dimensional hydrofoils. The tuned model is then tested on a three-dimensional hydrofoil and a model scale propeller to further evaluate its accuracy. Pressure distribution, cavitation patterns and their evolution over time, vapor fraction and hydrodynamic characteristics are studied.

The numerical findings compare particularly well with the experimental data for all the different geometries and flows in consideration. The proposed cavitation model calibration documents high accuracy and flexibility, although there are some discrepancies to be found as to the produced cavitation patterns. All in all, the numerical results of the solver MaPFlow are very promising for research regarding cavitation prediction and analysis.

Περίληψη

Η σπηλαίωση είναι ένα φαινόμενο που προκαλεί μια σειρά από μη επιθυμητά αποτελέσματα σε συστήματα ναυτικής πρόωσης, όπως διάβρωση, εκπομπή θορύβου, κραδασμούς και πτώση της απόδοσης. Η εμφάνιση του φαινομένου της σπηλαίωσης σε αυτές τις ναυτικές εφαρμογές είναι δεδομένη και έτσι πρέπει να λαμβάνεται υπόψη κατά τη διαδικασία της σχεδίασης. Για τη βελτίωση της γνώσης περί του φαινομένου μια συνήθης πρακτική είναι η εκτέλεση πειραματικών δοκιμών, οι οποίες είναι τόσο απαιτητικές ως προς την εκτέλεσή τους όσο και περιορισμένες ως προς το εύρος πληροφοριών που μπορούν να παρέχουν σχετικά με αυτό το πολυπαραμετρικό και σύνθετο φαινόμενο. Οι πρόσφατες τεχνολογικές εξελίξεις και η σημαντική αύξηση στη διαθέσιμη υπολογιστική ισχύ έχουν καταστήσει τις αριθμητικές προσομοιώσεις της σπηλαίωσης ως ένα πολύ χρήσιμο εργαλείο που μπορεί να συνεισφέρει σημαντικά στην κατανόηση και ικανότητα πρόβλεψης του φαινομένου και να διαδραματίσει κομβικό ρόλο στην διαδικασία σχεδίασης ενός εύρους ναυτικών εφαρμογών. Η παρούσα διπλωματική εστιάζει στην εφαρμογή μιας αριθμητικής μεθόδου για την προσομοίωση και την πρόβλεψη των αποτελεσμάτων μιας σπηλαιούμενης ροής.

Για αυτόν τον σκοπό, χρησιμοποιείται ο Eulerian επιλυτής MaPFlow που λύνει τις ασταθείς εξισώσεις Reynolds-Averaged Navier-Stokes. Ο στόχος της έρευνας είναι η εισαγωγή του μοντέλου εξίσωσης μεταφοράς για τη μοντελοποίηση μεταφοράς μάζας του Kunz για την προσομοίωση σπηλαιούμενων ροών. Για την επίτευξή του, ρυθμίζονται οι παράμετροι του μοντέλου σπηλαίωσης του Kunz, το οποίο και πιστοποιείται για την περίπτωση δύο δισδιάστατων υδροτομών. Στη συνέχεια, το μοντέλο ελέγχεται ως προς την ακρίβεια των αποτελεσμάτων του για μία τρισδιάστατη υδροτομή και για μια ναυτική έλικα υπό κλίμακα. Κατανομή της πίεσης, οπτικοποίηση της σπηλαίωσης και της εξέλιξής της στο χρόνο, η μάζα του ατμού και υδροδυναμικά χαρακτηριστικά μελετώνται για την εξαγωγή συμπερασμάτων.

Τα αριθμητικά ευρήματα παρουσιάζουν ιδιαίτερα καλή συμφωνία με τα πειραματικά δεδομένα για όλες τις διαφορετικές γεωμετρίες και ροές που εξετάζονται. Η προτεινόμενη ρύθμιση των συντελεστών του μοντέλου σημειώνει υψηλά επίπεδα ακρίβειας και ευελιξίας στις προσομοιώσεις, αν και υπάρχουν κάποιες αποκλίσεις που αφορούν την οπτικοποίηση της σπηλαίωσης. Συγκεντρωτικά, τα αριθμητικά αποτελέσματα του επιλυτή MaPFlow είναι πολλά υποσχόμενα για την έρευνα γύρω από την ανάλυση και την πρόβλεψη του φαινομένου της σπηλαίωσης.

Acknowledgements

First of all, I would like to sincerely thank my supervisor, Professor George Papadakis for our flawless cooperation over these past 9 months, which truly sparked my passion for scientific research. His guidance was always present and facilitated the realization of this thesis.

I also would like to especially thank PhD candidate Dimitris Ntouras for the invaluable assistance during this whole process, as well as the countless insights into the fascinating field of CFD.

I owe thanks to Vasilis Efstathiadis for our insightful discussions regarding the modeling of marine propellers, which was a common theme for both of our research works.

Special thanks also go to Helena for always believing in me. Without her support, I would not have been able to make this effort that generated such a fulfilling outcome.

Last but certainly not least, I want to wholeheartedly thank my family for all the emotional, ethical and material support I have received from them during all these years.

Contents

List of Figures

List of Tables

1 Introduction

1.1 Cavitation

1.1.1 General Description of the Phenomenon

Cavitation is defined as the vaporization of a liquid when its local static pressure decreases below its evaporation pressure. The evaporation pressure, which is also known as saturation or vaporization pressure, is a physical identity of the liquid and depends solely on the temperature of the fluid. Cavitation should not be confused with boiling, although they have the common result of liquid evaporation. In the case of cavitation, this saturation occurs due to low pressure, while boiling is caused due to significant temperature increase, as it is graphically illustrated in Figure 1.1.

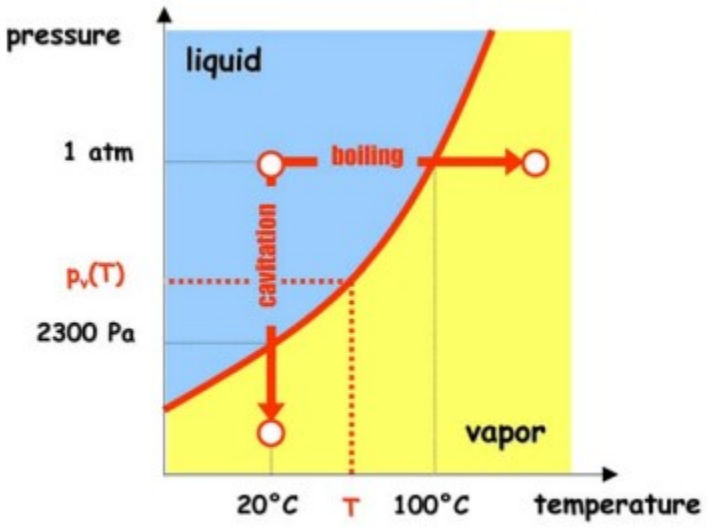

Figure 1.1: Water Phase Diagram

The cavitation phenomenon occurs in areas of the flow with high velocity, since this would lead to pressure decrease according to the Bernoulli theorem. The ambient temperature remains constant and in marine applications, like the ones investigated in the present work, it equals the temperature of the seawater. A slight temperature drop takes place at the

interface of the liquid and vapor phases, which can however be deemed as negligible for fluids like water where the density ratio between liquid and vapor is very high. Thus, the cavitation phenomenon in marine environments can be considered isothermal [1].

Another important concept is the cavity, which is the region or pocket of the produced vapor in a cavitating flow. Its size can range from a few bubbles to covering the whole extent of the geometry and it can be either steady and stationary over the surface or unsteady and experience separation from the surface and downstream transport.

A way to categorize cavitating flows is through the non-dimensional cavitation number σ, which is presented in Equation 1.1 in its general definition [2]. It has various more specific formulations according to the application it is employed for.

$$\sigma = \frac{\text{static pressure}}{\text{dynamic pressure}} \tag{1.1}$$

In the case of hydrofoils, the free stream-based cavitation number is used as it is described in Equation 1.2. In this equation, p_∞ and U_∞ are the freestream pressure and velocity respectively, p_{vap} is the evaporation pressure and ρ_l is the density of the liquid.

$$\sigma = \frac{p_\infty - p_{vap}}{\frac{1}{2}\rho_l U_\infty^2} \tag{1.2}$$

In the case of cavitation around marine propellers, where the rotational velocity is the significant component of the propeller motion, the rotational speed-based cavitation number is used. Its description is given in Equation 1.3, where n and D refer to the rotational speed and the diameter of the propeller respectively.

$$\sigma = \frac{p_\infty - p_{vap}}{\frac{1}{2}\rho_l (nD)^2} \tag{1.3}$$

For high values of the cavitation number, the static pressure overwhelms the dynamic pressure and thus cavitation does not occur as intensely. On the other hand, lower values of σ cause more intense cavitation phenomena.

1.1.2 Types of cavitation

In this section the five main categories of observable cavitation patterns are briefly described.

Bubble Cavitation

This type of cavitation occurs when the hydrofoil is placed at an angle of attack close to the ideal one. It includes the formation of bubbles that are separated from the surface, their downstream transportation and their final collapse at higher pressure regions. Regarding marine propellers, bubble cavitation is observed at the region of maximum thickness of the blade, since this is where the pressure is at its minimum [3].

Sheet Cavitation

Sheet cavitation is observed at an angle of attack different to the ideal. As a result, the lowest pressure is located at the leading edge of the suction side of the geometry. The cavity stays attached to the surface and the interface is clearly distinguishable.

Vortex Cavitation

Vortex cavitation is defined as the cavitation formation inside the vortices' cores. It occurs when the minimum pressure inside the vortices is lower than the evaporation pressure. Then, cavitation starts and is transported downstream within the vortex. Vortex cavitation around marine propellers can be further classified into three categories based on the region of the inception, namely tip vortex cavitation, hub vortex cavitation and propeller hull vortex cavitation.

Cloud Cavitation

In this case, the cavitating flow includes a collection of small bubbles that have been detached from sheet or bubble cavitation. For a marine propeller, this shedding phenomenon can take place during one propeller rotation while moving from regions of stronger to regions of weaker wake.

Supercavitation

Supercavitation refers to a cavitating flow with a cavity large enough to cover the whole or most of the geometry. Under supercavitating conditions, the skin friction of the object is lower, since the overlapping vapor sheet has lower viscosity than water and, thus, drag reduction occurs.

Figure 1.2 illustrates the various cavitation types that can be observed around a hydrofoil, reproduced from Franc [4]. In Figure 1.3, the same graphical presentation of the types and the possible regions of cavitation inception around marine propellers is presented, as it is illustrated by Politis [3].

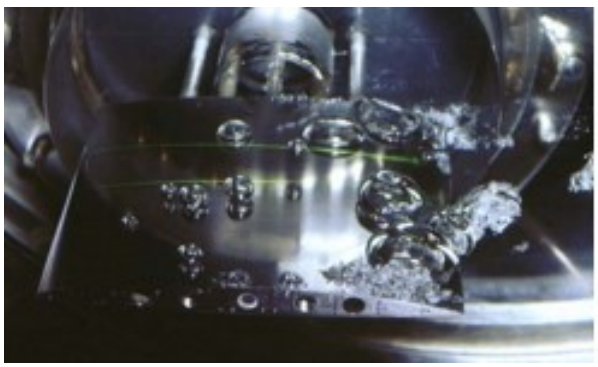

(a) Bubble cavitation

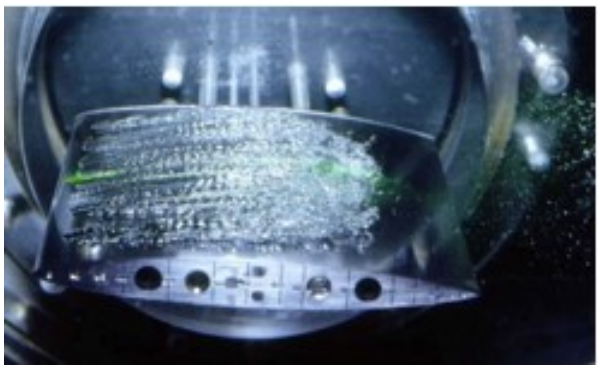

(b) Sheet cavitation

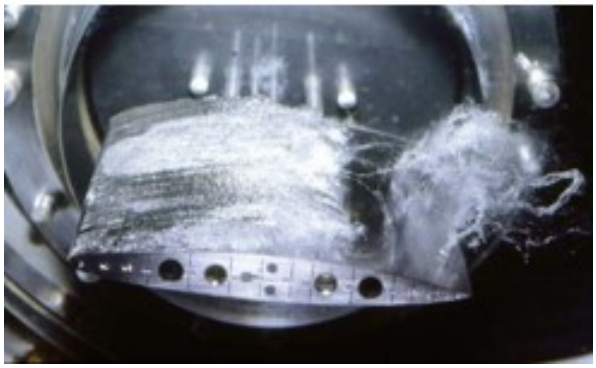

(c) Cloud cavitation

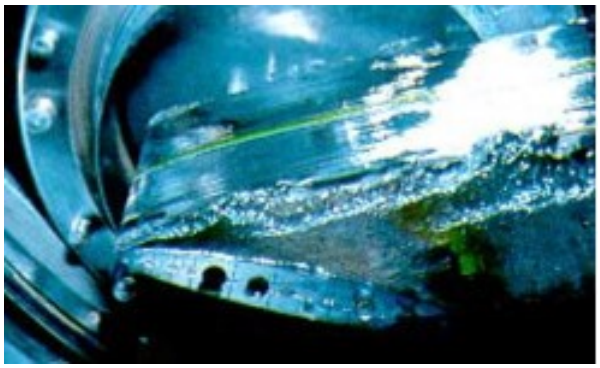

(d) Supercavitation

Figure 1.2: Types of cavitation around hydrofoils, reproduced from Franc [4]

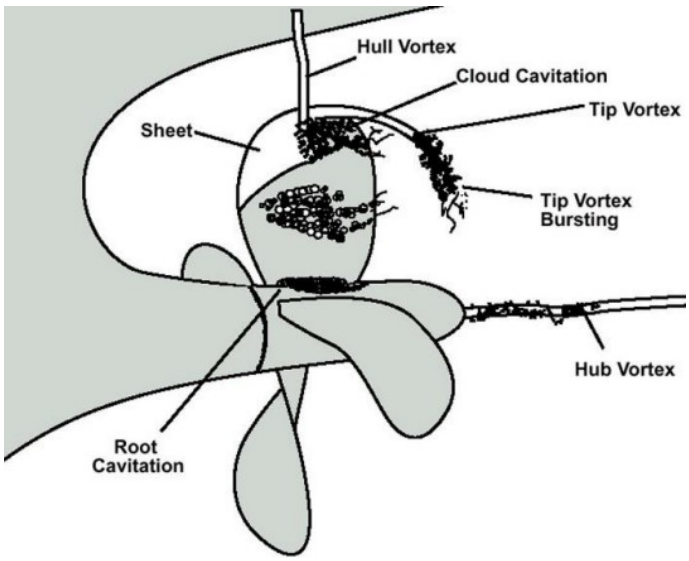

Figure 1.3: Propeller Cavitation Types, reproduced from Politis [3]

1.1.3 Effective Parameters

While the fluid pressure is the flow characteristic that determines the occurrence of cavitation, there are also other parameters that affect both the existence and the intensity of the phenomenon. A crucial parameter in determining the cavitating behavior is the amount of nuclei in the flow. Nuclei can be defined as dissolved or non-condensable gas bubbles within the liquid [5]. These particles act as weakness points inside the liquid and the breakdown of the liquid phase initiates from these points. Water with a lower nuclei content is a more homogeneous liquid and can thus withstand higher tension due to negative pressure than liquid with a high nuclei content.

Another significant aspect in the cavitation inception is the boundary layer. In full-scale propellers and hydrofoils the boundary layers are fully turbulent, which causes more intense cavitation. On the other hand, in the model scale geometries the boundary layer can be laminar in considerable parts of the leading edge region. This difference introduces uncertainty to the numerical modeling and can account for some possible computational discrepancies in the leading edge regions in comparison to the experiments. One way to overcome this issue in the experiments is to apply roughness to the leading edge region and thus trip the boundary layer into turbulence.

1.1.4 Cavitation Effects

In marine applications, and most notably in the case of propellers, cavitation causes a series of side effects, the most important of which are going to be briefly described in the current section. These include erosion, noise radiation, vibration and thrust breakdown.

Cavitation is by its nature a particularly violent phenomenon as far as both the generation and the destruction of the cavitation bubbles are concerned. This violent destruction of the vapor volumes when they enter higher pressure regions releases strong pressure pulses that strike the solid objects. This erosion is more common in the cases of cloud and bubble cavitation. The shock wave created by the destruction of the bubbles also cause radiation of noise over a wide range of frequencies that can be very harmful for humans. The cavitation type most susceptible to lead to noise radiation is the propeller hull vortex cavitation. When larger amounts of vapor are involved, like in the case of sheet cavitation, the destruction of the bubbles can cause significant pressure variations in the fluid, which in turn lead to vibrations of the cavitating structure [6].

Another especially important consequence of cavitation on marine propellers is the thrust breakdown it causes. At high cavitation numbers, not only does the cavitation phenomenon not reduce the propeller thrust, but it can also cause a small thrust increase. However, in different flow conditions, the pressure side of the blade can get increasingly covered with vapor. This causes a practical deactivation of the suction side of the blade, since there is no pressure difference to produce thrust. Due to this, the flow gets detached from the blade and thrust breakdown takes place [7].

1.1.5 Cavitation Experimental Testing

As it has been discussed, cavitation is a particularly dangerous phenomenon which has to be taken into account when designing propellers and hydrofoils. The traditional way to gather information and predict cavitating behavior has been the conduction of experiments around model scale geometries in a cavitation tunnel. The cavitation tunnel pumps water around a loop and past the investigated object. The pressure and velocity of the closed system are regulated and the goal is to set sea-like conditions. The documented results involve, among others, the propeller thrust and torque and detailed description of the pressure field

on the geometry. A typical sketch of a cavitation tunnel is presented in Figure 1.4 [8]. More information regarding experimental cavitation testing can be found in [9].

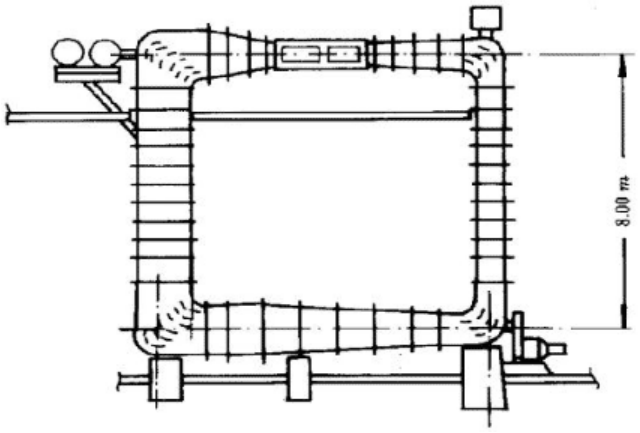

Figure 1.4: Cavitation Tunnel of HSVA [8]

The experiments conducted in cavitation tunnels usually concern model scale objects which leads to the need for scaling of the results to extrapolate them to full scale geometries. Apart from that, as it was mentioned above, cavitation is a phenomenon dependent on a variety of parameters. The task to ensure flow similarity between model and full scale objects through the satisfaction of all the parameters (viscosity, surface tension, nuclei content, velocity, density etc.) is impossible [2]. In order to overcome these difficulties attached to the experiments and to be able to predict the cavitation inception without the costly experiments, researchers in recent years have turned to Computational Fluid Dynamics.

1.2 CFD methods for cavitating flow

The cavitation phenomenon includes a variety of complex physical processes, such as, among others, phase change, turbulence, multiphase interface and variable fluid properties [10]. Thus, it is a very complex task to develop a generalized model able to be equally applicable for different problems. Several models employing different assumptions and simplifications have been proposed and applied to various situations depending on the nature of the flow and the cavitation type modeled, as well as the available computational resources.

In the present section, the main CFD methods for the simulation of cavitating flow are presented. Based on the Euler or Navier - Stokes equations these methods can be divided in two main categories: the interface tracking methods and the interface capturing methods depending on the modeling of the liquid - vapor interface.

1.2.1 Interface - Tracking Methods

In the interface-tracking methods, only the liquid phase has its physical properties resolved, while the interface between liquid and vapor is considered as a boundary condition for the equations of the liquid phase. The pressure is set equal to the saturation pressure along this interface. This methodology has been deemed as suitable only for simple cases, where the cavity has the form of a stable, fully defined gas volume, like for example in the case of stable two-dimensional sheet cavitation [11].

1.2.2 Interface - Capturing Methods

On the other hand, the interface-capturing approach, also known as continuum modeling, describes the flow as a mixture of liquid and vapor, in which the density continuously varies between the density of the individual phases. Hence, the interface between the two does not need to be tracked, as it is already modeled within the interpenetration of the two phases. These methods can be further classified in two categories based on the way the phase interaction is modeled: the inhomogeneous models and the homogeneous models.

Inhomogeneous model

In the inhomogeneous or full two-fluid model, both phases are modeled separately and a different set of equations is solved for each of the two. The exchange of mass, momentum and energy is approached explicitly through transfer terms, resulting in accurate modeling of mass and thermal exchange as well as surface tension at the interface. However, the exchange rates and the viscous friction have to be given to initialize the method and these values are very difficult to obtain. Furthermore, the most important reason that this approach has not been widely used in scientific research is the computational expense, as the required equations are double compared to the homogeneous model.

Homogeneous model

In the homogeneous or single fluid model, the liquid and vapor phase have common properties, like pressure, velocity and temperature at all points of the flow. Thus, a single set of the conservation laws is used for the modeling of the two phases. The density field can be obtained through various approaches, with some of the most notable ones being the following: state equation, barotropic equation and transport equation model.

In the state equation approach, the pressure, temperature and density are combined through the thermodynamic state law. However, as isothermal flow can be assumed for cavitation prediction, many researchers have instead used a barotropic equation to relate density with pressure. This approach has been used mainly due to the simplicity of its implementation, but the parallel prediction of pressure and density results in failure to capture fundamental fluid physics, such as vorticity production.

The transport equation models (TEM) use an additional transport equation to calculate the mixture density and the mass transfer between the two phases is modeled with source terms. In the most contemporary expressions of this approach, the mass or volume transfer rate of either liquid or vapor is modeled and the aforementioned transport equation is coupled with the conservation equations of the flow field to close the equations system. Various authors have accounted for different models, the most notable of which are further analyzed in the present section.

The Kunz cavitation model [12], which is similar to the one used by Merkle et al. [13], is centered around a pressure-based method, in which the evaporation and condensation terms dictate the mass transfer rates between the two phases. These mass transfer rates heavily depend on empirical factors, which have to be tuned according to the needs of the flow and geometry in hand. The source terms of this modeling approach have proved to offer flexibility regarding cavitation simulation, thus making this category of models the most widely used and the one with most variations. Efforts have also been made to remove the dependency on the empirical factors, as Senocak and Shyy [14] proposed a model to explicitly calculate the mass transfer coefficients from the interfacial velocity terms. However, the authors conclude that the approach needs further research to be considered an accurate cavitation prediction model.

Another approach was the derivation of the source terms from the Rayleigh-Plesset equation. Sauer and Schnerr [15] proposed a model based on the dynamics of a single bubble. Although the model is free of empirical factors, numerical uncertainty still exists and tuning needs to be applied for the values of the model constants, such as bubble radius and number. Aiming at an improved modeling of the phase change for models derived from the Rayleigh-Plesset equation , Zwart [16] implemented empirical factors, while Singhal [17] also introduced the effect of surface tension along with the empirical coefficients.

The main reason that the transport equation models have become the most widely used way to simulate cavitation is the convective character of the governing equations. They allow proper modeling of the bubble detachment and drift, as well as of the cavity closure. Moreover, unlike the aforementioned barotropic models, the density and pressure gradients are not parallel and the model can thus take into account vorticity production, a vital element of cavitating flow. However, it has to be noted that this approach also has a flaw deriving from the source terms. The parameters of each model have to be properly set, otherwise the accuracy of the numerical predictions will be significantly affected.

1.3 Objectives of the present research

The main objectives of this thesis can be summarized in the following:

- Development of a computational method to simulate cavitating flow and implementation of the method in the Eulerian solver MaPFlow.
- Calibration of the model coefficients around two-dimensional hydrofoils and validation with experimental results.
- Assessment of the capability of the model to predict the mechanism of unsteady cavitation around a three-dimensional hydrofoil.
- Evaluation of the model's prediction regarding cavitation around a model-scale marine propeller.

1.4 Thesis Outline

The thesis is divided in 7 chapters. In Chapter 1, an overview of the cavitation phenomenon is given along with the techniques used nowadays for the numerical cavitation modeling. In Chapter 2, the Eulerian in-house solver MaPFlow is presented and the problem is stated through its governing equations. Chapter 3 includes the cavitation modeling technique used in the present work along with the way it is implemented in the solver. Chapter 4 is centered around the calibration of the algorithm and the simulation of cavitation around two-dimensional hydrofoils. In Chapter 5, unsteady cavitation is introduced and simulated around a three-dimensional twisted hydrofoil. Chapter 6 focuses on the assessment of the capability of the implemented algorithm to predict cavitation around marine propellers. Finally, in Chapter 7, concluding remarks regarding the thesis are drawn and further research paths are recommended.

2 MaPFlow Solver

For the purpose of the present research, the solver MaPFlow [18] was used to carry out the numerical simulations. MaPFlow is an Eulerian multiphase solver developed by the Laboratory of Ship and Marine Hydrodynamics of the NTUA. It uses the Finite Volume method to solve the unsteady Reynolds-Averaged Navier Stokes (RANS) equations on unstructured grids. In the present study, the interface capturing method has been used for the two-phase modeling. The Transport Equation Model (TEM) is employed to simulate cavitation and both phases are assumed to be isothermal. The effect of gravity is deemed as negligible and is not taken into consideration.

2.1 Governing Flow Equations

2.1.1 Mass and Momentum Conservation

The Navier-Stokes equations are provided by applying the fundamental laws of mechanics to a fluid medium. Assuming an incompressible fluid, the conservation of mass and momentum can be expressed in differential vector form as it is shown in Equations 2.1 and 2.2. These equations are also known as the Continuity equation and the Momentum equation respectively.

$$\nabla \vec{u} = 0 \tag{2.1}$$

$$\frac{\partial \vec{u}}{\partial t} + \vec{u}\nabla\vec{u} = -\frac{1}{\rho}\nabla p + \nabla\vec{\sigma} + \vec{F}_B \tag{2.2}$$

In equations 2.1 and 2.2, ρ denotes the fluid density, $\vec{u}$ the velocity vector, p the pressure, $\vec{F}_B$ the source terms and body forces and $\vec{\sigma}$ the stress tensor.

2.1.2 The Volume-of-Fluid (VOF) Method

The flows under consideration in the present study are unsteady two-phase flows of two interpenetrating fluids. Thus, the interface between the two phases has to be accounted for. There have been various ways used to model the physique of this zone into the RANS equations. In the present work, the VOF method [19] is adopted in order to reduce the problem to a single fluid computation. Hence, the procedure requires the solution of only one set of equations, while the interface between the two fluids is treated as a density discontinuity and as a local transition to different flow properties. The basic principle of this method is the use of an indicator function to describe the phase of the examined area, denoting it as either liquid or gas phase. This function is called the volume fraction and is defined in equation 2.3. It will also be referred to as liquid volume fraction.

$$\alpha_l = \frac{\rho_m - \rho_v}{\rho_l - \rho_v} \tag{2.3}$$

where index l refers to the liquid phase, index v to the vapor phase and index m to the fluid mixture.As it is made clear from the above equation, the volume fraction takes the value of 1 in pure water regions and of 0 in pure vapor regions. In the areas close to the cavitation bubble the value of α_l is between 0 and 1. The blending equations 2.4 and 2.5 describe the properties of the fluid mixture.

$$\rho_m = \alpha_l \rho_l + (1 - \alpha_l)\rho_v \tag{2.4}$$

$$\mu_m = \alpha_l \mu_l + (1 - \alpha_l)\mu_v \tag{2.5}$$

The limit zone of the cavitation bubble, i.e. the limits between the vapor and liquid phases, is treated as a material surface and as such, the substantial derivative of the liquid volume fraction equals 0.

$$\frac{D\alpha_l}{Dt} = 0 \rightarrow \frac{\partial \alpha_l}{\partial t} + \vec{u}\nabla\alpha_l = 0 \tag{2.6}$$

2.1.3 The Artificial Compressibility Method

The incompressibility assumption for the flow leads to an inherent problem of the RANS equations, which is the decoupling of the continuity and momentum equations. A way to link them to a fully coupled system shall be considered. There are several approaches in relevant literature that address this issue. The most common way used are methods known as pressure-correction methods, such as the SIMPLE [20] and PISO [21] algorithms. However, in this study the adopted strategy is the Artificial Compressibility Method, which was originally proposed by Chorin [22].

The basic principle of the artificial compressibility method is the assumption of an artificial relation between density and pressure during convergence. This relation corresponds to the definition of the speed of sound in a compressible flow, as it can be seen in equation 2.7.

$$\frac{\partial p}{\partial \rho} = c^2 \tag{2.7}$$

However, in the case of an incompressible fluid, this relation is defined as a pseudo-time (τ) derivative, corresponding to the numerical procedure until convergence. The sound speed c is substituted by a numerical parameter β that regulates the convergence procedure.

$$\left.\frac{\partial \rho}{\partial p}\right|_{\tau} = \frac{1}{\beta} \tag{2.8}$$

The artificial compressibility method augments the mass equation with a pseudo-time derivative of pressure in order to get by the decoupling of the mass and momentum equations. Using the chain rule, as it can be seen in equation 2.9, the density pseudo-time derivative can be expressed by using the artificial compressibility parameter (β) and the pseudo time pressure derivative.

$$\frac{\partial \rho}{\partial \tau} = \frac{\partial \rho}{\partial p}\frac{\partial p}{\partial \tau} = \frac{1}{\beta}\frac{\partial p}{\partial \tau} \tag{2.9}$$

By using 2.1 and 2.9 the augmented mass equation is formed:

$$\frac{1}{\beta}\frac{\partial p}{\partial \tau} + \rho \nabla \vec{u} = 0 \tag{2.10}$$

Once the numerical solution has converged in pseudo-time domain, the first term of equation 2.10 is equal to 0 and the initial form of the equation is satisfied in the physical time domain.

2.1.4 Derivation of Conservative Form

The equations of mass, momentum and liquid volume fraction are written in their conservative form as is presented below. Firstly, the mass equation with the fictitious time derivative term is described

$$\frac{\partial \rho}{\partial \tau} + \nabla(\rho \vec{u}) = 0 \tag{2.11}$$

By eliminating the density time derivative and the density gradient and introducing equation 2.9, the following form is obtained:

$$\frac{1}{\beta}\frac{\partial p}{\partial \tau} + \rho \nabla \vec{u} = 0 \tag{2.12}$$

The same procedure is applied to the conservative momentum equation provides

$$\frac{\partial \rho \vec{u}}{\partial t} + \frac{\partial \rho \vec{u}}{\partial \tau} + \nabla(\rho \vec{u} \cdot \vec{u}) = -\nabla p + \nabla \sigma + \vec{F}_B \tag{2.13}$$

The temporal term of equation 2.12 can be expanded as follows:

$$\frac{\partial \rho \vec{u}}{\partial t} = \rho \frac{\partial \vec{u}}{\partial t} + \vec{u}\frac{\partial \rho}{\partial t} = \rho \frac{\partial \vec{u}}{\partial t} + \vec{u}\frac{\partial}{\partial t}(\alpha_l \Delta\rho + \rho_v) = \rho \frac{\partial \vec{u}}{\partial t} + \vec{u}\Delta\rho \frac{\partial \alpha_l}{\partial t} \tag{2.14}$$

where $\Delta\rho$ denotes the difference in density of the two fluids.

The pseudo-time term can be expanded the same way like Equation 2.14:

$$\frac{\partial \rho \vec{u}}{\partial \tau} = \rho \frac{\partial \vec{u}}{\partial \tau} + \vec{u} \Delta \rho \frac{\partial \alpha_l}{\partial \tau} \tag{2.15}$$

Finally, the transport equation for the liquid volume fraction under the same scope will be:

$$\frac{\partial \alpha_l}{\partial t} + \frac{\partial \alpha_l}{\partial \tau} + \frac{\alpha_l}{\rho_m \beta} \frac{\partial p}{\partial \tau} + \nabla(\vec{u} \alpha_l) = 0 \tag{2.16}$$

Equations 2.12, 2.13 and 2.16 constitute a fully coupled system of non-linear equations, able to describe unsteady two-phase flows.

By considering a reference volume Ω and integrating all the field quantities over it, the equation system can be written in the following matrix form:

$$\Gamma \int_\Omega \frac{\partial \vec{Q}}{\partial \tau} d\Omega + \Gamma_e \int_\Omega \frac{\partial \vec{Q}}{\partial t} d\Omega + \oint_{\partial \Omega} (\vec{F_c} - \vec{F_v}) dS = \int_\Omega \vec{S_q} d\Omega \tag{2.17}$$

where the matrix Γ is the Kunz preconditioner [12] used to deal with the problem becoming stiff when high density ratios appear in the system eigenvalues. Vectors $\vec{Q}$ and $\vec{U}$ are the vectors containing the primitive and conservative variables respectively, while $\vec{S_q}$ denotes the source term vector. It has to be noted that in the present study the effect of gravity is omitted and thus $\vec{S_q}$ contains the source terms related to the cavitation modeling discussed in the next chapter. It can be observed that at each physical timestep the unsteady system of equations is expressed for the conservative variables $\vec{U}$, while at each fictitious timestep, a pseudo-steady state problem is solved for the primitive variables $\vec{Q}$. The transformation from the conservative to the primitive form is achieved through the Jacobian matrix $\Gamma_e = \frac{\partial \vec{U}}{\partial \vec{Q}}$.

$$\vec{U} = \begin{bmatrix} 0 & \rho \vec{u} & \alpha_l \end{bmatrix}^T \qquad \vec{Q} = \begin{bmatrix} 0 & \rho \vec{u} & \alpha_l \end{bmatrix}^T \tag{2.18}$$

$$\Gamma = \begin{bmatrix} \frac{1}{\beta\rho_m} & 0 & 0 \\ 0 & \rho_m I & \vec{u}\Delta\rho \\ \frac{\alpha_l}{\beta\rho_m} & 0 & 1 \end{bmatrix} \qquad \Gamma_e = \begin{bmatrix} 0 & 0 & 0 \\ 0 & \rho_m I & \vec{u}\Delta\rho \\ 0 & 0 & 1 \end{bmatrix} \tag{2.19}$$

Also, the inviscid and viscous fluxes $\vec{F_c}$ and $\vec{F_v}$ are described as:

$$\vec{F_c} = \begin{bmatrix} V_n \\ \rho_m u\Delta V + pn_x \\ \rho_m v\Delta V + pn_y \\ \rho_m w\Delta V + pn_z \\ \alpha_l V_n \end{bmatrix} \qquad \vec{F_v} = \begin{bmatrix} 0 \\ \tau_{xx}n_x + \tau_{xy}n_y + \tau_{xz}n_z \\ \tau_{yx}n_x + \tau_{yy}n_y + \tau_{yz}n_z \\ \tau_{zx}n_x + \tau_{zy}n_y + \tau_{zz}n_z \\ 0 \end{bmatrix} \tag{2.20}$$

where $V_n = \vec{u} \cdot \vec{n}$, $V_g = \vec{u}_{vol} \cdot \vec{n}$ and $\Delta V = V_n - V_g$. The velocity $\vec{u}_{vol}$ corresponds to the movement of the control volume and $\vec{u}_n$ denotes the velocity normal to the control volume.

According to the Boussinesq' hypothesis, the viscous stresses τ_{ij} are described by the following equation:

$$\tau_{ij} = (\mu_m + \mu_t)(\frac{\partial u_i}{\partial x_j} + \frac{\partial u_j}{\partial x_i}) - \frac{2}{3}\rho\delta_{ij}k \tag{2.21}$$

where μ_t is the turbulent dynamic viscosity, k is the turbulent kinetic energy and δ_{ij} is the Kronecker delta.

2.1.5 Rotating Frame of Reference

In cases where the object is rotating, like the case of a marine propeller that is examined later in the present study, the transformation of the Navier-Stokes equations into a rotating frame of reference is deemed convenient [23]. MaPFlow uses the absolute velocity formulation, as it has been shown to produce better results regarding the evaluation of fluxes using the finite volume method.

The absolute velocity of a point rotating with a steady rotational velocity ω around a steady axis can be expressed as seen in equation 2.22, where $\vec{u_r}$ is the relative velocity. The effects due to the Coriolis force and due to the centrifugal force also have to be taken into consideration.

$$\vec{u}_a = \vec{u}_r + \vec{\omega} \times \vec{r} \tag{2.22}$$

To integrate the rotating frame approach into the RANS equations, the absolute velocity as expressed in equation 2.22 has to simply substitute the relative velocity in equations 2.12, 2.13 and 2.16.

$$\frac{1}{\beta}\frac{\partial p}{\partial \tau} + \rho \nabla \vec{u} = 0 \tag{2.23}$$

$$\frac{\partial \rho \vec{u}}{\partial t} + \frac{\partial \rho \vec{u}}{\partial \tau} + \nabla[\rho \vec{u}(\vec{u} - \vec{\omega} \times \vec{r}) + p\vec{I} - \vec{\tau}] = -\rho(\vec{\omega} \times \vec{u}) \tag{2.24}$$

$$\frac{\partial \alpha_l}{\partial t} + \frac{\partial \alpha_l}{\partial \tau} + \frac{\alpha_l}{\rho_m \beta}\frac{\partial p}{\partial \tau} + \nabla[(\vec{u} - \vec{\omega} \times \vec{r})\alpha_l] = 0 \tag{2.25}$$

2.2 Spatial Discretization

2.2.1 The Finite Volume Method

The Finite Volume Method is utilized for the spatial discretization of the equation system in MaPFlow. The mesh is divided into arbitrary cells with volume Ω_i, while the center of their volume coincides with the cell center. The field quantities are stored at the cell centers. For a given control volume Ω_i the primitive variables will be integrated to

$$\vec{\overline{Q}} = \frac{1}{\Omega_i}\int_{\Omega_i} \vec{Q}(\vec{x}, t) d\Omega \tag{2.26}$$

Using the Finite Volume Method on Equation 2.17 provides

$$\Gamma_e \frac{\partial \vec{\overline{Q}} \Omega}{\partial t} + \Gamma \frac{\partial \vec{\overline{Q}} \Omega}{\partial \tau} = -\oint_{\partial \Omega_i(t)} (\vec{F}_c - \vec{F}_v) dS + \int_{\Omega_i(t)} \vec{S}_q d\Omega \tag{2.27}$$

By gathering the right hand side of the equation in a spatial residual $\vec{R}_\Omega$, equation 2.27 is written

$$\Gamma_e \frac{\partial \vec{\overline{Q}}\Omega}{\partial t} + \Gamma \frac{\partial \vec{\overline{Q}}\Omega}{\partial \tau} = -\vec{R}_\Omega \tag{2.28}$$

,where

$$\vec{R_\Omega} = \oint_{\partial\Omega_i(t)} (\vec{F_c} - \vec{F_v}) dS - \int_{\Omega_i(t)} \vec{S_q} d\Omega \tag{2.29}$$

The surface integral of the residual $\vec{R}_\Omega$ is approximated to be constant across different edges of each cell. Hence, it can be calculated as a sum of the fluxes evaluated at the midpoint of each face. Moreover, the volume integral of the source term does not vary throughout each elemental volume, according to an employed approximation. Thus, the residual can be described in the following equation if Nf is the total number of faces of the corresponding control volume Ω_i

$$\vec{R}_\Omega = \sum_{j}^{N_f} (\vec{F_c} - \vec{F_v})_j dS_i - \vec{S_q}\Omega_i \tag{2.30}$$

For purposes of simplification, in the next sections the averaging operator $\overline{Q}$ will be omitted.

2.2.2 Variable Reconstruction

MaPFlow, as already mentioned previously, is a code operating with the variable values in the centers of the cells, i.e. all the calculations are done in the element centers. However, in order to calculate the right-hand side residual of equation 2.17, the information needs to be transported to the cell faces, as it is made clear in equation 2.30. Variable reconstruction is the process of transferring the value of these variables at the cell centers to the respective cell edges via extrapolation. This process can be fulfilled by various suitable schemes.

A schematic representation of the variable reconstruction process is presented in Figure 2.1. Two adjacent cells i and j with control volumes Ω_i and Ω_j and connecting through face f are considered. $\vec{\phi}_L$ denotes the extrapolated value of vector $\vec{\phi}_i$ on the left side of f and $\vec{\phi}_R$ the extrapolation of $\vec{\phi}_j$ on the right side of f.

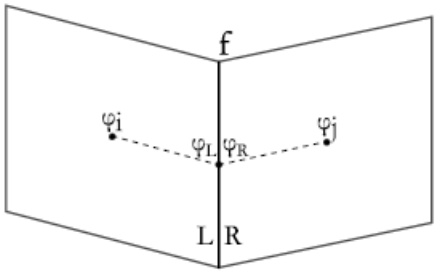

Figure 2.1: Reconstruction of Variables on face f

For each variable a reconstruction scheme has to be chosen to account for its variations throughout the domain.

Velocity Field Reconstruction

To approximate the velocity field, the Piecewise Linear Reconstruction (PLR) scheme is implemented, as the velocity field is continuous everywhere in the mesh. Hence, the PLR scheme is applied without the use of limiters [24].

According to the PLR scheme, the flow variables are linearly distributed over the control volume

$$\begin{aligned} \vec{u}_L &= \vec{u}_i + \nabla(\vec{u}_i \cdot \vec{r}_i) \\ \vec{u}_R &= \vec{u}_j + \nabla(\vec{u}_j \cdot \vec{r}_j) \end{aligned} \tag{2.31}$$

Pressure Field Reconstruction

As it has been mentioned, in the present study the effect of gravity is omitted. Thus, both the pressure field and the pressure gradient demonstrate continuous behavior and ,as a result, the Piecewise Linear Reconstruction scheme can be employed. The pressure is reconstructed according to the following relation.

$$\begin{aligned} p_L &= p_i + \nabla(p_i \cdot \vec{r}_i) \\ p_R &= p_j + \nabla(p_j \cdot \vec{r}_j) \end{aligned} \tag{2.32}$$

Volume Fraction Field Reconstruction

Under a similar scope, the treatment of the inherently discontinuous volume fraction field (α_l) should also be examined. A suitable reconstruction scheme is applied in order to preserve the associated interface sharpness and hinder excessive smearing due to numerical diffusion. Numerous higher order reconstruction schemes have been introduced that limit numerical diffusion. Most of them are based on Leonard's Normalized Variable Diagram [25]. Even though these schemes offer higher accuracy, it was determined that for the present study a simple first order upwind reconstruction scheme offers sufficient accuracy and low numerical diffusion. Thus, the upwind scheme was used for the reconstruction of α_l in the entirety of the computational domain, including the area of the interface between the two fluids.

The first order upwind scheme used for the reconstruction of the volume fraction (α_l) is expressed as follows

$$\begin{aligned} \alpha_L &= \alpha_i \\ \alpha_R &= \alpha_j \end{aligned} \tag{2.33}$$

2.2.3 Convective Fluxes

As it was analyzed, two different values $\vec{Q}_R$ and $\vec{Q}_L$ are extrapolated on the same edge after the variable reconstruction on the cell faces. Thus, a discontinuity is created and has to be accounted for. This discontinuity along with the fact that the system of equation is hyperbolic in pseudo-time, constitute a Riemann problem, which is solved by using the approximate Riemann solver of Roe [26]. Moreover, to overcome the density dependency of the inviscid Jacobian eigenvalues the preconditioning matrix Γ has been used. The preconditioned Jacobian matrix that transforms the conservative variables to primitive is described by equation 2.34 and its analytical form is given in equation 2.35.

$$A_c = \frac{\partial \vec{F_c}}{\partial Q} = \Gamma\Gamma^{-}1A_c = \Gamma\tilde{A}_c \tag{2.34}$$

$$\tilde{A}_c = \begin{bmatrix} 0 & n_x & n_y & n_z & 0 \\ n_x & \rho_m(n_x u + \Delta V) & \rho_m n_y u & \rho_m n_z u & u\Delta V \Delta\rho \\ n_y & \rho_m n_x v & \rho_m(n_y v + \Delta V) & \rho_m n_z v & v\Delta V \Delta\rho \\ n_z & \rho_m n_x w & \rho_m n_y w & \rho_m(n_z w + \Delta V) & w\Delta V \Delta\rho \\ 0 & \alpha_l n_x & \alpha_l n_y & \alpha_l n_z & \Delta V \end{bmatrix} \tag{2.35}$$

Using the aforementioned Riemann solver, the convective fluxes at a face f are

$$\vec{F}_{c,f} = \frac{1}{2}(\vec{F}_c(\vec{Q}_R) + \vec{F}_c(\vec{Q}_L)) - \frac{1}{2}\overline{\Gamma|\tilde{A}_c|}_f(\vec{Q}_R - \vec{Q}_L) \tag{2.36}$$

where $|\tilde{A}_c|$ is the Roe averaged preconditioned Jacobian matrix given as

$$|\tilde{A}_c|_f = \tilde{R}^{-1}|\tilde{\Lambda}|\tilde{R} \tag{2.37}$$

$\tilde{R}$ and $\tilde{R}^-1$ are the right and left eigenvectors respectively , while $\tilde{\Lambda}$ are the eigenvalues of $|\tilde{A}_c|$. To compute the inviscid Jacobian of equation 2.37 the Roe averaged quantities on face f are denoted as

$$\overline{\vec{u}} = \frac{\sqrt{\rho_R}\vec{u}_R + \sqrt{\rho_L}\vec{u}_L}{\sqrt{\sqrt{\rho_R} + \sqrt{\rho_L}}}, \qquad \overline{\rho} = \sqrt{\rho_R \rho_L} \tag{2.38}$$

The eigenvalues of $|\tilde{A}_c|$ are described in the following equation.

$$\begin{aligned} \lambda_{1,2,5} &= V_n - V_g \\ \lambda_3 &= V_n - c - \frac{V_g}{2} \\ \lambda_4 &= V_n + c - \frac{V_g}{2} \end{aligned} \tag{2.39}$$

In the above equation c is the artificial sound speed that appears in equation 2.7 and is expressed as follows

$$c = \sqrt{\beta + (V_n - \frac{V_g}{2})^2} \tag{2.40}$$

The right and left eigenvectors of the Jacobian 2.34 are described in equations 2.41 and 2.42 respectively

$$\tilde{R} = \begin{bmatrix} 0 & 0 & -\rho_m c_m & -\rho_m c_p & 0 \\ x_1 & x_2 & n_x + \frac{u\lambda_3}{\beta} & n_x + \frac{u\lambda_4}{\beta} & 0 \\ y_1 & y_2 & n_y + \frac{v\lambda_3}{\beta} & n_y + \frac{v\lambda_4}{\beta} & 0 \\ z_1 & z_2 & n_z + \frac{w\lambda_3}{\beta} & n_z + \frac{w\lambda_4}{\beta} & 0 \\ 0 & 0 & 0 & 0 & 1 \end{bmatrix} \tag{2.41}$$

$$\tilde{R}^{-1} = \begin{bmatrix} \frac{1}{\rho_m c_g}[n_x(wy_2 - vz_2) & \frac{1}{c_g}[\beta(n_z y_2 - n_y z_2) & \frac{1}{c_g}[\beta(n_x z_2 - n_z x_2) & \frac{1}{c_g}[\beta(n_y x_2 - n_x y_2) & 0 \\ +n_y(uz_2 - wx_2) + & +\Delta V(wy_2 - vz_2)] & +\Delta V(uz_2 - wx_2)] & +\Delta V(ux_2 - uy_2)] & \\ +n_z(vx_2 - uy_2)] & & & & \\ \frac{1}{\rho_m c_g}[n_x(vz_1 - wy_2) & \frac{1}{c_g}[\beta(n_y z_1 - n_x y_1) & \frac{1}{c_g}[\beta(n_z x_1 - n_x z_1) & \frac{1}{c_g}[\beta(n_z y_1 - n_y x_1) & 0 \\ +n_y(wx_1 - uz_1) & +\Delta V(wy_1 - vz_1)] & +\Delta V(wx_1 - uz_1)] & +\Delta V(ux_1 - uy_1)] & \\ +n_z(uy_1 - vx_1)] & & & & \\ -\frac{1}{\rho_m 2cc_g}(\beta + \lambda_4 V_n) & \frac{1}{2cc_g}(\beta c_p n_x) & \frac{1}{2cc_g}(\beta c_p n_y) & \frac{1}{2cc_g}(\beta c_p n_z) & 0 \\ \frac{1}{\rho_m 2cc_g}(\beta + \lambda_3 V_n) & \frac{1}{2cc_g}(\beta c_m n_x) & \frac{1}{2cc_g}(\beta c_m n_y) & \frac{1}{2cc_g}(\beta c_m n_z) & 0 \\ 0 & 0 & 0 & 0 & 1 \end{bmatrix} \tag{2.42}$$

where c_m, c_p and c_g are described in equation 2.43 and $\vec{x_1}$ and $\vec{x_2}$ are the unit vectors $\vec{x_1} = (x_1, y_1, z_1)$ and $\vec{x_2} = (x_2, y_2, z_2)$.

$$c_m = c - \frac{V_g}{2}, \qquad c_p = c + \frac{V_g}{2}, \qquad c_g = \beta + V_n \Delta V \tag{2.43}$$

2.2.4 Viscous Fluxes

To calculate the viscous fluxes on a face f between two elements i and j, a simple averaging procedure is followed

$$\vec{Q}_{ij} = \frac{1}{2}(\vec{Q}_i + \vec{Q}_j) \tag{2.44}$$

The gradients are computed through supplementing the Green-Gauss formula with an additional directional vector $\vec{t}_{ij}$.

$$\nabla\vec{Q}_{ij} = \overline{\nabla\vec{Q}_{ij}} + [\overline{\nabla\vec{Q}_{ij}} \cdot \vec{t}_{ij} - \frac{\partial\vec{Q}}{\partial l}_{ij}] \cdot \vec{t}_{ij} \tag{2.45}$$

where $\vec{t}_{ij}$ is the unit vector from the cell center i to the cell center j and l is the distance between them. $\overline{\nabla\vec{Q}_{ij}}$ is the mean gradient defined as follows

$$\overline{\nabla\vec{Q}_{ij}} = \frac{1}{2}(\nabla\vec{Q}_i + \nabla\vec{Q}_j) \tag{2.46}$$

2.3 Temporal Discretization

Regarding the discretization of the flow equations in time, the implicit formulation of the problem with $\vec{Q}^*$ being the vector of the flow variables is

$$\Gamma\frac{\partial(\vec{Q}^*\Omega_i)}{\partial\tau} + \vec{R}^* = 0 \tag{2.47}$$

where $\vec{R}^*$, which is described in the equation below, is the unsteady residual including the spatial residual of equation 2.28 and the unsteady term.

$$\vec{R}^* = \vec{R}_{\Omega_i}(\vec{Q}^*) + \Gamma_e\frac{\partial(\vec{Q}^*\Omega_i)}{\partial t} \tag{2.48}$$

Within the framework of the dual time-stepping technique, two indices n and k are introduced to describe the iterations in the physical and the fictitious time domains respectively. In particular, for every physical timestep a steady problem is solved in the pseudo-time domain, starting with k = 0. The flow variables vector is initialized based on the previous convergent solution $\vec{Q}_0^{*,n+1} = \vec{Q}_k^n$. During this process, $\vec{Q}^*$ does not satisfy the original equation. Once convergence is achieved, the term $\Gamma\frac{\partial(\vec{Q}^*\Omega_i)}{\partial\tau}$ is eliminated and the initial equations are recovered and the problem is solved in the physical time domain.

For the discretization of the unsteady term, a Backward Differentiation Formula (BDF) scheme [27] is applied, providing the following series of successive time levels

$$\frac{\partial(\vec{Q}^*\Omega_i)}{\partial t} = \frac{1}{\Delta t}[\phi_{n+1}(\Omega_i\vec{Q})^{n+1} + \phi_n(\Omega_i\vec{Q})^n + \phi_{n-1}(\Omega_i\vec{Q})^{n-1} + \phi_{n-2}(\Omega_i\vec{Q})^{n-2} + ...] \quad (2.49)$$

The discretization of the pseudo time derivative is achieved through a first-order backward difference scheme

$$\frac{\partial(\vec{Q}^*\Omega_i)}{\partial\tau} = \Omega_i^{n+1}\frac{\vec{Q}^{*,k+1} - \vec{Q}^{*,k}}{\Delta\tau} \quad (2.50)$$

For convergence purposes, the local time stepping technique is applied. The local fictitious timestep is described as

$$\Delta\tau = CFL\frac{D_i}{\hat{\Lambda}_{c,i}} \quad (2.51)$$

where $\hat{\Lambda}_{c,i}$ is the convective spectral radii described as

$$\hat{\Lambda}_{c,i} = \sum_{j=1}^{N_f}(|\vec{V}_n - \frac{V_g}{2}| + c)_{ij}\Delta S_{ij} \quad (2.52)$$

2.4 Turbulence Modeling

Turbulent flows have been modeled with various approaches depending on the application and the available computational resources. Direct Numerical Simulation (DNS), Large Eddy Simulation (LES) and Detached Eddy Simulation (DES) all present a high level of solution accuracy at the expense of significantly increased computational cost. Due to that, the aforementioned techniques are very limited in their usage. To satisfy the needs of simulating practical applications at a reasonable computational cost, MaPFlow uses the RANS method to model turbulence. The RANS models have been developed based on the Boussinesq hypothesis regarding the Reynolds Stress tensor. One or more transport equations are solved to determine the value of the turbulent kinetic viscosity and the turbulent kinetic energy field. In the present study, the $k-\omega$ SST Model has been used to capture the effect of turbulence on the flow.

The k-ω SST Model

The k-ω Shear Stress Transport model is a two equation eddy-viscosity model originally introduced by Menter [28]. This model incorporates the k-ω model near the domain's wall boundaries and the k-ϵ model in the free-stream region. Through this model blending, it is possible to combine the excellent behavior of the first one in the treatment of near wall areas and separation flows with the capability of the second one in handling inlet free-stream turbulence properties.

The advection-diffusion equations for the turbulent kinetic energy k and the specific dissipation rate ω are

$$\begin{aligned} \frac{\partial(\rho k)}{\partial t} + \nabla(\vec{u}\rho k = \nabla[(\mu + \sigma_k \mu_t)\nabla k] + \rho P_k - \beta^* \rho \omega k \\ \frac{\partial(\rho \omega)}{\partial t} + \nabla(\vec{u}\rho \omega = \nabla[(\mu + \sigma_\omega \mu_t)\nabla \omega] + \alpha \rho S^2 - \beta \rho \omega^2 + 2(1 - F_1)\frac{\rho \sigma_{\omega_2} \omega}{\nabla} k \cdot (\nabla \omega)^T \end{aligned} \tag{2.53}$$

where $P_k = min(\mu_t(\nabla \times \vec{u})(\nabla \times \vec{u})^T, 10\beta^* \rho k \omega)$ is the turbulent kinetic energy production term, μ_t is the turbulent dynamic (or eddy) viscosity and $S = \sqrt{2S_{ij}S_{ij}}$ is the mean strain rate. F_1 and F_2 are switching functions between the two aforementioned turbulence models. When $F_1 = 1$, the set of the $k-\omega$ equations is solved, while for $F_1 = 0$ the $k-e$ equations

are applied. These switching functions are defined in the following equations.

$$F_1 = \tanh\{\{min[max(\frac{\sqrt{k}}{\beta^*\omega y}, \frac{500v}{y^2\omega}), \frac{4\rho\sigma_{\omega_2}k}{CD_{k\omega}y^2}]\}^4\} \tag{2.54}$$

$$F_2 = \tanh\{[max(\frac{2\sqrt{k}}{\beta^*\omega y}, \frac{500v}{y^2\omega})]^2\} \tag{2.55}$$

$$CD_{k\omega} = max(2\frac{\rho\sigma_{\omega_2}}{\omega}\nabla k \cdot (\nabla\omega)^T, 10^{-10} \tag{2.56}$$

The model constants are : $\beta^* = 0.09, \alpha_1 = 5/9, \beta_1 = 0.075, \sigma_{k_1} = 0.85, \sigma_{\omega_1} = 0.5, \alpha_2 = 0.44, \beta_2 = 0.0828, \sigma_{k_2} = 1.0, \sigma_{\omega_2} = 0.856$. These parameters also subject to blending according to the following function.

$$\phi = F_1\phi_1 + (1 - F_1)\phi_2 \tag{2.57}$$

Finally, a limiter is also applied to regulate the dynamic viscosity.

$$\mu_t = \frac{\rho\alpha_1 k}{max(\alpha_1\omega, SF_2)} \tag{2.58}$$

3 Cavitation Modelling

From the available computational methods to simulate cavitation, the transport equation model is the most widely used one in the case of hydrofoils and marine propellers. Various works have focused on the comparison and assessment of the accuracy of the cavitation models listed in the introductory chapter. Regarding cavitation around hydrofoils, [29] and [30] both come to the conclusion that all models can reproduce two-dimensional sheet cavitation with similar accuracy, which is also the result in a similar research work centered around marine propellers [31].

From the findings of these studies, it has been concluded that all the available Transport Equation Models listed above can accurately predict cavitation in various marine environments, without significant differences to one another. In the present work, the Kunz cavitation model, as it is presented in the current chapter, has been employed to simulate cavitating flow.

3.1 Kunz Mass Transfer Model

Kunz [12] proposed a cavitation model, in which the mass transfer rates between the two phases are controlled through the source terms seen in Equations 3.1 and 3.2. The transformation from liquid to vapor m^- is proportional to the liquid volume fraction and to the amount by which the pressure is below the saturation pressure (Equation 3.1). The transformation of vapor to liquid m^+ is modeled through the use of a simplified form of the Ginzburg-Landau potential (Equation 3.2).

$$m^- = \frac{C_{dest}\rho_v\alpha_l MIN[0, p - p_{vap}]}{(\frac{1}{2}\rho_l U_\infty^2)t_\infty} \tag{3.1}$$

$$m^+ = \frac{C_{prod}\rho_v\alpha_l^2(1-\alpha_l)}{t_\infty} \tag{3.2}$$

The evaporation or destruction coefficient is denoted as C_{dest} and the condensation or production coefficient as C_{prod}. Both terms are non-dimensionalised with respect to the mean flow time scale t_∞, which is determined through the equation $t_\infty = \frac{L_{ref}}{U_\infty}$, where L_{ref} is the reference length and U_∞ is the free stream velocity. The evaporation term is also non-dimensionalised with respect to the freestream kinetic energy.

Regarding the condensation and evaporation coefficient, it is documented that they are empirical and their values have to be adjusted for every different examined flow and geometry individually. Their proper tuning plays a crucial role in the accuracy of the numerical results. This coefficient calibration procedure is a crucial part of the present study and will be further analyzed in the following chapter. The values proposed for these coefficients by Kunz in the original formulation of the model are $C_{dest} = 100$ and $C_{prod} = 100$.

It is also important to understand the physical importance of these empirical coefficients in the numerical modeling. It was observed that increasing the value of the evaporation coefficient C_{evap} leads to a longer cavity and the formed bubble is transported towards the downstream direction. Moreover, the negative pressure coefficient at the leading edge decreases [32]. As far as the condensation coefficient C_{cond} is concerned, the pressure coefficient gradient is higher with increased values of C_{cond}. As a result, the condensation at the end of the bubble is more abrupt with higher condensation coefficients. No significant effect of this coefficient on the cavity length has been found.

3.2 Numerical Implementation

Rewriting the conservative form of the mass (2.12), momentum (2.13) and volume fraction equations (2.16) to include the implementation of the mass transfer models source terms, the following equations are obtained.

$$\frac{1}{\beta}\frac{\partial p}{\partial \tau} + \rho \nabla \vec{u} = (m^+ + m^-)(\frac{1}{\rho_l} - \frac{1}{\rho_v}) \tag{3.3}$$

$$\frac{\partial \rho \vec{u}}{\partial t} + \frac{\partial \rho \vec{u}}{\partial \tau} + \nabla(\rho \vec{u} \cdot \vec{u}) = -\nabla p + \nabla \sigma + \vec{F_B} \tag{3.4}$$

$$\frac{\partial \alpha_l}{\partial t} + \frac{\partial \alpha_l}{\partial \tau} + \frac{\alpha_l}{\rho_m \beta}\frac{\partial p}{\partial \tau} + \nabla(\vec{u}\alpha_l) = (m^+ + m^-)\frac{1}{\rho_l} \tag{3.5}$$

It has to be noted that the source terms also appear in the mass conservation equation, as this equation is an expression of the conservation of the mixture volume.

Cavitating flow is characterized by phenomena of intense mass transfer between the two phases. These phenomena provide a major challenge for the numerical algorithms, as the high initial evaporation rate changes the local fluid properties by 3 orders of magnitude. This abrupt property change requires a numerical treatment that supplies stability to the algorithm, and thus a fully explicit treatment of the source terms is not a viable option. A purely implicit treatment would not be appropriate either, as, according to the linear stability theory, this treatment would be stable only as long as the eigenvalues of the source Jacobian are all negative, which is not the case in the present problem.

In order to overcome these numerical stability issues, Kunz [12] proposes to follow the strategy of Venkateswaran [33] for the numerical treatment of mass transfer source terms in reacting flow computations. The basic principle of this strategy is the identification of a source and a sink component among the mass transfer source terms. Then, the sink term is treated implicitly and the source term explicitly [34]. Going back to equation 2.17, the source term vector $\vec{S}_q$ is split to the vectors $\vec{S}_q^+$ and $\vec{S}_q^-$, which refer to the condensation and the evaporation mass transfer rates respectively. These source terms vectors are described in the following equation.

$$\begin{aligned} \vec{S}_q &= \vec{S}_q^+ + \vec{S}_q^- \\ \vec{S}_q^+ &= [m^+(\frac{1}{\rho_l} - \frac{1}{\rho_v}), 0, 0, 0, m^+\frac{1}{\rho_l}]^T \\ \vec{S}_q^- &= [m^-(\frac{1}{\rho_l} - \frac{1}{\rho_v}), 0, 0, 0, m^-\frac{1}{\rho_l}]^T \end{aligned} \tag{3.6}$$

Let D^+ and D^- denote the Jacobian matrices of the production and destruction term respectively. Focusing on the destruction term m^-, its Jacobian is given

$$D^- = \frac{\partial \vec{S}_q^-}{\partial \vec{Q}} = \begin{bmatrix} \frac{C_{dest}\rho_v}{\frac{1}{2}\rho_l U_\infty^2}\alpha_l(\frac{1}{\rho_l}-\frac{1}{\rho_v}) & 0 & 0 & 0 & \frac{C_{dest}\rho_v}{\frac{1}{2}\rho_l U_\infty^2}(p-p_v)(\frac{1}{\rho_l}-\frac{1}{\rho_v}) \\ 0 & 0 & 0 & 0 & 0 \\ 0 & 0 & 0 & 0 & 0 \\ 0 & 0 & 0 & 0 & 0 \\ \frac{C_{dest}\rho_v}{\frac{1}{2}\rho_l U_\infty^2}\alpha_l\frac{1}{\rho_l} & 0 & 0 & 0 & \frac{C_{dest}\rho_v}{\frac{1}{2}\rho_l U_\infty^2}(p-p_v)\frac{1}{\rho_l} \end{bmatrix} \tag{3.7}$$

It can simply be proved that the non-zero eigenvalue of D^- is the following:

$$\lambda(D^-) = \frac{C_{dest}\rho_v}{\frac{1}{2}\rho_l U_\infty^2 t_\infty}[\alpha_l(\frac{1}{\rho_l}-\frac{1}{\rho_v})+(p-p_v)\frac{1}{\rho_l}]^T \tag{3.8}$$

This eigenvalue is less than zero for $\rho_v < \rho_l$, a condition that is always satisfied. Thus, the destruction term m^- can be identified as the sink term and will as a result be treated implicitly. This leads to α_l approaching zero exponentially, so that the algorithm remains stable in conditions where significant mass transfer terms cause very low values of the liquid volume fraction.

Following the identical procedure for the production term, it can be shown that m^+ is the source term, which will be treated explicitly.

4 Two-Dimensional Hydrofoils

This chapter includes the results of the numerical simulations of cavitation around the NACA0009 and NACA66MOD hydrofoils. These foils have been used in the bibliography to test and calibrate the accuracy of numerical cavitation prediction, because the obtained cavitation pattern is uniformly spread in the spanwise direction around these hydrofoils. Thus, the two-dimensional numerical results can be compared with the available experimental data. The main interest of this part of the thesis is to properly tune the coefficients of the aforementioned Kunz cavitation model, so that it can accurately reproduce the effects of cavitating flow for different types of geometry and flow.

4.1 NACA0009

4.1.1 Experimental Setup

The first tested geometry is a truncated NACA0009 hydrofoil with the final dimensions of 100mm of chord length and 150mm of span. The hydrofoil is placed in the test section of the EPFL high-speed cavitation tunnel. The rectangular tunnel has the dimensions of 150 x 150 x 750 mm. During the experiment, hydrodynamics forces, pressure and velocity are measured with the focus being placed on the pressure measurements. The operating parameters are the flow angle of attack (α), the upstream velocity (V_∞) and the cavitation number (σ). Further information about the experiments, the measurements and the corrections techniques employed can be found in [35].

4.1.2 Numerical Setup

For the numerical simulation of cavitation around the NACA0009 hydrofoil a 2D computational domain is used, which can be seen in Figure 4.1. The configuration of this domain is the following: the inlet is located 5C upstream and the outlet 10C downstream of the hydrofoil, while the width of the domain equals 2C, where as C is denoted the chord length of the examined foil.

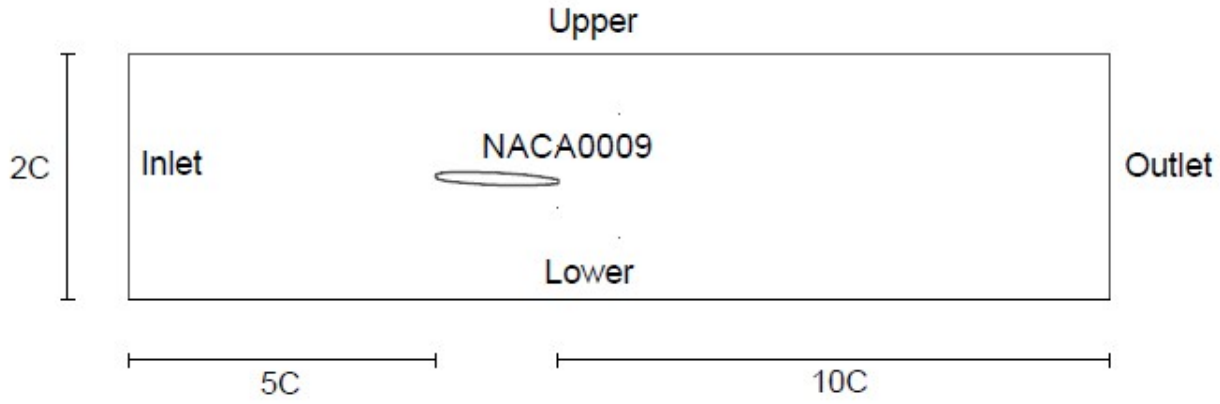

Figure 4.1: NACA0009 Computational Domain

Regarding the aforementioned operating parameters, the flow angle of attack is set to 2.5 degrees, the inlet velocity equals 15 m/s and the cavitation number (σ) , which is tested at 4 different values from 0.75 to 0.90 to test the algorithm's efficiency in different cavitating conditions. All these values respond to the respective conditions used at the experimental tunnel. The initial tests centered around the calibration of the model coefficients and the spatial and temporal independence of the simulation have been performed using one value of the cavitation number, specifically $\sigma = 0.90$. The final results for the pressure distribution and the cavitation pattern are presented for the entirety of the examined cavitation numbers.

The boundary conditions applied to the computational domain are presented in Table 4.1. The normal to surface resolution of the domain (y+) is set equal to 1. For a given cavitation number, the outlet pressure is set in order to achieve the correct value of the saturation pressure, according to equation 1.2. In this particular case, $p_{vap} = 2.800kPa$ and for $\sigma = 0.90$ the outlet pressure is set $p_{outlet} = 104.050kPa$.

Boundary	Velocity	Pressure
Inlet	fixed value	zero gradient
Outlet	zero gradient	fixed value
Upper	slip	zero gradient
Lower	slip	zero gradient
Foil	no slip	zero gradient

Table 4.1: Boundary Conditions for Simulation of Cavitation around NACA0009

4.1.3 Mesh and Timestep Independence Study

The first step in the process of a computational analysis is the independence study of the spatial and temporal discretisation, i.e. the mesh and timestep independence. Both features have to be calibrated appropriately, so that the results of the simulation can be considered credible. This process is described in the present section.

To begin with, two computational meshes were constructed, with the second one being more refined in comparison to the first one. The enhancement of the resolution was implemented at the boundary layer of the hydrofoil and its near surrounding area. The meshes are labeled as Medium and Fine and their specifications are presented in Table 4.2.

Mesh	Number of Cells
Medium	33000
Fine	67000

Table 4.2: Mesh Specifications for NACA0009

A snapshot of the Medium mesh is presented in Figure 4.2 and thereby the meshing technique used for the two-dimensional hydrofoils is also clarified. The grid was refined in two dimensions around the hydrofoil and in the chordwise direction the refinement was more detailed. A thick boundary layer was employed so that the cavitation bubble is located totally inside its limits. This way it is ensured that the extent and the interface of the cavity is accurately predicted. As mentioned before, the first cell has such a height so that the $y^+ = 1$ condition is satisfied.

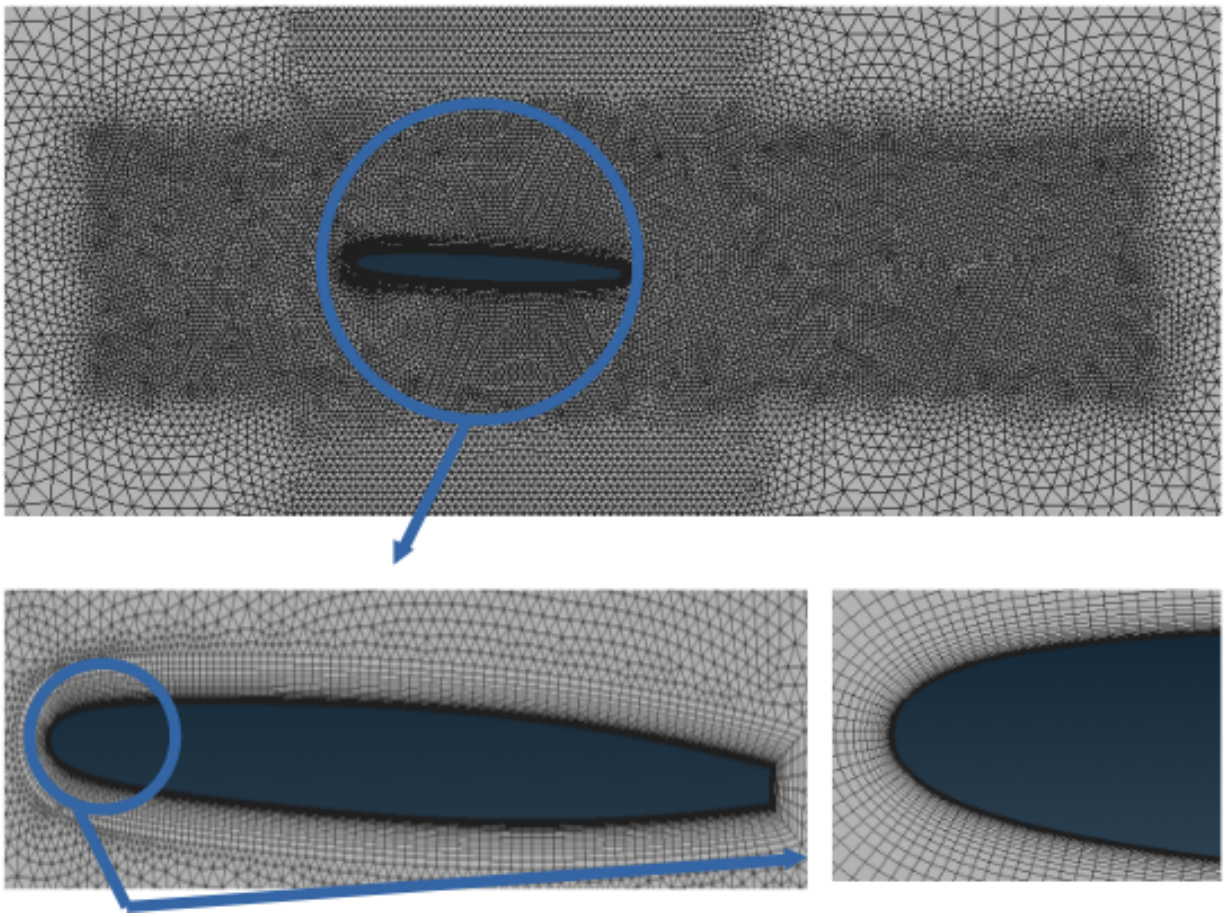

Figure 4.2: NACA0009 Computational Mesh

The simulation results for the pressure distribution coefficient in the framework of the grid independence are compared in Figure 4.3. As it can be seen, the Medium and Fine Grids produce identical results. Thus, the Medium grid was chosen for the simulations due to lower computational cost.

Moreover, the timestep to be used in the simulations was investigated to determine its optimal value. Using the Medium mesh, several timesteps ranging from dt=1e-5 sec to dt=1e-4 sec were tested. Observing the results in Figure 4.4, convergence is demonstrated in a timestep range of dt=1e-5 to 2.5e-5 sec and a timestep of 2.5e-5 sec was selected. The experimental C_p curve is also included so as to act as a reference point for the predicted numerical results.

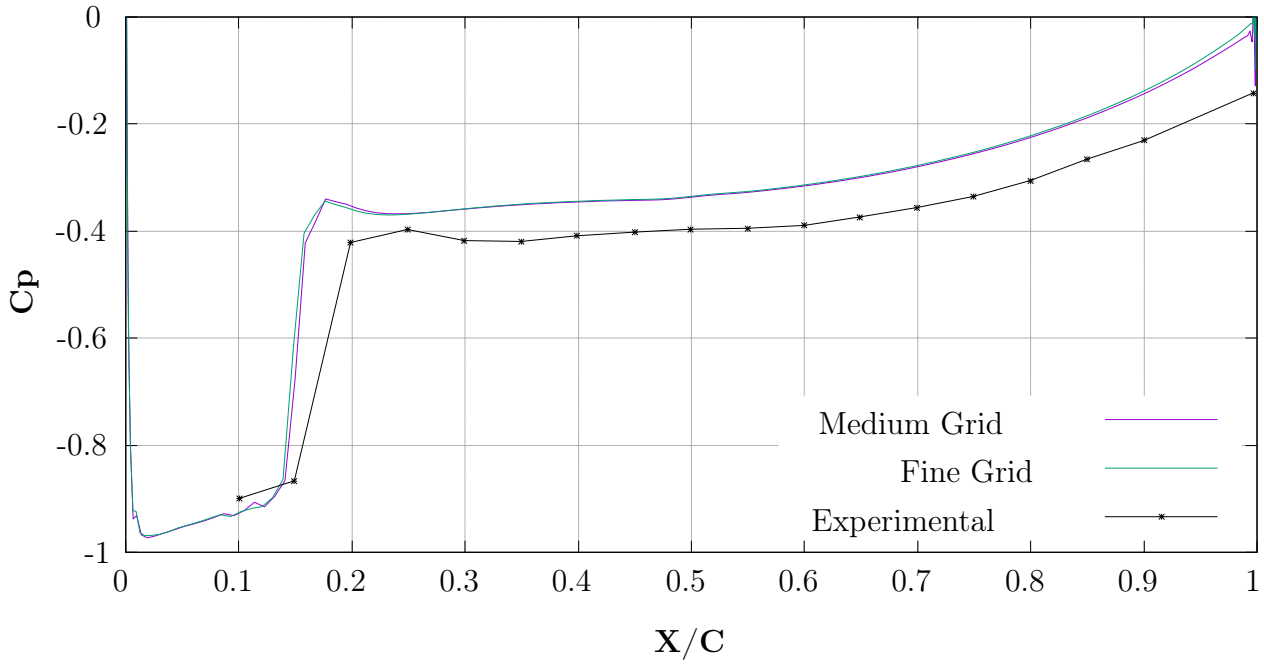

Figure 4.3: Grid Independence Study for NACA0009 for $\sigma = 0.9$

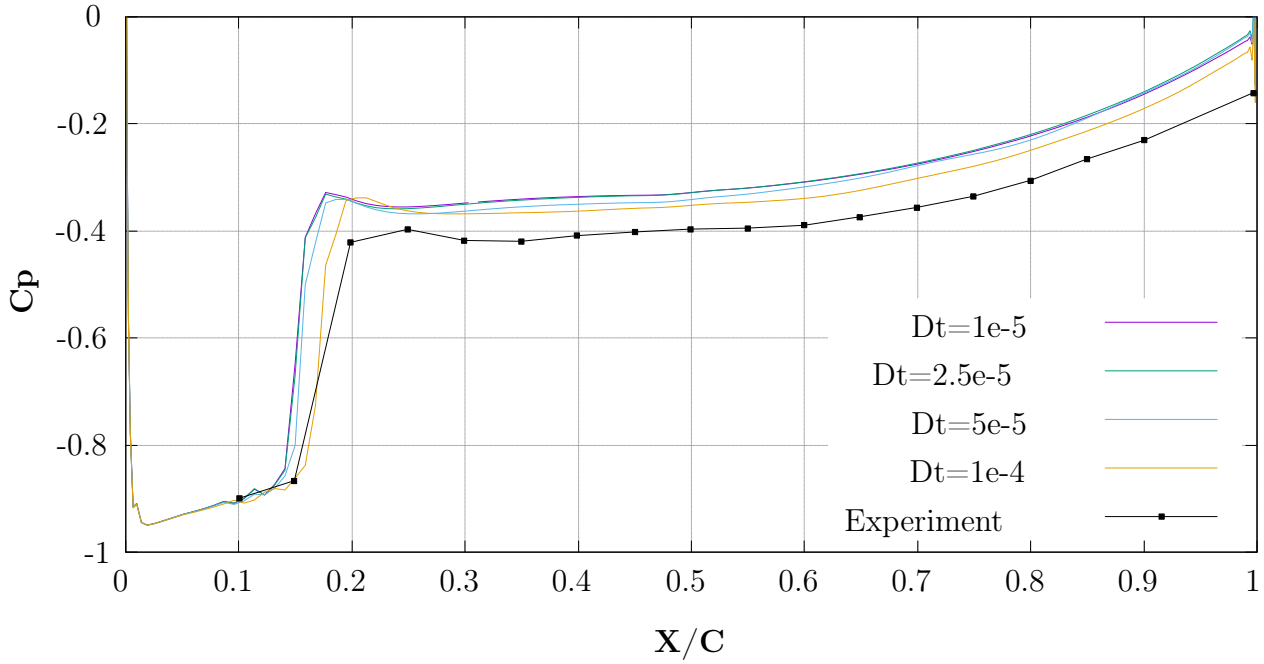

Figure 4.4: Timestep Independence Study for NACA0009 for $\sigma = 0.9$

4.1.4 Cavitation Model Coefficients Calibration

As presented both in Chapter 1 and Chapter 3, the main issue in cavitation modeling with a transport equation model like the Kunz model that is employed in the present study, is the dependency on empirical coefficients. These coefficients have to be properly calibrated for the model to produce the sought results. Many studies regarding the optimisation or the calibration of these coefficients have been conducted ([11], [32], [10], [36]) using different solvers and they all arrive at a different set of optimal empirical coefficients. The conclusion that is derived from this observation is that the optimal range for these coefficients is primarily dependent on the employed solver. It has to be noted that the following parametric studies were conducted for a value of $\sigma = 0.9$.

Hence, a parametric study for each of the two empirical coefficients involved was conducted to determine their suitable values to perform cavitation simulation with MaPFlow. The present thesis is not focused on the optimisation of the model coefficients, so the goal set is to determine the intervals where the simulations show convergence for the chosen values of C_{prod} and C_{dest}. This area of convergence is preferred since the numerical solution displays stability. In order to achieve that, various values of both factors were used and the pressure coefficient graphs were compared. The analysis had the originally proposed model coefficients $(C_{dest}, C_{prod}) = (100, 100)$ as a starting point.

Firstly, the effect of the condensation coefficient is studied. As it was mentioned in the previous chapter, this factor dictates the pressure gradient at the closure of the cavity. High values of C_{prod} cause high pressure gradient values and thus destabilize the algorithm, which is more sensitive to this parameter than to C_{dest}. Specifically, for $C_{prod} \geq 500$ the pressure gradients become too steep at the closure region and the code is not stable. The most stable behavior is obtained for values in the interval [100,400], for which the pressure coefficient distribution is presented in Figure 4.5. Convergence is observed in the range of $C_{prod} \in [300, 400]$.

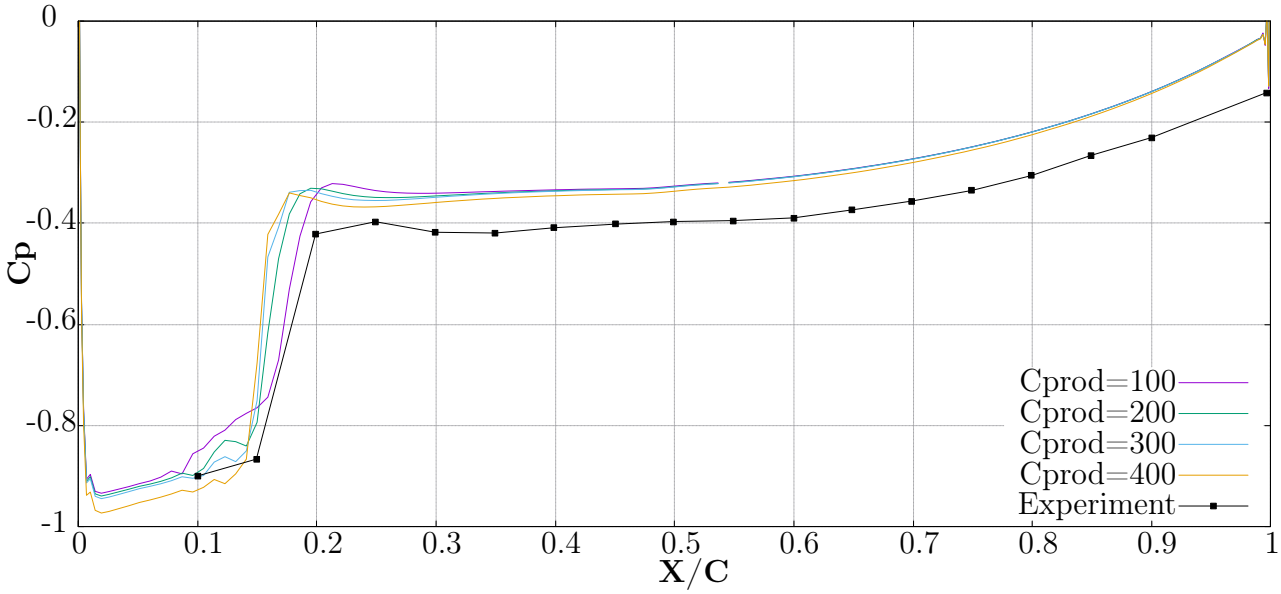

Figure 4.5: Influence of C_{prod} in cavitation simulation of NACA0009 for $\sigma = 0.9$

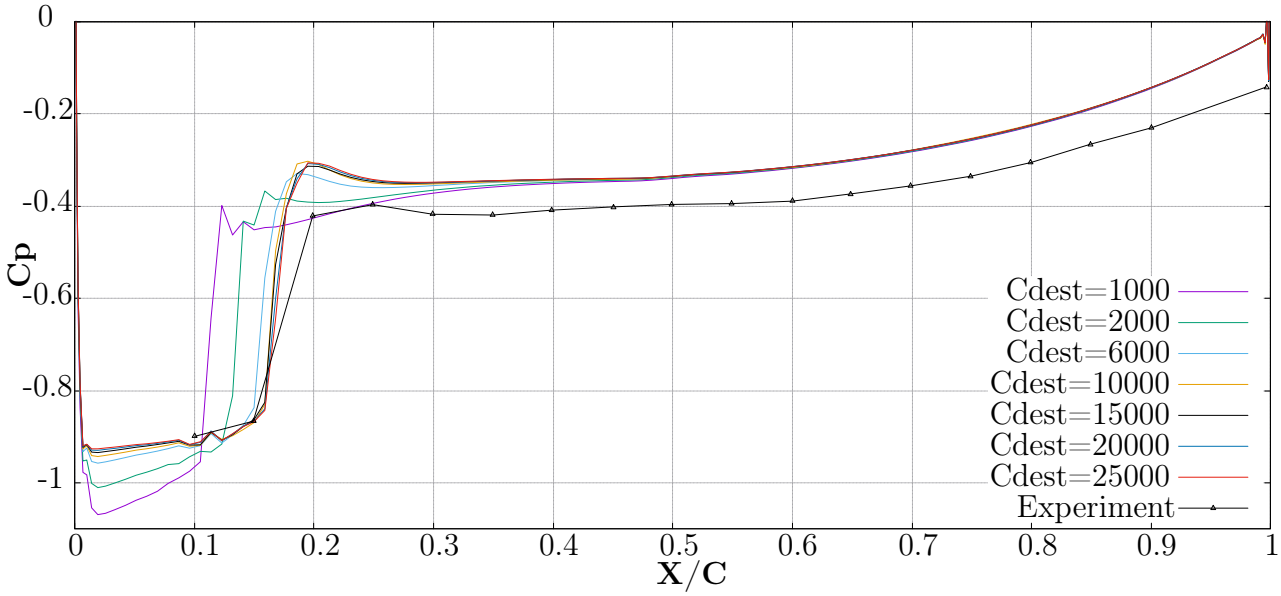

Figure 4.6: Influence of C_{dest} in cavitation simulation of NACA0009 for $\sigma = 0.9$

Consequently, a similar analysis is performed to find the convergence interval of the evaporation coefficient. It has been mentioned that the length of the cavity depends on the value of C_{dest}. Beginning from the value of $C_{dest} = 100$ that was originally proposed by Kunz, it was observed that values of this magnitude do not provide sufficient results in MaPFlow. Thus, the performed analysis contains values of $C_{dest} \geq 1000$, as it is seen in Figure 4.6. The model is proved to be significantly stable with respect to this parameter and, as a result, many values were tested. Convergence is observed in the range of $C_{dest} \geq 8000$.

From the analysis executed, it was determined that the pair of coefficients to be used in the cavitation simulation is C_{dest}=15000 and C_{prod}=400. The following results of the pressure distribution and the cavitation pattern around the NACA0009 hydrofoil have been calculated with this set of model coefficients.

As it has been mentioned, the calibration process of the model coefficients was carried out for the value of the cavitation number $\sigma = 0.9$. However, a short analysis for the values of the empirical factors for the other cavitation number was also conducted and the findings were identical to the ones of the original parametric analysis. Thus, the aforementioned set of model coefficients was determined to be satisfactory for all the different cavitating flows.

4.1.5 Pressure Distribution

The pressure coefficient distribution was calculated and compared with the experimental results to validate the model's ability to accurately predict cavitation for different cavitation numbers. As it can be seen in Figures 4.7, 4.8, 4.9 and 4.10, the computational results show very good agreement with the experimental ones in the first two cases and thus, it can be concluded that MaPFlow successfully predicts cavitating flow around NACA0009 for the larger values of σ. The algorithm properly models the increase in cavity length for lower values of the cavitation number. One observation that has to be made, however, is that the numerical prediction is deteriorating with respect to accuracy for lower values of the cavitation number. Lower values of σ constitute the cavitating phenomena more intense and are thus more challenging to be predicted accurately.

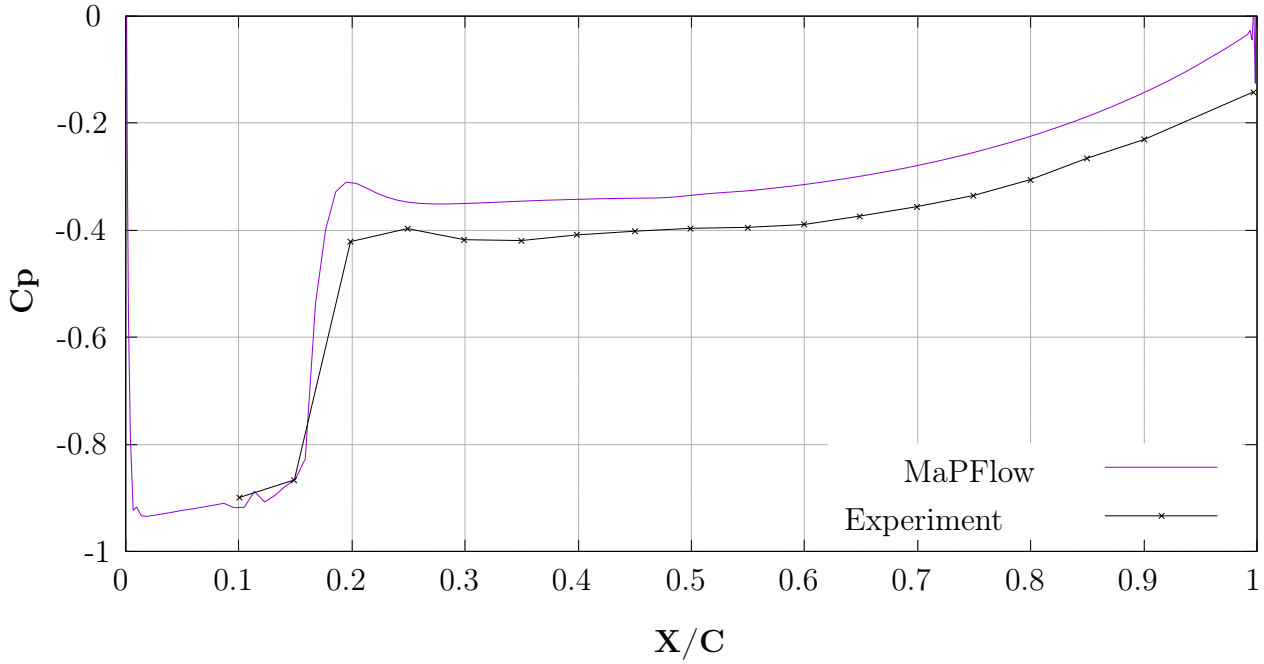

Figure 4.7: Pressure Coefficient Distribution around NACA0009 for $\sigma = 0.9$

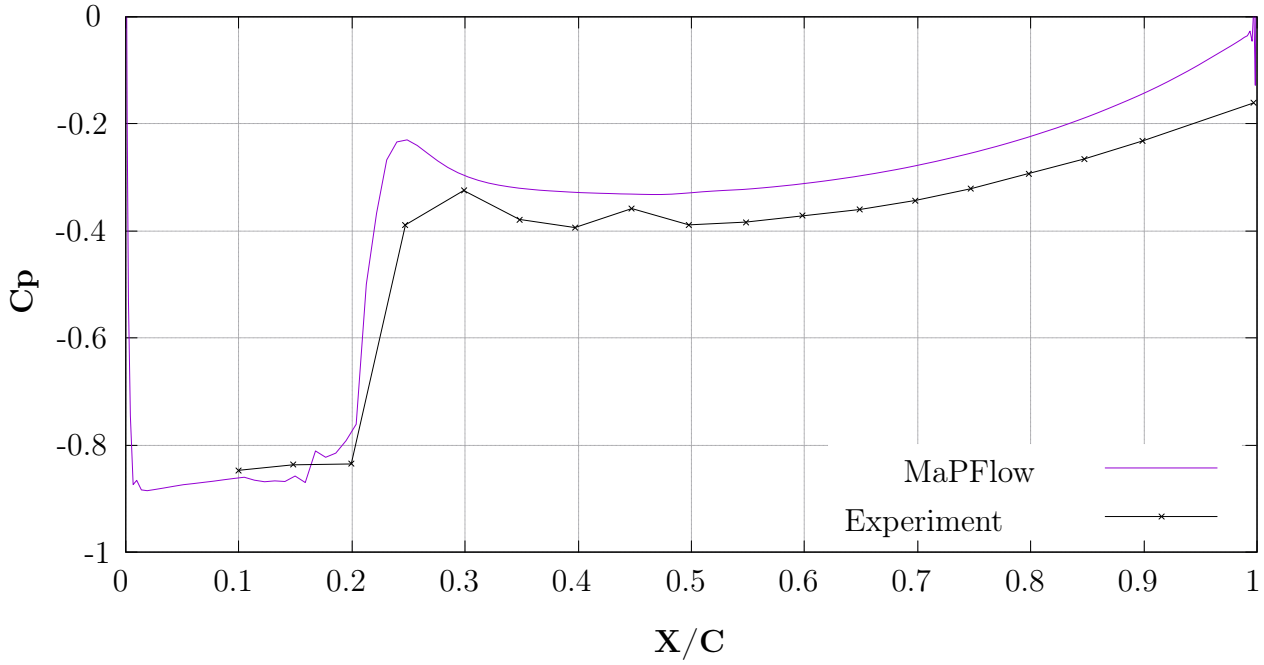

Figure 4.8: Pressure Coefficient Distribution around NACA0009 for $\sigma = 0.85$

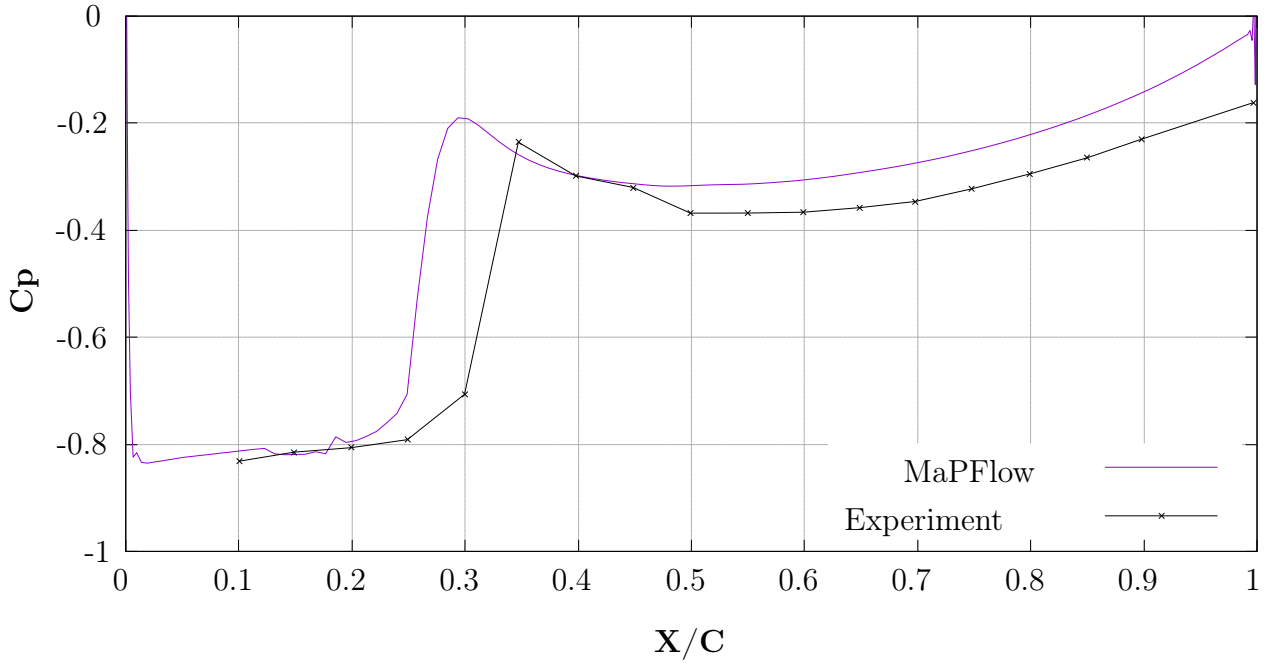

Figure 4.9: Pressure Coefficient Distribution around NACA0009 for $\sigma = 0.80$

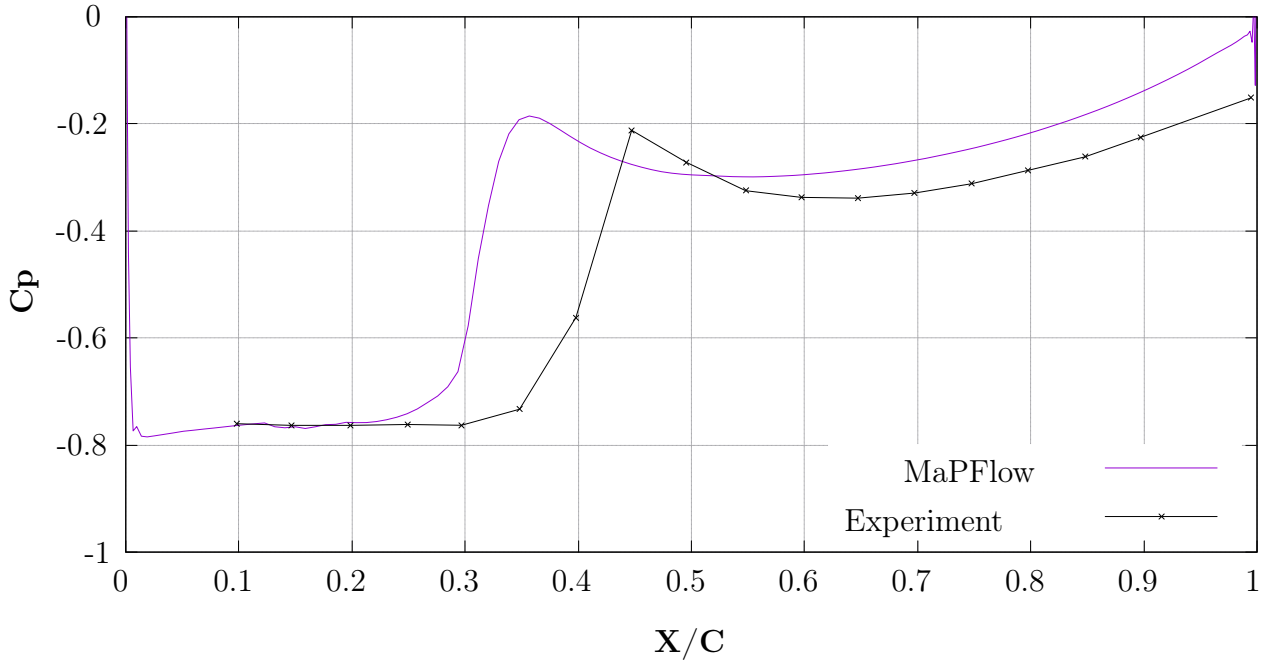

Figure 4.10: Pressure Coefficient Distribution around NACA0009 for $\sigma = 0.75$

4.1.6 Cavitation Pattern

Finally, the vapor volume fraction of the domain was visualized to obtain the shape of the formed vapor bubble around the hydrofoil for the examined cavitation numbers. As it can be seen, the model successfully reproduces the expected increase in cavitation area with the decrease of the cavitation number. Figures 4.11, 4.12, 4.13 and 4.14 illustrate the extent of the cavity with reference to the hydrofoil chord, so that the cavity growth is made clear. Additionally, a closer look into the cavity closure is presented, along with the scale of the used contour for clarity.

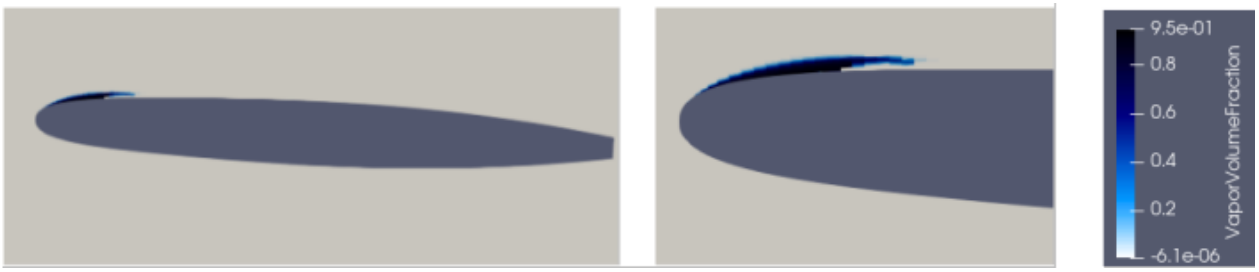

Figure 4.11: Vapor Volume Fraction around NACA0009 for $\sigma = 0.9$

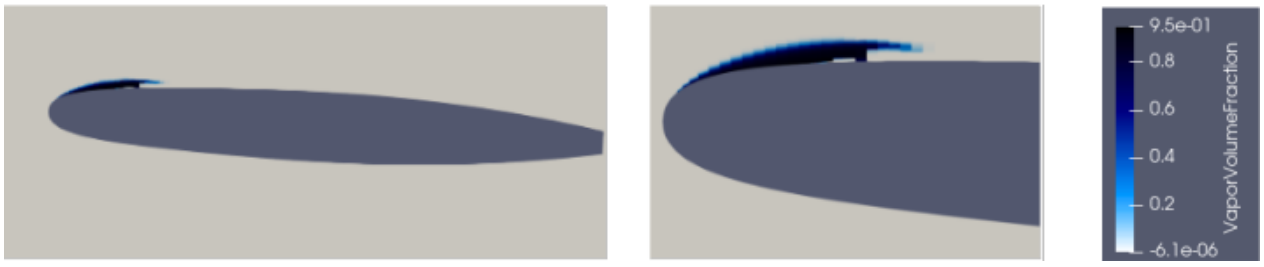

Figure 4.12: Vapor Volume Fraction around NACA0009 for $\sigma = 0.85$

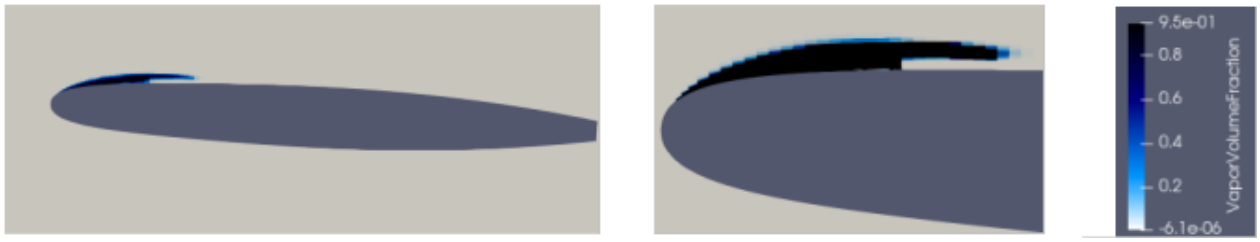

Figure 4.13: Vapor Volume Fraction around NACA0009 for $\sigma = 0.8$

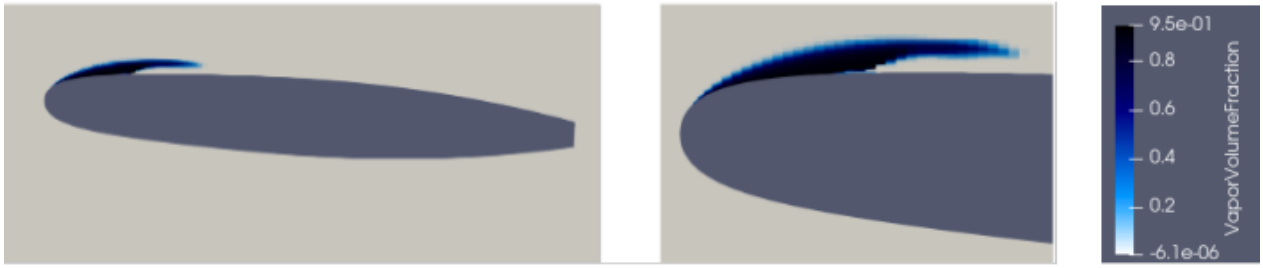

Figure 4.14: Vapor Volume Fraction around NACA0009 for $\sigma = 0.75$

4.2 NACA66MOD

4.2.1 Experimental Setup

The second test case used to assess the cavitation prediction algorithm is a modified NACA 66 hydrofoil tested in the High Speed Water Tunnel in the Graduate Aeronautical Laboratories of the California Institute of Technology. The foil was modified to meet the tunnel requirements and is thus called NACA66 MOD. It is designed with a camber ratio of f/c=0.020, a NACA meanline of a=0.8 and a thickness ratio of t/c=0.9, where f is the maximum thickness, t the maximum camber and c = 0.150 m the chord length of the hydrofoil [37]. Similar to the first test case, different operating conditions were tested and measurements were conducted for the pressure and the cavity size.

4.2.2 Numerical Setup

For the numerical simulation of cavitation around the NACA66MOD hydrofoil a 2D computational domain is used identically to the first test case. The configuration of this domain can be observed in Figure 4.15 and its specifications are the following: the inlet is located 5C upstream and the outlet 10C downstream of the hydrofoil, while the width of the domain equals 5C, where as C is noted the chord length of the examined foil.

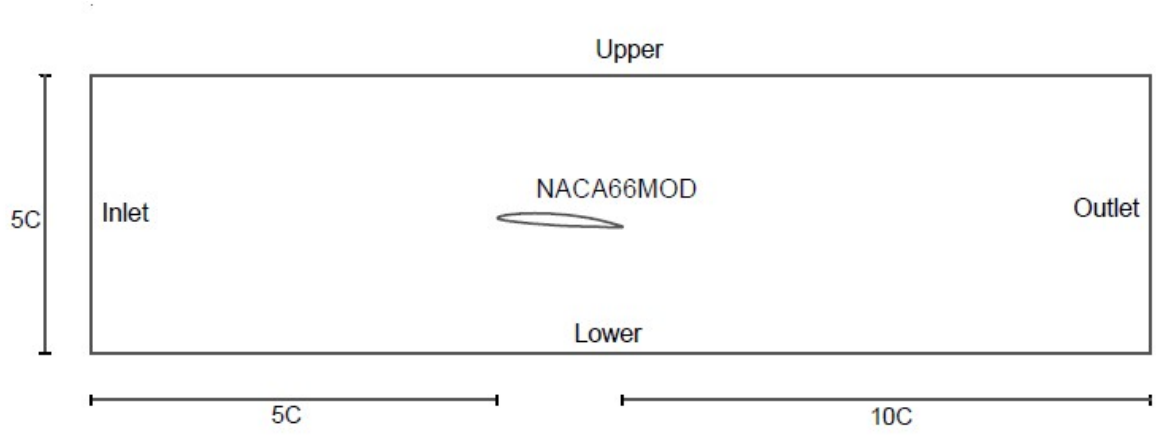

Figure 4.15: NACA66MOD Computational Domain

In order to imitate the flow conditions of the experiment, a flow Reynolds number of 2 x 10^6 is kept constant. Additionally, the flow angle of attack is set to 4 degrees, the inlet velocity equals 12.2 m/s and three different values of the cavitation number (σ) , namely 0.84, 0.91 and 1.0 have been examined. The preliminary studies for the calibration of the model and the simulation configuration have been performed using one value of the cavitation number, specifically $\sigma = 1$. The final results for the pressure distribution and the cavitation pattern are presented and compared with the experimental data for all three different cavitation numbers.

The boundary conditions applied to the computational domain are presented in Table 4.3. The normal to surface resolution of the domain (y+) is set equal to 1.

Boundary	Velocity	Pressure
Inlet	fixed value	zero gradient
Outlet	zero gradient	fixed
Upper	slip	zero gradient
Lower	slip	zero gradient
Foil	no slip	zero gradient

Table 4.3: Boundary Conditions for Simulation of Cavitation for NACA66MOD

4.2.3 Mesh and Timestep Independence Study

Following the same procedure like in the first test case, two computational meshes of increasing resolution were compared and their specifications are presented in Table 4.4 below.

Mesh	Number of Cells
Medium	66000
Fine	110000

Table 4.4: Mesh Specifications for NACA66MOD

A snapshot of the Medium mesh is given in Figure 4.16. The first image sheds light on the mesh refinement used around the hydrofoil in the direction of both axes. The second and third images describe the boundary layer around NACA66 MOD in a broad and more detailed view respectively.

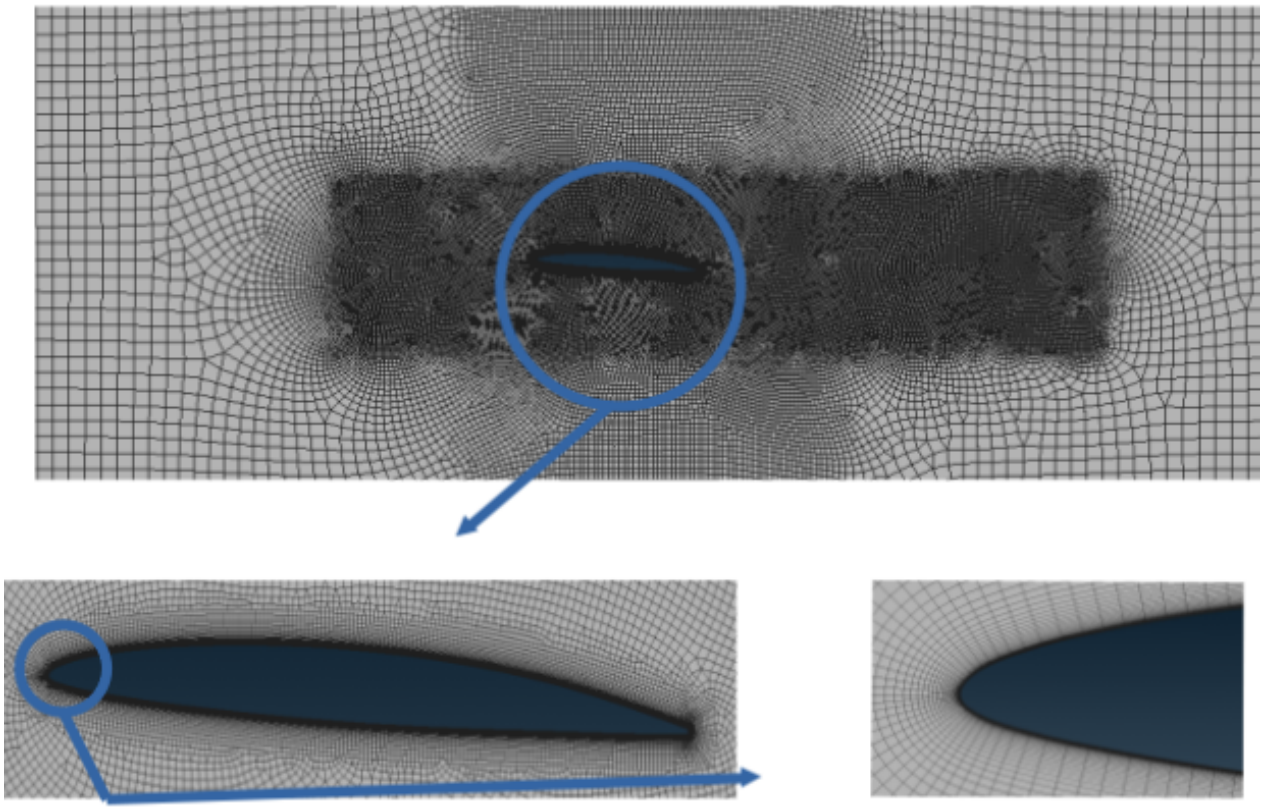

Figure 4.16: NACA66MOD Computational Mesh

The flow was simulated using the meshes above in cavitating conditions. The results are gathered and compared in Figure 4.17. As it can be seen, the Medium and Fine Grids produce identical results. As a result, the Medium grid was chosen for the simulations due to lower computational cost.

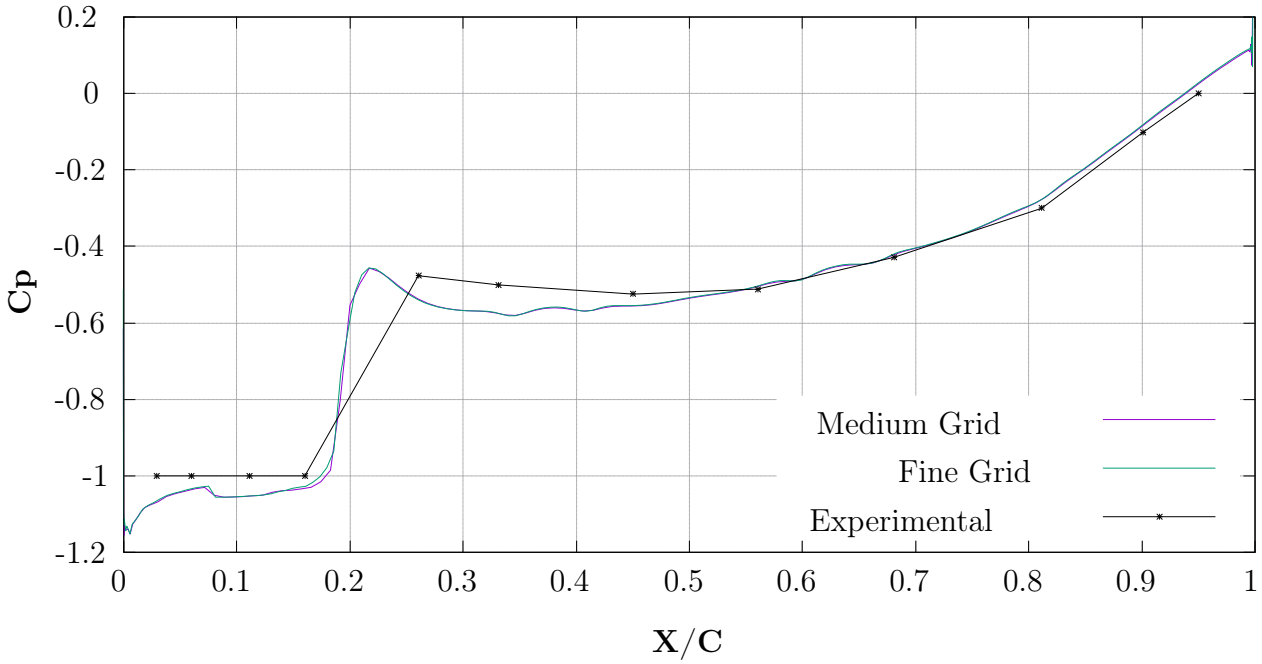

Figure 4.17: Grid Independence Study for NACA66MOD for $\sigma = 1.0$

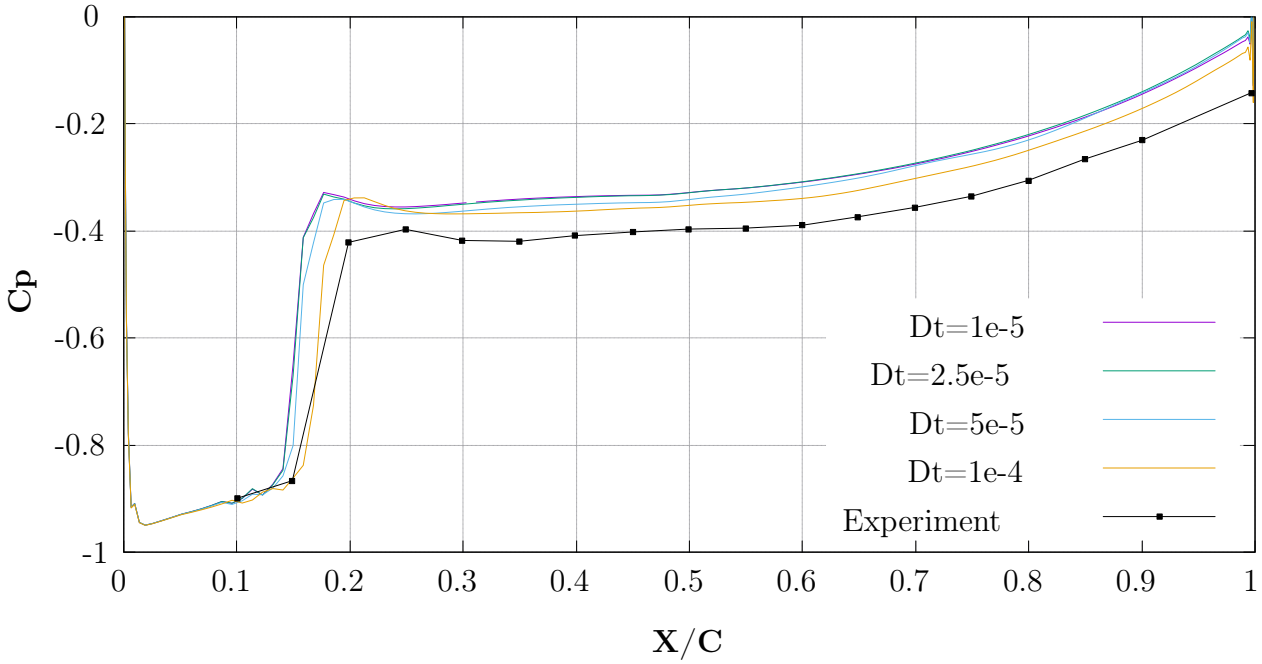

Figure 4.18: Timestep Independence Study for NACA66MOD for $\sigma = 1.0$

The influence of the timestep used in the simulations was also investigated. The computational results are shown in Figure 4.18. Several timesteps ranging from dt=1e-5 sec to dt=2e-4 sec were tested and compared.Observing that the graphs demonstrate convergence in a timestep range of dt=1e-5 to 2.5e-5 sec, a timestep of 2.5e-5 sec was selected.

4.2.4 Cavitation Model Coefficients Validation

As it was performed for the first test case, the cavitation model coefficients were investigated with respect to their impact on the simulation results. The focus here was to validate the results of the first parametric analysis and determine if the chosen set of empirical factors can be also employed for the simulations around other geometries and flows. It has to be noted that the following parametric studies were conducted for a value of $\sigma = 0.9$.

The observations were identical to the case of the NACA0009 hydrofoil, which can be observed in Figures 4.20 and 4.19 presented below. The only difference spotted is that the production coefficient C_{prod} does not destabilise the simulation for larger values, unlike the first hydrofoil. However, the convergence region remains the same. The final pair of model coefficients used for this test case is identical to the first test case, namely C_{evap}=15000 and C_{cond}=400. Both coefficients are in their zone of convergence and the simulations results show very good agreement with the experimental data for pressure coefficient distribution. The calibration of the model coefficients was carried out for the value of the cavitation number $\sigma = 1.0$. Like in the first test case, a short parametric study for the empirical factors for the other cavitation number was also conducted and the results were identical to the ones of the original analysis.

The most important takeaway from this analysis regarding the convergence intervals and chosen values for C_{prod} and C_{dest} is the fact that the convergence remained identical for different geometries and flows tested. The chosen values for the coefficients could predict the intended cavitating behavior in completely different simulation conditions. This leads to the conclusion that, once these coefficients have been calibrated according to the needs of the used solver, they can be employed for the simulation of other geometries and flows. This is also supported by the findings of other research works, like [11], as well as by the findings of the present work regarding the test cases investigated in the following chapters of the study.

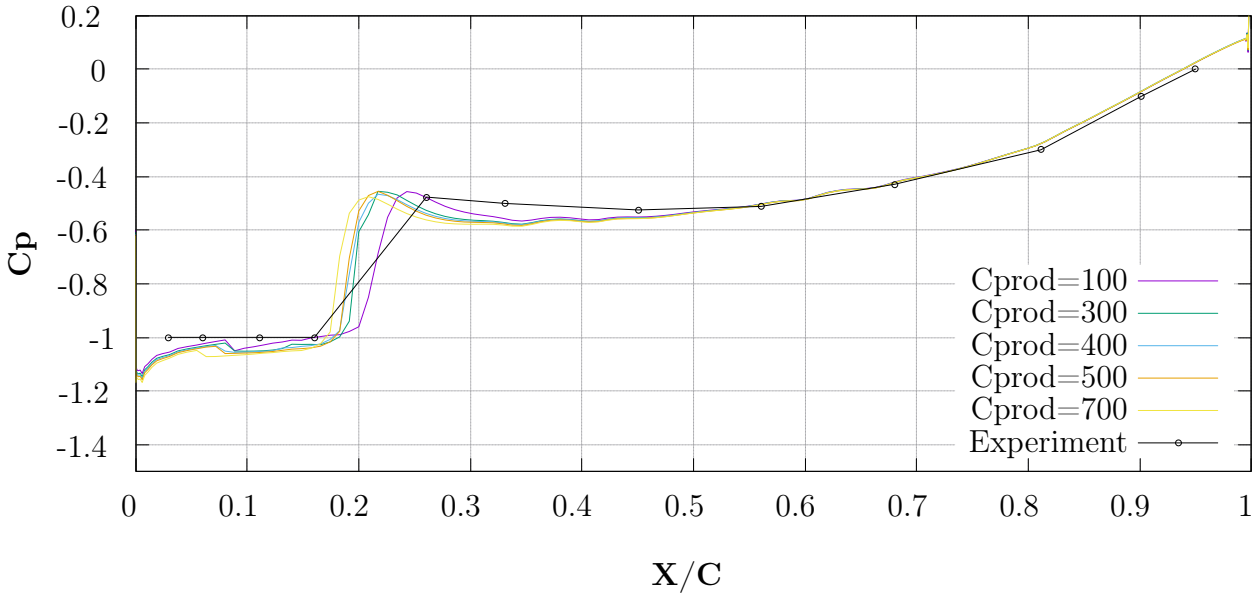

Figure 4.19: Influence of C_{prod} in cavitation simulation around NACA66MOD for $\sigma = 1.0$

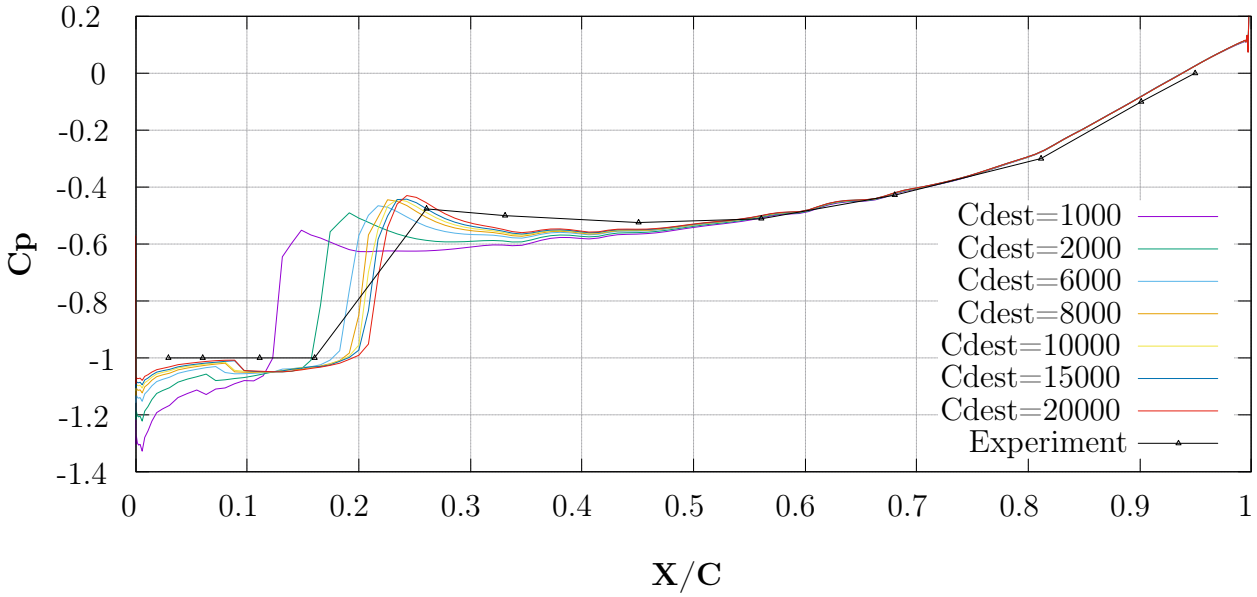

Figure 4.20: Influence of C_{dest} in cavitation simulation around NACA66MOD for $\sigma = 1.0$

4.2.5 Pressure Distribution

Like in the first test case, the pressure coefficient distribution was calculated and compared with the experimental results for different cavitation numbers. As it can be seen in Figures 4.21, 4.22 and 4.23, the computational results show good agreement with the experimental ones in all three cases and thus, it can be concluded that MaPFlow successfully predicts cavitating flow around NACA66MOD. The prediction accuracy decreases for lower values of the cavitation number, an observation that was also made for the first hydrofoil tested.

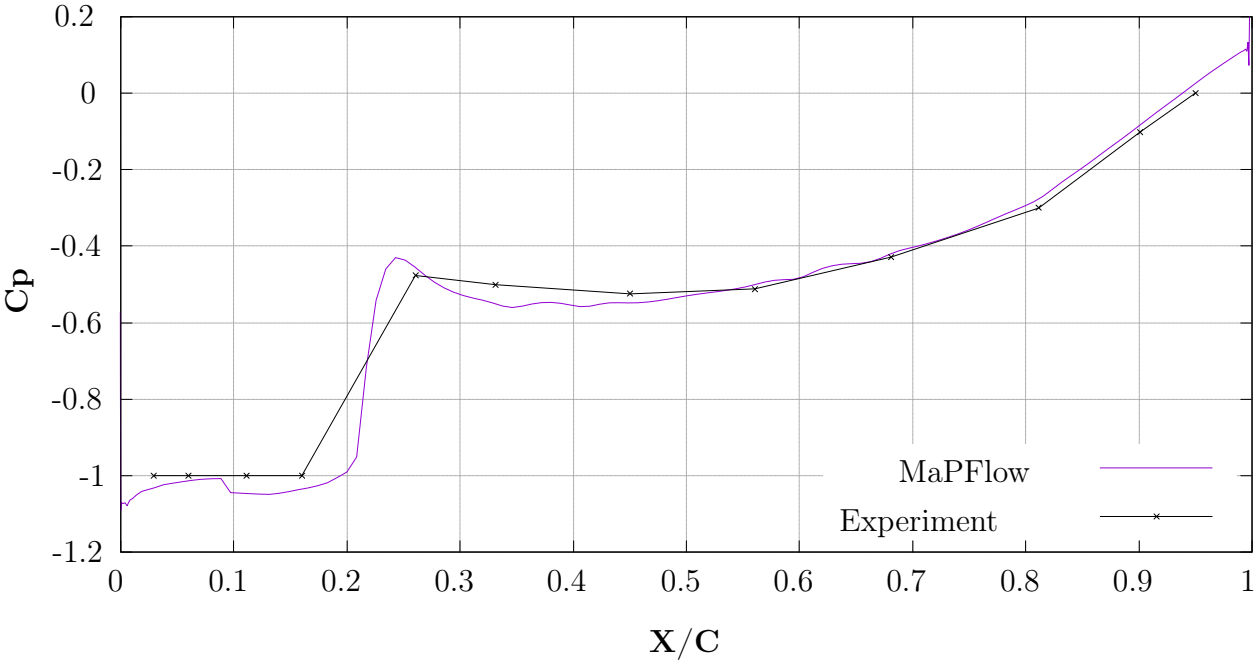

Figure 4.21: Pressure Coefficient Distribution around NACA66MOD for $\sigma = 1$

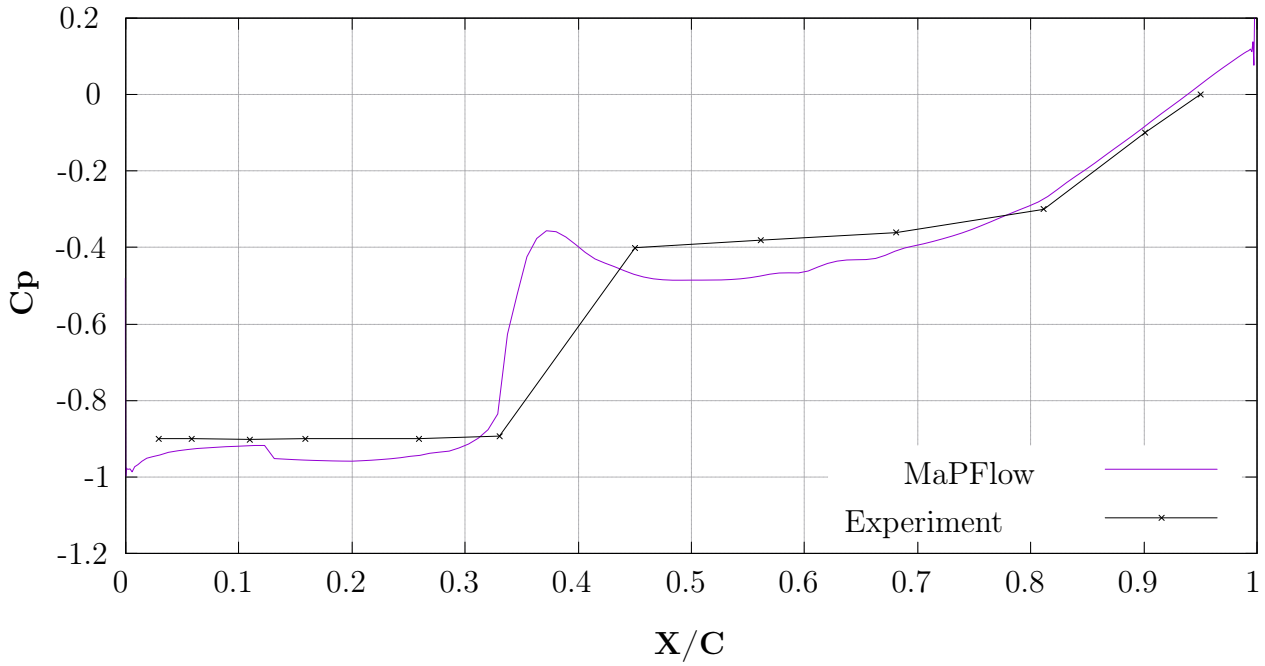

Figure 4.22: Pressure Coefficient Distribution around NACA66MOD for $\sigma = 0.91$

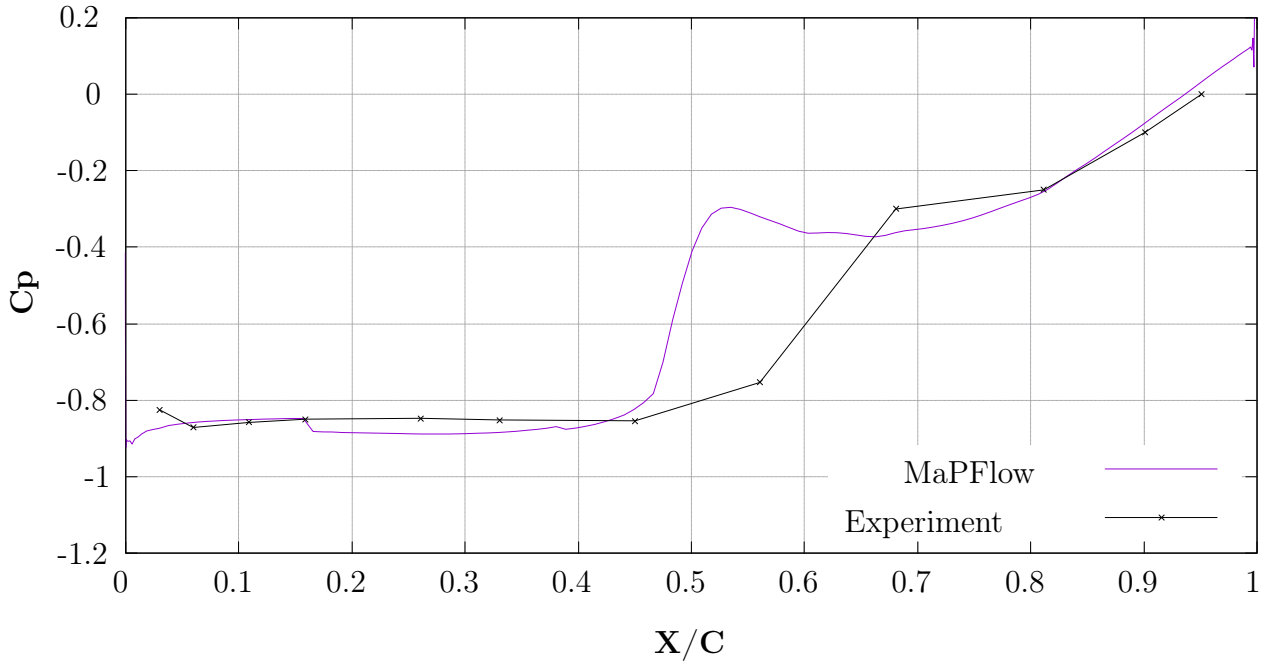

Figure 4.23: Pressure Coefficient Distribution around NACA66MOD for $\sigma = 0.84$

4.2.6 Cavitation Pattern

Finally, the vapor volume fraction of the domain was visualized to obtain the shape of the formed bubble around the hydrofoil for the three examined cavitation numbers (Figures 4.24, 4.25, 4.26) . As it can be seen, the model reproduces the expected increase in cavitation area with the decrease of the cavitation number. Identically to the first test case, the cavity extent is given with reference to the chord length and in a closer look.

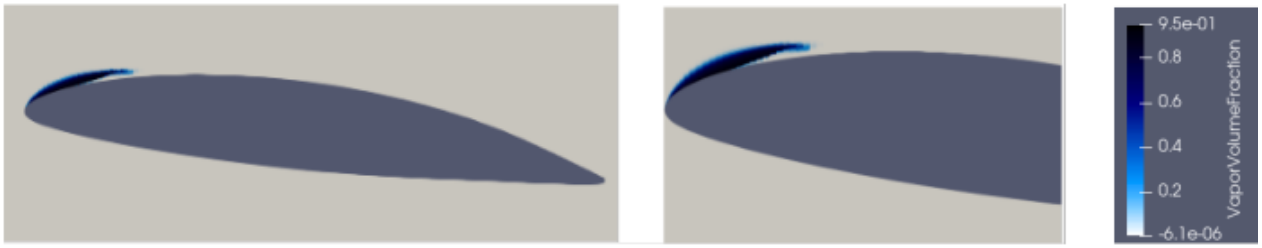

Figure 4.24: Vapor Volume Fraction around NACA66MOD for $\sigma = 1$

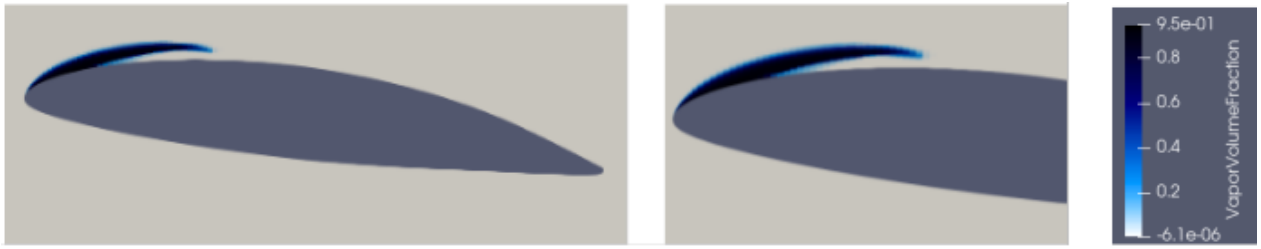

Figure 4.25: Vapor Volume Fraction around NACA66MOD for $\sigma = 0.91$

Figure 4.26: Vapor Volume Fraction around NACA66MOD for $\sigma = 0.84$

5 Three-Dimensional Hydrofoil

The next step in the assessment of the implemented algorithm concerns the numerical study of cavitation around a three-dimensional hydrofoil, specifically the Delft Twist11 hydrofoil. Twisted foils have been widely tested in the field of cavitation research, as they generate cavitation resembling the one of propellers. However, the experimental and computational setup is simpler and more well defined than in the case of propellers due to the lack of the rotating body. Therefore, the twisted hydrofoils have become an important test case to assess numerical approaches to accurately predict the cavitation phenomenon.

5.1 Delft Twist11 Hydrofoil

The Delft Twist11 Hydrofoil is an important case for the numerical study of cavitation, as it tests the algorithms' capability to predict the unsteady sheet cavitation that occurs around the foil. The cavitation bubble demonstrates a periodic character, in which it is shed and regenerated within a constant time frame.

However, apart from the useful conclusions that can be drawn, simulating the unsteady sheet cavitation around the Delft Twist 11 hydrofoil poses a major challenge in numerical modeling. Many recent works like [38] have clearly demonstrated that the results are not only influenced by the cavitation model, but they are also heavily dependent on the turbulence modeling. The standard two-equations turbulence models like the $k-\omega$ SST fail to capture the unsteady cavity dynamics. This has been found to be a result of the overproduction of the turbulent viscosity at the cavity closure and its downstream region [39]. This excessive viscosity dampens the inherent unsteadiness of sheet cavitation and thus the models show inability to accurately predict the phenomenon.

To overcome this problem with the RANS method, several modifications on the turbulence modeling have been proposed. The most used method is the Reboud modification [40]. This approach, which belongs to the category of Density-correction methods (DCM), has shown improved results regarding cavity shedding and formation. Further information regarding this

modification is given in section 5.5. Other approaches , which have been recently introduced to improve RANS modeling are the Filter-based methods (FBM) [41], the filter-based density correction methods [42] and the interface-effect based model [43], have not been as widely applied and tested.

Other studies have applied more detailed approaches on the turbulence of the flow such as LES [44], DES [45] and Detached Delayed Eddy Simulations (DDES) [46] . It has been observed that these methods offering higher resolution have been more successful in simulating the experimental results than the RANS methods. However, the increase of the computational cost is very significant.

In the present study, the RANS approach with the standard $k-\omega$ SST model was compared with the modified $k-\omega$ SST model according to Reboud [40]. Both models were assessed as to their accuracy in predicting unsteady cavitation.

5.2 Unsteady Cavitation Mechanism

Unsteady sheet cavitation appears in two- and three-dimensional cases, in both of which the cavitation cloud is shed and regenerated over time. The shedding of the cavity occurs due to the re-entrance of the flow into the downstream region of cavity, something referred to as re-entrant jet [47].

A short analysis of the two- dimensional phenomenon is presented so that the more complex three-dimensional phenomenon - which is the one examined in the present work- can be more easily understood. In the 2D case, the re-entrant jet moves upstream towards the leading edge along the surface of the foil underneath the vapor sheet. At some point the re-entrant jet impinges on the liquid-vapor interface leading to separation or shedding of part of the cavity. This shedded bubble cloud is then advected by the main flow in downstream direction. The cavity is regenerated back to its original size and the shedding process repeats itself. The aforementioned stages of this mechanism are graphically presented in Figures 5.1 (a)-(f), as illustrated by De Lange and De Bruin [48].

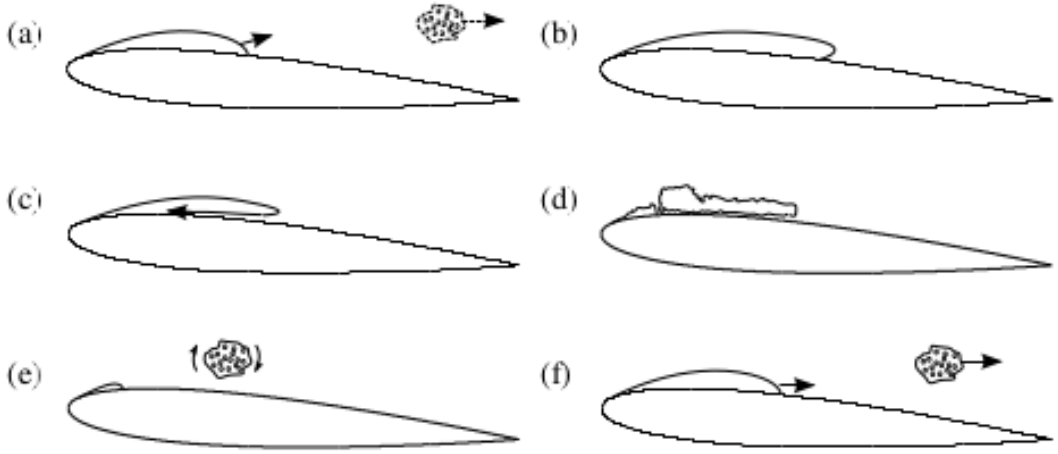

Figure 5.1: Two-Dimensional Cavitation Shedding Mechanism, reproduced from De Lange and De Bruin [48]

Regarding the three dimensional sheet cavitation on the Delft Twist11 hydrofoil, the work of Foeth [49] provides a detailed insight on the phenomenon and its mechanism. As it was mentioned, sheet cavitation around the foil is formed, shed and regenerated in a periodic way. The component dictating this behavior is the re-entrant flow inside the cavity area, exactly like the two-dimensional case. The main difference of the three-dimensional case consists in the spanwise component of the re-entrant flow. Thus, a distinction is made between two types of re-entrant flow based on their direction, which are described by the following terms:

- Re-entrant jet, which refers to the part of the flow traveling upstream along the foil's surface.
- Side-entrant jet, which denotes the part of the re-entrant jet with direction from the cavity sides to its center.

A schematic representation of the shedding mechanism is presented in Figure 5.2, reproduced from Foeth [50]. These sketches focus on the re-entrance of the flow and the shedding of the cavity, while the separated bubble cloud following the flow downstream is not regarded. However, it has to be pointed out that this bubble cloud is present similarly to the way it is depicted in Figure 5.1.

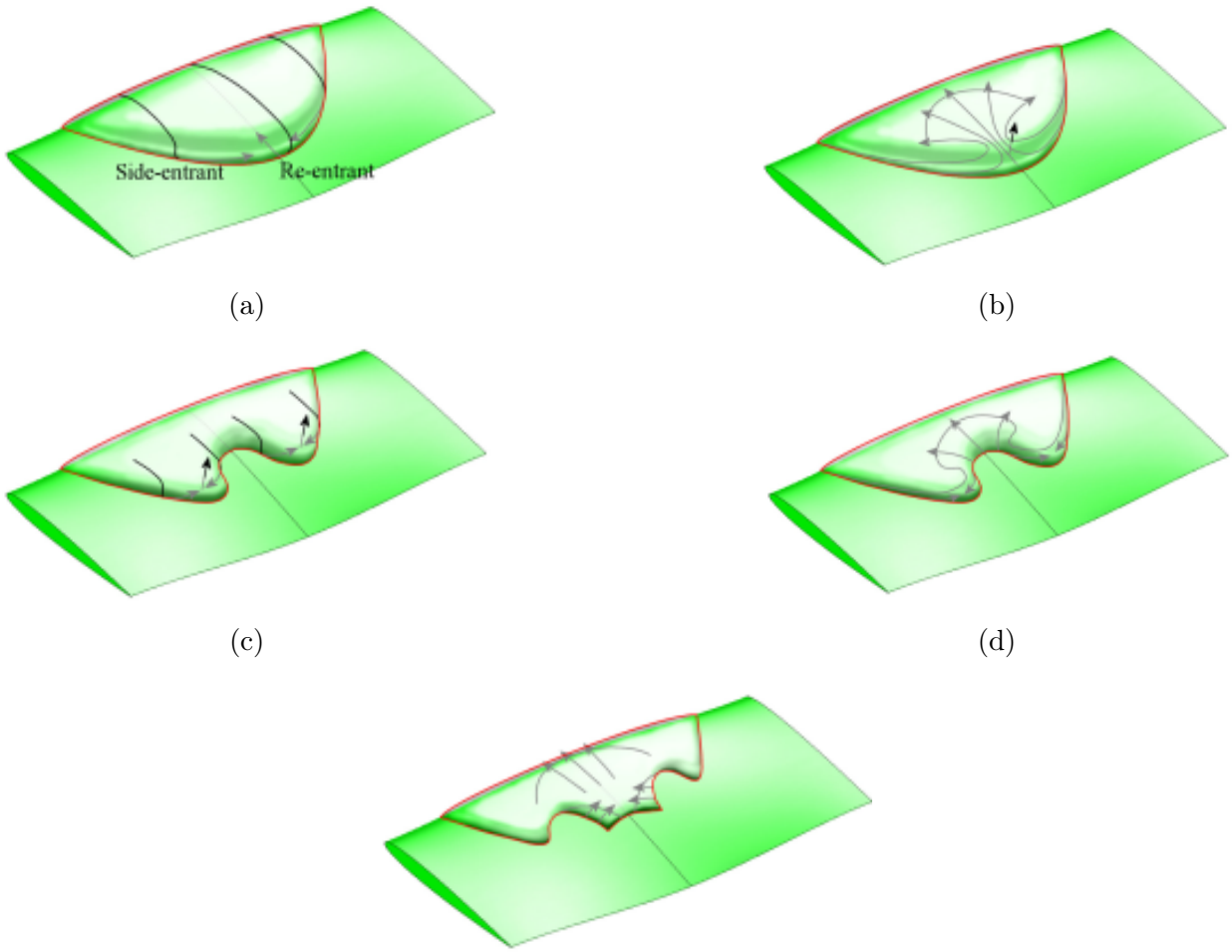

Figure 5.2: Three-Dimensional Cavitation Shedding Mechanism, reproduced from Foeth [50]

In Figure 5.2a the cavity is at full growth and the distinction between side-entrant and re-entrant jets is made clear. In Figures 5.2b-5.2d the shedding process is illustrated. The side-entrant jets collide with each other and part of the vapor cloud gets detached from the cavity, forming the convex-shaped vortex. Finally, in Figure 5.2e the regeneration process of the cavity takes place.

5.3 Geometry and Experimental Setup

As far as the geometry of the hydrofoil is concerned, the profile is of a modified NACA0009 section, the chord length equal to 0.15m and the span equals 0.30m [51]. The twisted foil has been constructed through a spanwise geometric angle of attack variation of the section profile. The angle of attack variation is symmetric in respect to the mid-span plane of the hydrofoil. At the edges, the angle has the value of 0 degrees, which rises up to 11 degrees at the center of the wing. For the following study, the foil has also been rotated -2 degrees (leading edge downward). Figure 5.3 offers three different views of the hydrofoil geometry so as to provide a full definition of the tested geometry.

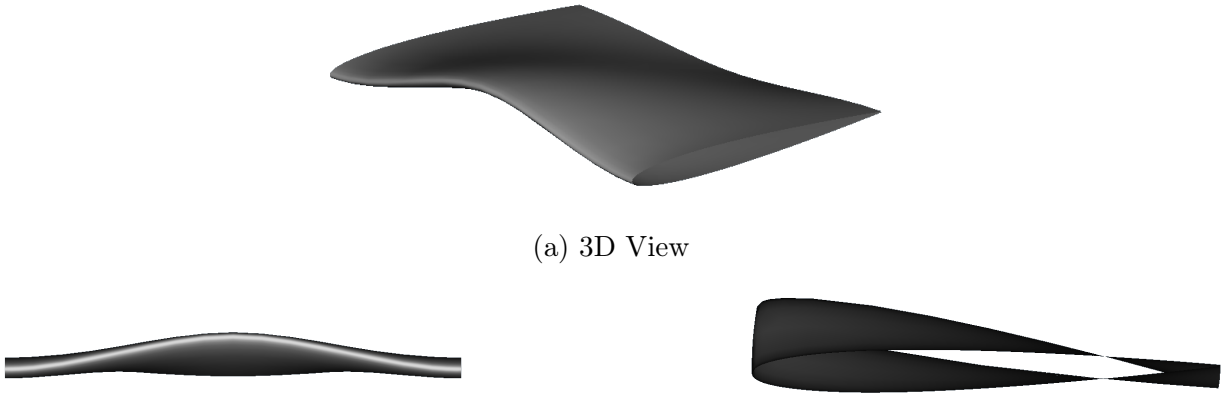

(a) 3D View

(b) Fore View

(c) Side View

Figure 5.3: Delft Twist11 Geometry

The experimental tests for the Delft Twist11 Hydrofoil were carried out in the cavitation tunnel at Delft University. More information regarding the experiments can be found in [49]. The observed experimental cavity is three dimensional with a convex-shaped closure line. Moreover, it is to be noted that sand grains are applied to the leading edge of the geometry so that the flow becomes fully turbulent. With this extra roughness possible effects of the laminar boundary layer on the cavitation phenomenon are eliminated.

5.4 Numerical Setup

For the simulation of cavitation around the Twist11 foil, a 3D computational domain with the following configuration has been used. The inlet is located 3C upstream and the outlet 6C downstream of the hydrofoil, while the height and width of the domain each equal 2C, with C being the chord length of the foil. Taking advantage of the aforementioned symmetry of the hydrofoil, only half the domain is used for the following numerical simulations. The domain as it was used for the flow simulations is presented in Figure 5.4.

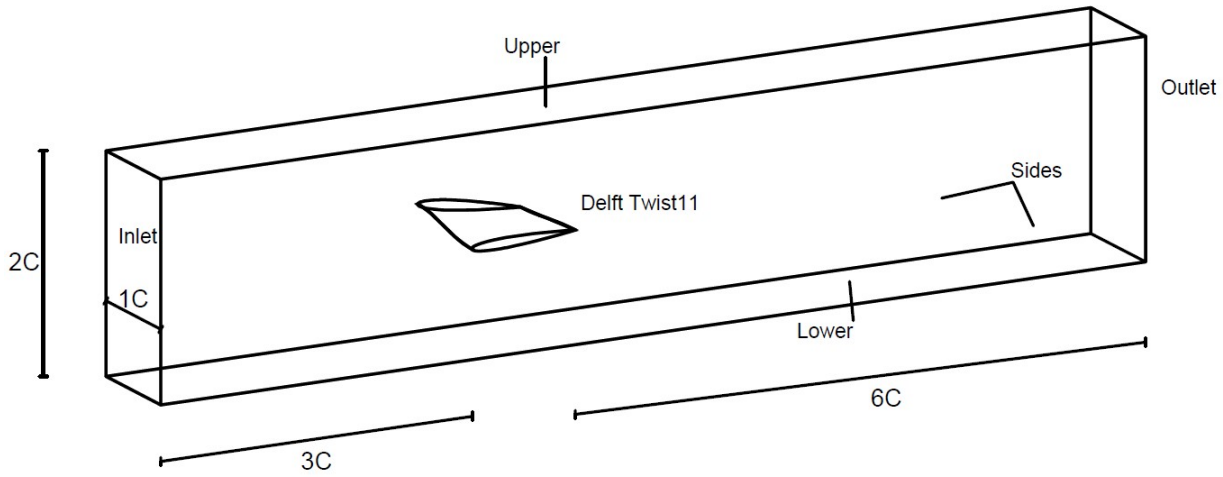

Figure 5.4: Delft Twist11 Hydrofoil Computational Domain

Regarding the flow and boundary conditions of this test case, the inlet velocity is set equal to 6.97 m/s, which leads to a Reynolds number of Re=$1.05 * 10^6$, the outlet pressure equal to 29000 Pa and the cavitation number has the value of $\sigma = 1.07$ [52]. The boundary conditions applied to the domain are presented in Table 5.1.

Boundary	Velocity	Pressure
Inlet	fixed value	zero gradient
Outlet	zero gradient	fixed value
Upper	slip	zero gradient
Lower	slip	zero gradient
Side walls	slip	zero gradient
Foil	no slip	zero gradient

Table 5.1: Boundary Conditions for Simulation of Cavitation around Twist11 Hydrofoil

5.5 Mesh and Timestep Independence Study

To evaluate cavitation around the Delft Twist11 hydrofoil, a suitable computational mesh had to be constructed. As it has been mentioned, cavitating behavior around this hydrofoil has a periodic character and the objective of this initial mesh study is to determine the spatial resolution needed to reproduce the phenomenon. The mesh independence study was executed in 2 steps. Firstly, an initial study was conducted to determine in which direction the grid should be refined to achieve the desired computational accuracy while minimizing the simulations cost. Secondly, the resolution of the grid showing the best characteristics from the initial process was further refined to get the optimal spatial configuration.

For all the following grids, the normal to the wall resolution y^+ has been kept equal to 1. Moreover, the streamwise resolution on the pressure side of the hydrofoil has remained constant and equal to 185 for all the grids.

Similar to the two-dimensional cases studied above, snapshots of the used mesh configuration are provided for purposes of clarity. Observing the images from above to below, the first snapshot shows the volume mesh refinement in the area around the hydrofoil both in the streamwise and the normal direction. The following two images provide a clearer view to the boundary layer, while also pointing out to the different chordwise discretisation employed for the suction side and the pressure side. Finally, the last snapshot shows the spanwise discretisation of the used mesh. The attached images concern Mesh 1-A.

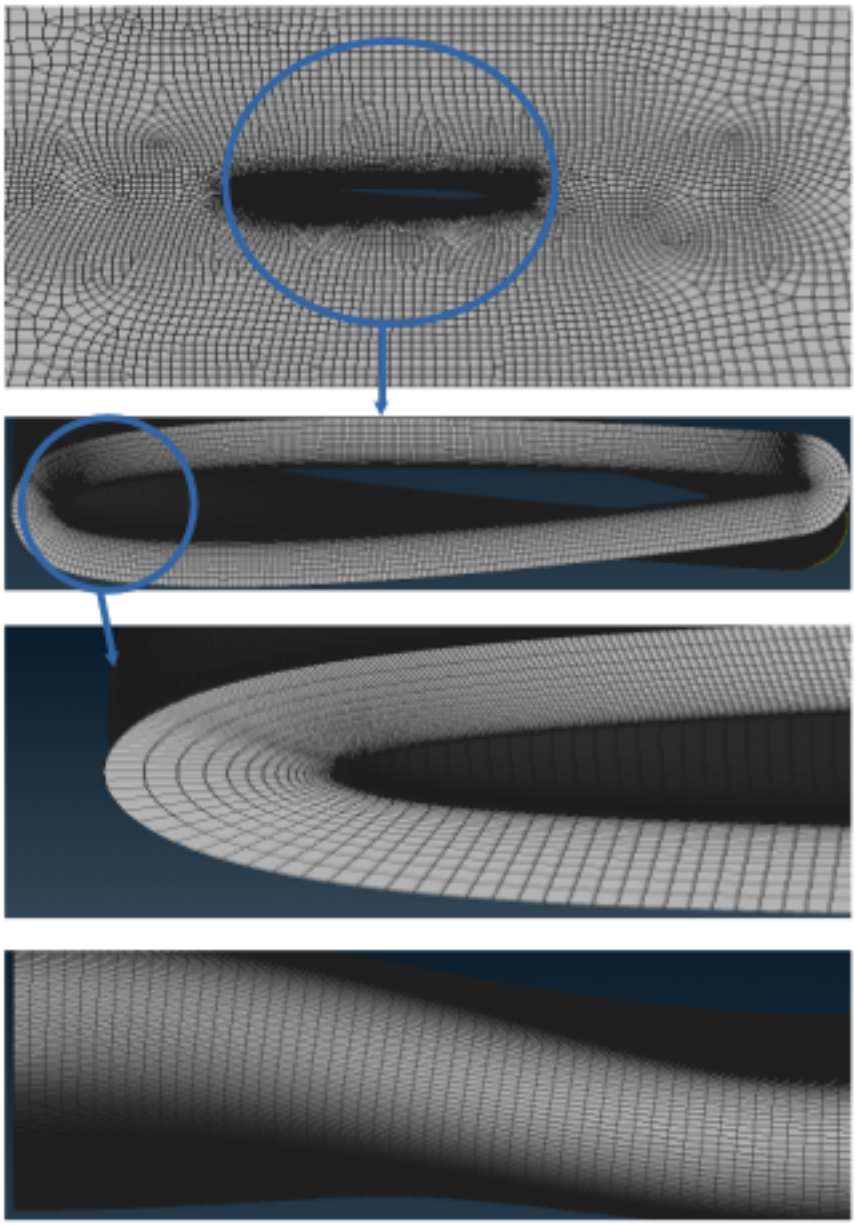

Figure 5.5: Delft Twist11 Hydrofoil Computational Mesh

The specifications of the examined mesh resolutions for the first part of the analysis can be seen in Table 5.2. In comparison to the original coarse grid (Mesh 1), Mesh 1-A is refined in the streamwise direction, Mesh 1-B in the spanwise direction and Mesh 1-C has a finer resolution in the normal to the foil direction. The numbers in the columns Streamwise, Spanwise, and Normal denote the number of elements, in which the surface was discretised in each direction. Higher element number denotes higher refinement.

Mesh	Streamwise	Spanwise	Normal	Structured (in mil.)	Total (in mil.)
1	185	50	35	0.655	2.55
1-A	375	50	35	0.987	3.005
1-B	185	75	35	0.982	4.500
1-C	185	50	70	1.310	3.064

Table 5.2: Initial Meshes for the Delft Twist11 Hydrofoil

In Figure 5.6 the refinement directions of the computational mesh are schematically presented so as to provide clarity regarding the grid configurations presented in this section.

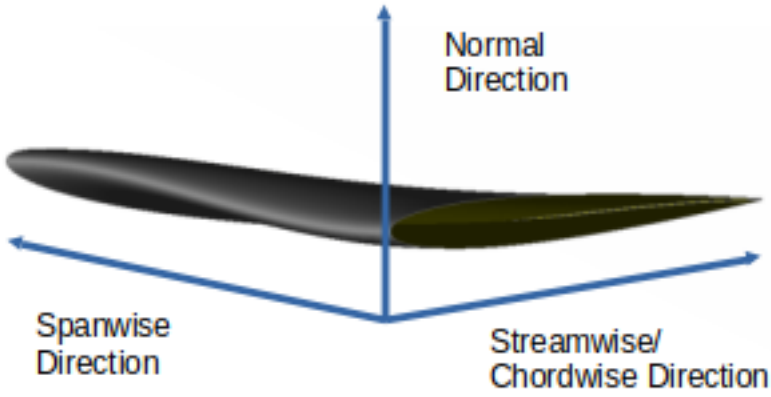

Figure 5.6: Delft Twist11 Hydrofoil Computational Domain

By testing the aforementioned grid resolutions, it was determined that the streamwise refinement (Mesh 1-A) offers the desired periodic behavior of the cavity around the hydrofoil. Thus, the grid that was chosen and examined for the mesh independence study was the mesh 1-A.

The specifications of the tested meshes are presented in Table 5.2. In comparison to the original streamwise-refined grid Mesh 1-A, Mesh 2-A is 2 times more refined in the normal to the wall direction while Mesh 3-A is finer in the streamwise direction.

Mesh	Streamwise	Spanwise	Layers	Structured (in mil.)	Total (in mil.)
1-A	375	50	35	0.987	3.005
2-A	375	50	70	1.999	3.915
3-A	515	50	35	1.335	6.324

Table 5.3: Meshes for the Delft Twist11 Hydrofoil Grid Independency Study

Regarding the meshes considered, all 3 of them displayed the sought periodic behavior, which was made evident by the distribution of the vapor mass over time. This graph is presented in Figure 5.7. It can be seen that the behavior of all 3 meshes displays a periodic character. However, Mesh 2-A predicts a different time period in the distribution of the vapor volume fraction that is almost double to the period predicted by Meshes 1-A and 3-A. As a result, the two meshes deemed suitable to carry out the numerical simulations with were Mesh 1-A and 3-A. And as the findings of the two show a great similarity to each other, Mesh 1-A was chosen due to the less computational power needed.

As far as the timestep analysis is concerned, the timesteps used corresponded to T/500,T/1000 and T/2000, with T being the experimental time period of the cavitation phenomenon and equaling 0.03 seconds. The present case was found to be particularly sensitive with respect to the temporal discretization. Larger timesteps than T/1000 did not reproduce a periodic behavior, while smaller ones also did not improve the obtained patterns. The timestep that better reproduces the sought periodic behavior is dt=T/1000. By using this timestep, the results of Figure 5.7 were obtained and the period was determined equal to 2.66 seconds.

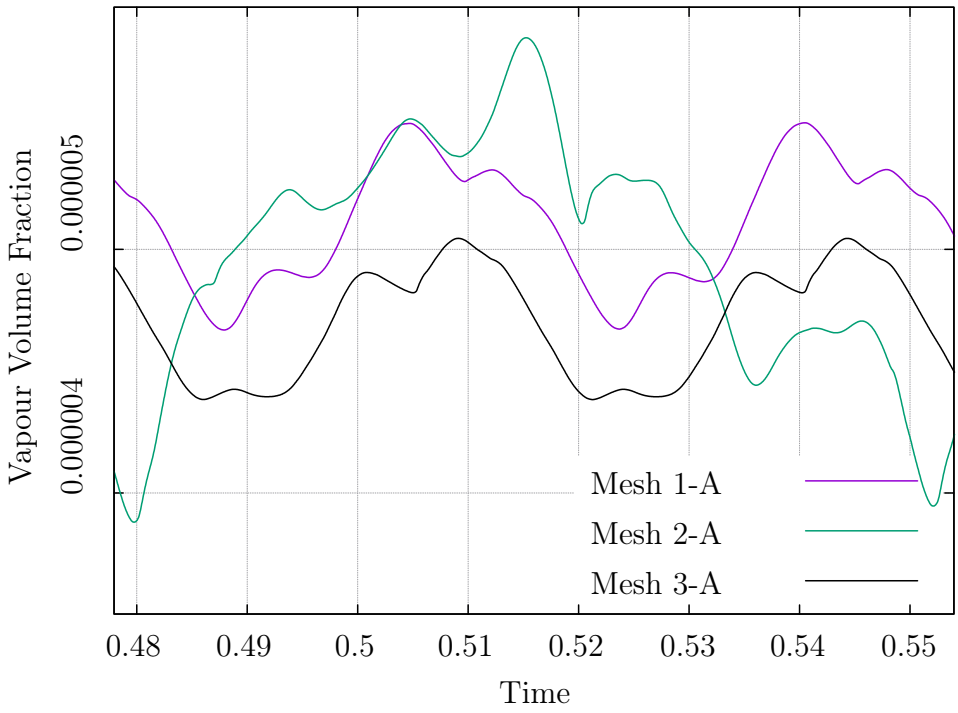

Figure 5.7: Vapor Volume Fraction over Time

5.6 Turbulence Model Modification

As it was already mentioned before, a modified $k-\omega$ SST turbulence model was incorporated in the analysis and the results were compared with the standard model. This modified turbulence model, commonly mentioned in the literature as Reboud's modification [40], attempts at reducing the turbulent viscosity that the standard RANS models overproduce at the area of the closure of the cavity and on the tail of the hydrofoil. In order to achieve better results regarding turbulence modeling, the following modification was introduced to equation 2.53.

$$\mu_t = \frac{f(\rho)\alpha_1 k}{max(\alpha_1\omega, SF_2)} \tag{5.1}$$

with the density correction function being described as follows

$$f(\rho) = \rho_v + \frac{(\rho - \rho_v)^n}{(\rho_l - \rho_v)^{n-1}}, n >> 1 \tag{5.2}$$

The value of n is set equal to 10 according to [38]. The aforementioned correction is considered an ad-hoc modification catering to the need for lower turbulent viscosity especially in the areas with lower density compared to the water areas, as it can be seen in Figure 5.8.

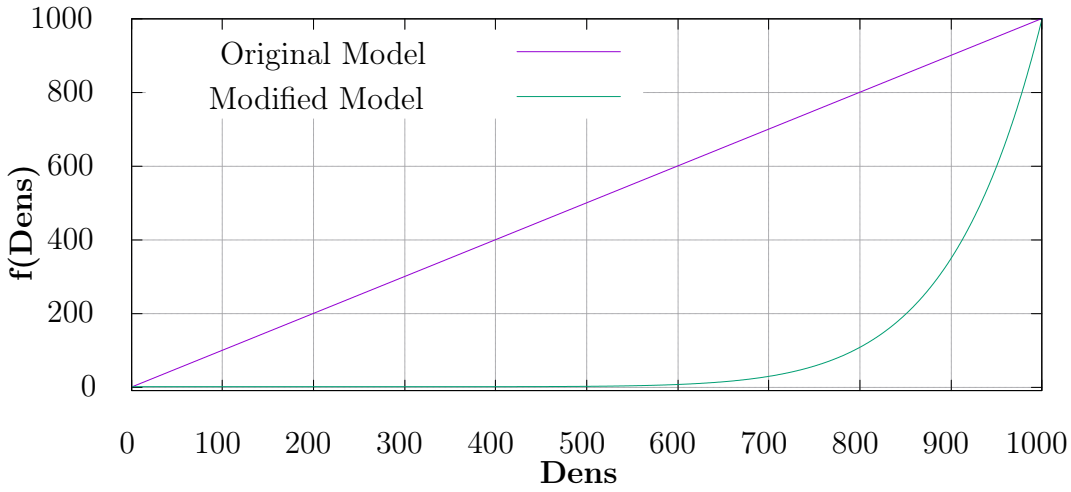

Figure 5.8: Viscosity Correction

5.7 Cavitation Pattern

Finally, the cavitation bubble was visualized and compared to the experimental data. Various snapshots of the hydrofoil have been taken where the vapor volume iso-surface $\alpha = 0.1$ is presented. In Figure 5.10 the first two columns contain the results produced by MaPFlow, while the third column displays the experimental results. The first from left column depicts the results obtained when using the RANS model and for the results of the second column the RANS model with the Reboud correction was applied. The hydrofoil is denoted in light gray color and the vapor volume in blue. All the snapshots are zoomed in on the vapor area around the center of the hydrofoil. The edges, as it was already mentioned, have not been filled with vapor, which is a basic property of the twisted hydrofoils. A snapshot of the cavitating pattern in isometric view is presented in Figure 5.9 to show the cavitating behavior for the entirety of the geometry.

Through the snapshots in Figure 5.10 it is made clear that MaPFlow can reproduce the aforementioned mechanism of unsteady cavitation. The stages of the phenomenon can be traced back to Figure 5.2. The bubble is at full growth in Figure 5.10a. In Figures 5.10b

- 5.10d the re-entrant and side-entrant jets shed the cavitation bubble in its middle part. In Figures 5.10d - 5.10f, the shedded vapor completely splits from the original cavity and follows the flow downstream. In the final stage of the phenomenon, corresponding to Figures 5.10g - 5.10j the separated bubble moves further downstream and the original vapor cavity regenerates, ready for the shedding cycle to begin once again.

The implemented Reboud modification produces more accurate results as far as the quantity of vapor generated. However, there is still a visible vapor underproduction in comparison to the experimental results with both methods. Due to the reduced values of viscosity in the modified $k - \omega$ -SST turbulence model, the shedding process and the unsteady vapor structures are depicted in greater detail.

All in all, MaPFlow is deemed to be successful in predicting the unsteady cavitation behavior, as the stages of shedding and regenerating the vapor bubble are clearly reproduced. Due to the fact that RANS is not able to grasp the unsteady dynamics of the present case, quantitative results do not offer any useful conclusions. In the following snapshots, the qualitative capture of the periodic shedding mechanism is observed.

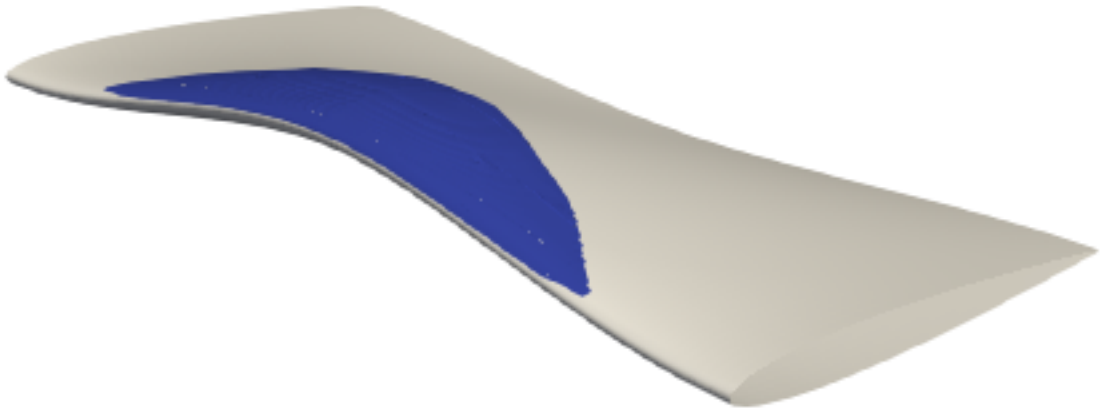

Figure 5.9: Isometric View of the Delft Twist11 Hydrofoil,vapor iso-surface $\alpha = 0.1$

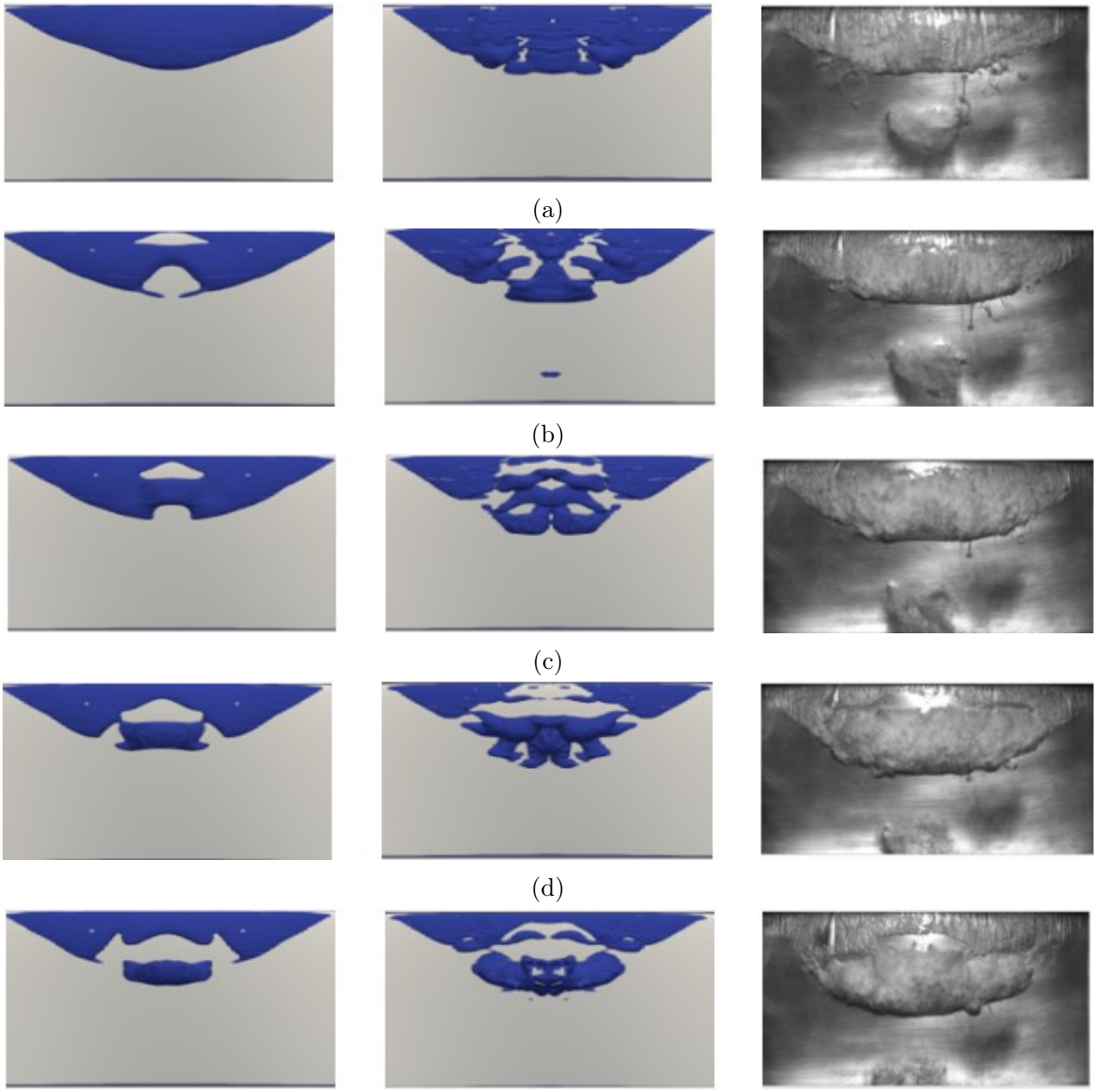

Figure 5.10: Comparison between numerical results (First column: RANS, Second column: RANS with Reboud Correction) and experimental results(third column) - dt=T/10, vapor iso-surface $\alpha = 0.1$

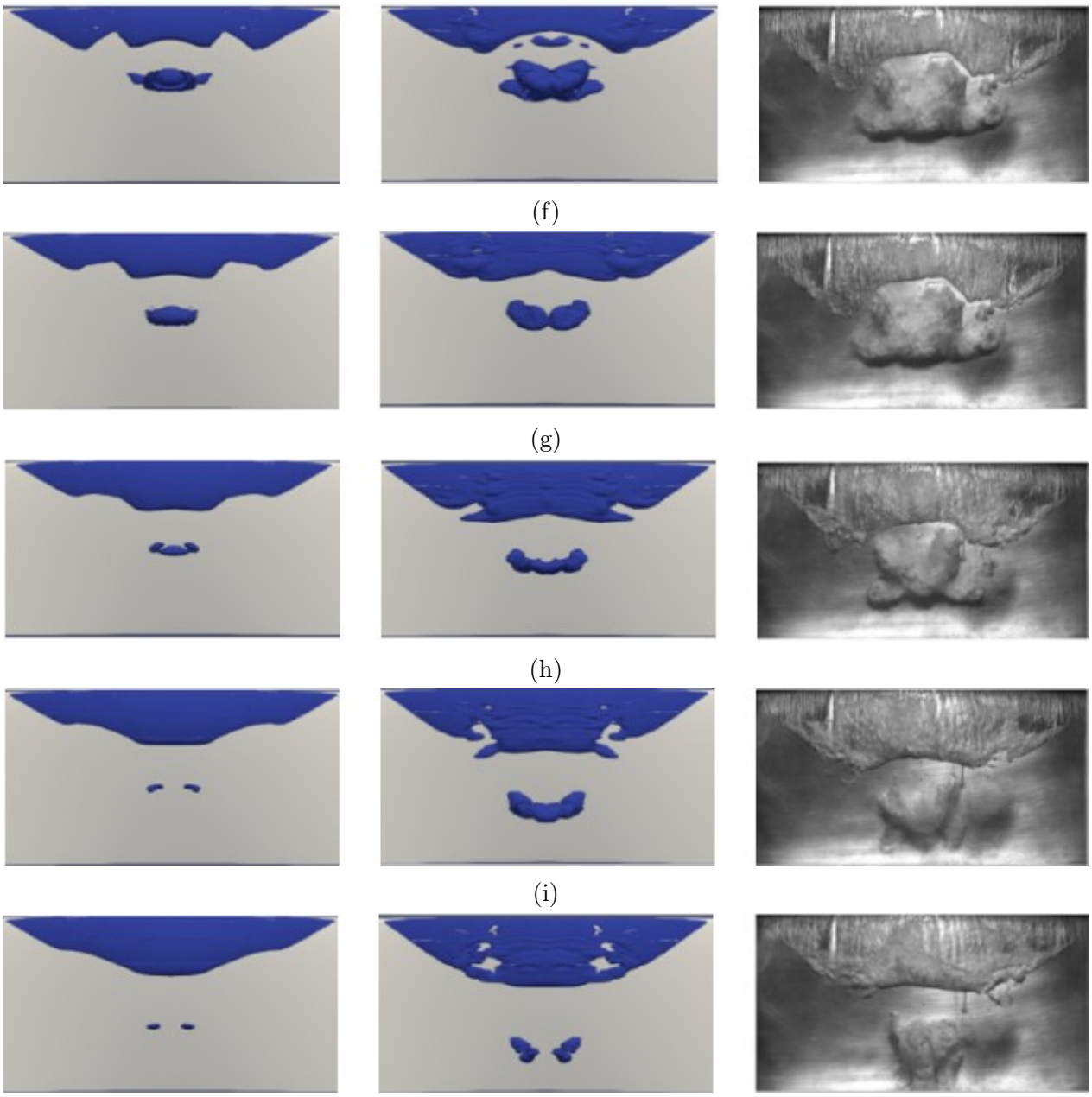

Figure 5.10: Comparison between numerical results (First column: RANS, Second column: RANS with Reboud Correction) and experimental results(third column) - dt=T/10, vapor iso-surface $\alpha = 0.1$,part two

6 Marine Propeller

Cavitating propeller performance is a particularly challenging phenomenon to investigate. So far, the most widely used tool for this scope have proven to be model scale experimental tests, like the ones carried out by SVA Potsdam regarding the controllable pitch VP1304 propeller, also referred to as Potsdam Propeller Test Case.

6.1 PPTC propeller

In this chapter, the Potsdam Propeller Test Case (PPTC) is used to evaluate the capability of MaPFlow to accurately predict cavitating flow around marine propellers. Simulations of cavitating and non-cavitating flow were conducted around this model scale propeller, which was used as a reference geometry in the 1st International Workshop on Cavitating Propeller Performance [53].

The considered geometry is a model scale five-bladed propeller with a diameter of $D = 250mm$. On the webpage of the workshop, analytical geometrical description of the propeller along with the propeller data sheet and description by radius are given along with the experimental results. In Figure 6.1, a sketch of the PPTC geometry from a fore and an isometric view is presented.

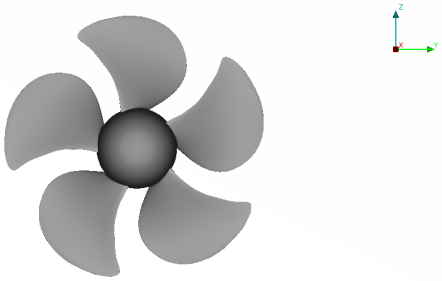

(a) Fore View

Figure 6.1: PPTC Propeller Geometry

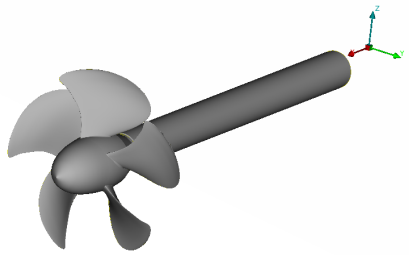

(b) 3D View

Figure 6.1: PPTC Propeller Geometry

6.2 Propeller Open Water Characteristics

During open water tests, the thrust and torque produced by the propeller are described by using three non-dimensional characteristics. These are the thrust coefficient K_T, the torque coefficient K_Q and the advance coefficient J, all three of which are described in the following equations.

$$K_T = \frac{T}{\rho n^2 D^4} \tag{6.1}$$

$$K_Q = \frac{Q}{\rho n^2 D^5} \tag{6.2}$$

$$J = \frac{V_s}{nD} \tag{6.3}$$

In the equations above, T denotes the thrust, Q the torque, ρ the water density, n the propeller rotational speed, D the propeller diameter and V_s the advance speed.

6.3 Computational Domain Setup

One very important parameter in the setup for marine propeller simulations is the size of the computational domain. As the rotating frame of reference frame is used in the present study, a cylindrical domain has been chosen. As far as the cylinder's dimensions are concerned, they

are chosen in such a way so that uniform inflow upstream of the propeller and the avoidance of reflection downstream of the propeller are ensured. The inlet is located 20D upstream of the propeller hub, the outlet 25D downstream of the shaft and the outer boundary 20D away from the x axis, where by D is denoted the propeller diameter.

Furthermore, as in the current work the propeller is operating in uniform inflow, rotational periodic boundary conditions have been applied. This type of boundary condition is used when the geometry in consideration and the expected pattern of the flow solution demonstrate a periodically repeating behavior, as in the case of a marine propeller. This type of boundary condition offers closure to the problem by transferring the flow variables from one periodic surface to another.

So, the domain is constituted of a blade passage with 72° periodicity in the circumferential direction. The domain is graphically presented in Figure 6.2 and the boundary conditions of the domain are highlighted in Table 6.1. The left and right sides of the domain, which are not mentioned in the aforementioned table, are considered rotational periodic boundaries. Finally, the normal to the wall direction was held equal to y+=1 for the entirety of the numerical analysis. To simulate the propeller rotational motion, the rotating frame of reference approach has been used, as it was introduced in Chapter 2.

Boundary	Velocity	Pressure
Inlet	fixed value	zero gradient
Outlet	zero gradient	fixed
Outer Domain	slip	zero gradient
Hub	no slip	zero gradient
Shaft	slip	zero gradient
Blade	no slip	zero gradient

Table 6.1: Boundary Conditions for Simulation of Cavitation around the PPTC Propeller

The open water performance of the propeller in wetted and cavitating flows is assessed for three different operating conditions, which are presented in Table 6.2. The value of the thrust coefficient listed in table 6.2 refers to the non-cavitating flow.

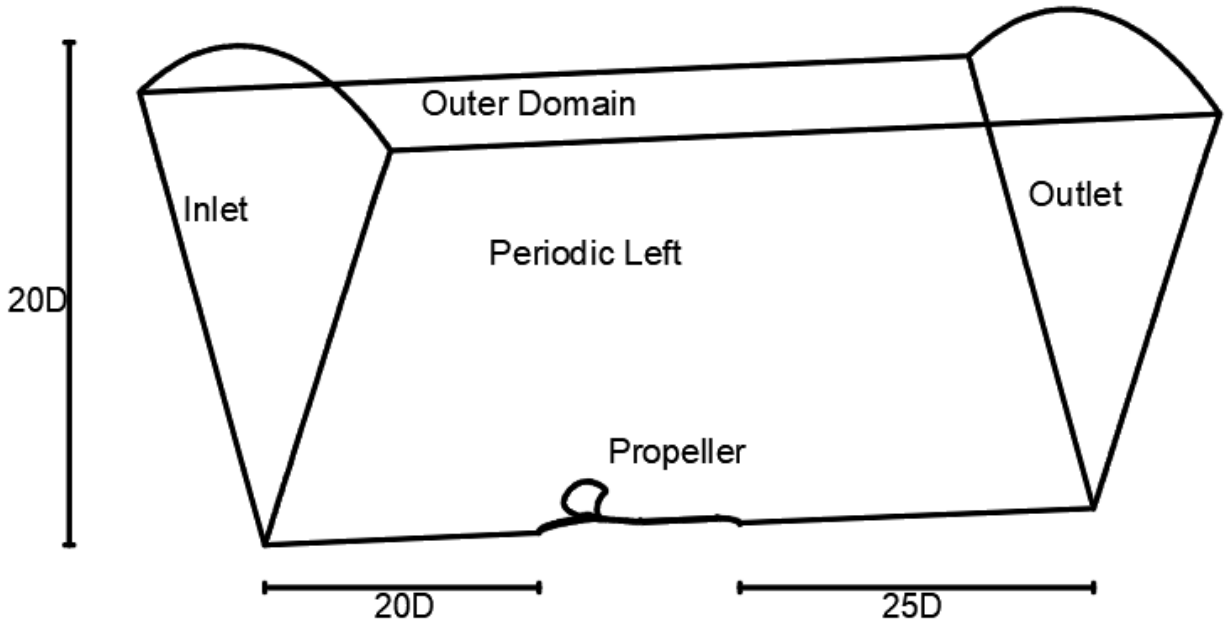

Figure 6.2: PPTC Computational Domain

Case	J	σ_n	V_{inlet} (m/s)	n (rev/s)	K_T
2.1	1.019	2.024	6.365	24.987	0.387
2.2	1.269	1.424	7.927	24.986	0.245
2.3	1.408	2.000	8.805	25.014	0.167

Table 6.2: Operating Conditions of Cavitation Experiments

6.4 Mesh and Timestep Independence Study

Similar to the previous cases, an analysis regarding grid and timestep had to be carried out so that the results can be deemed as accurate. Both studies were executed for Case 2.1 in both non-cavitating and cavitating flow conditions.

Firstly, some information regarding the configuration of the computational domain is presented. Figures 6.3 and 6.4 provide insight on how the computational meshes employed for this case were constructed. As it can be seen in figure 6.3 the grid has been refined parallel to the flow direction so as to better model the propeller wake and its hydrodynamic characteristics. Moreover, an even finer refinement has been imposed around the propeller

blade, since this is the expected area of cavitation occurrence. A dense grid configuration is required in order to capture the cavitation phenomenon. Another aspect of the meshing technique highlighted in the same image is the way the structured boundary layer has been constructed, so that the condition of $y^+ = 1$ is satisfied.

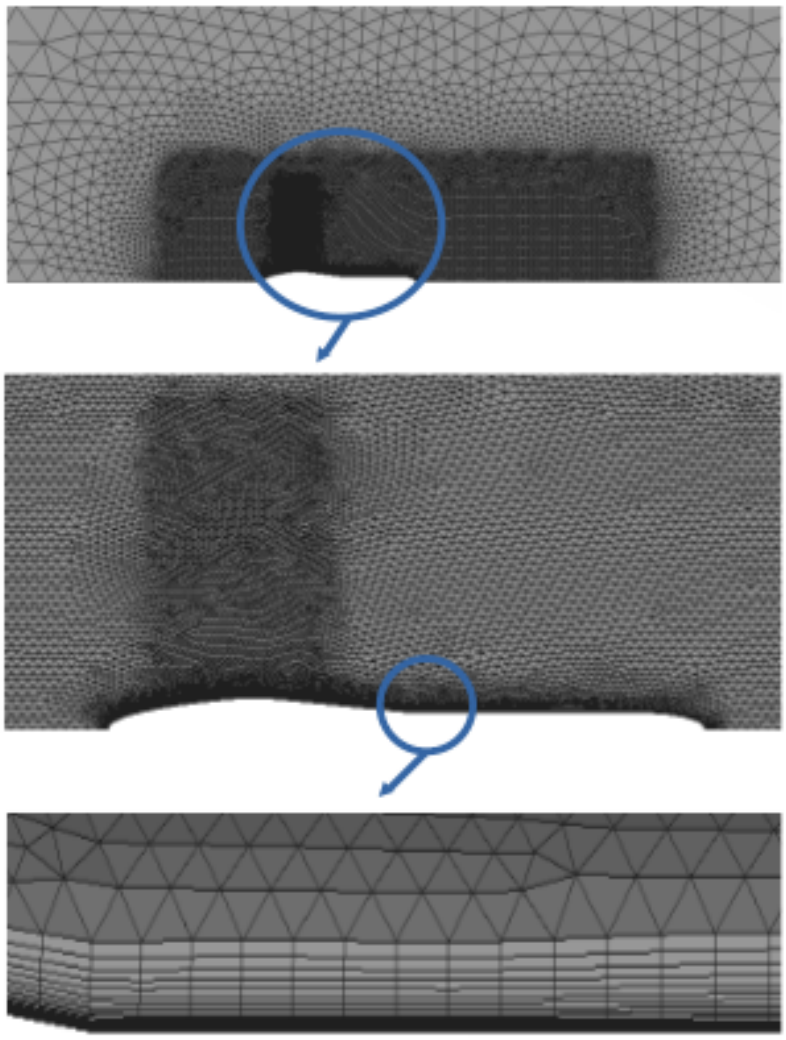

Figure 6.3: PPTC Computational mesh refinement

Figure 6.4 reveals one of the most significant steps in the mesh creation, namely the propeller blade surface mesh. The propeller blade has a very complex geometry and a very high

refinement is needed for the cavitation prediction. In order to tackle these issues, a structured grid was created, as it is seen below, in which the areas of the leading and trailing edge, the blade tip and the root have been further refined. The blade boundary layer has been constructed identically to the one of the shaft, which is seen above, by creating layers in the normal to the blade surface direction.

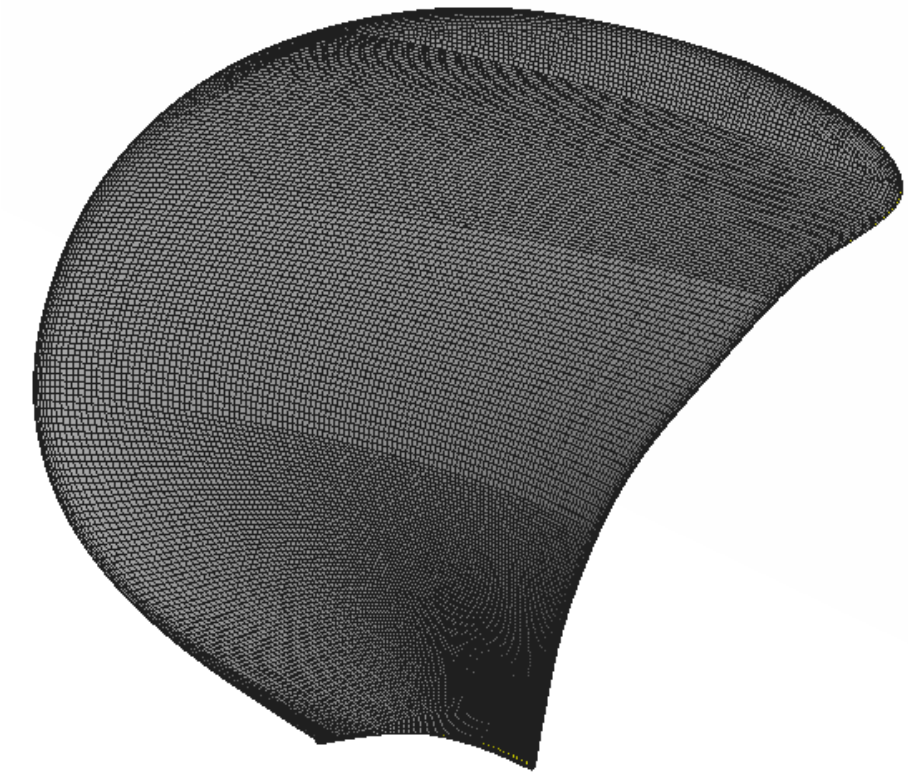

Figure 6.4: Surface mesh on the propeller blade

Beginning with the mesh independency, three different meshes were tested, with all three having a boundary layer that satisfies the requirement of $y^+ = 1$. The specifications of these meshes, which are labeled as Medium, Fine-A and Fine-B, are presented in Table 6.3. In comparison to the Medium Grid, Mesh Fine-A is more refined volume-wise in the wake region of the propeller. On the contrary, Mesh Fine-B has a more refined surface mesh of the geometry and boundary layer around it.

Mesh	Surface	Boundary Layer (in mil.)	Total Elements (in mil.)
Medium	69000	1.662	4.100
Fine-A	69000	1.662	8.170
Fine-B	100000	2.408	6.772

Table 6.3: Mesh Specifications for PPTC propeller

For these grid configurations the thrust coefficient for non-cavitating and cavitating flow and the torque coefficient for cavitating flow were calculated and compared with each other. The results of this analysis are displayed in Table 6.4.

Mesh	K_T (non-cav.)	K_T (cav.)	$10K_Q$ (cav.)
Medium	0.376	0.377	0.9564
Fine-A	0.376	0.377	0.9584
Fine-B	0.375	0.376	0.9543

Table 6.4: Mesh Specifications for PPTC propeller

It is observed that all 3 meshes produce similar thrust and torque coefficients. As a result, the grid chosen to carry out the numerical simulations was the Medium grid due to lower computational cost.

The same procedure was carried out to specify the timestep of the simulations. The 3 values examined are the following: $dt = T/2600$, $dt = T/1800$ and $dt = T/1000$. This analysis was done considering only cavitating flow, as the non-cavitating flow was modeled steadily in time. The results of this analysis are gathered in Table 6.5. Since all the timesteps produced identical results for the thrust coefficient and very similar ones for the torque coefficient, they were all deemed suitable for the simulations. Finally, the timestem chosen was $dt = T/1800$.

Timestep	k_T	$10k_Q$
T/2600	0.377	0.9582
T/1800	0.377	0.9574
T/1000	0.377	0.9562

Table 6.5: Timestep analysis for PPTC propeller

6.5 Numerical results

In this part of the study, the results of the simulations around the PPTC propeller are presented and assessed. For each of the 3 different operating conditions modeled the thrust and torque coefficients as well as the obtained cavitation pattern are compared with the experimental results reported in [53].

In Table 6.6, the thrust coefficient for cavitating and non-cavitating conditions as well as the torque coefficient for the cavitating conditions are shown along with the respective experimental values for all 3 sets of operating conditions (Table 6.2). Along with these values, the relative error for each value expressed in percent is calculated and assessed.

		K_T (non cav.)	K_T (cav.)	$10K_Q$ (cav.)
Case 2.3.1	MaPFlow	0.376	0.3774	0.9544
	Experiment	0.387	0.3735	0.9698
	Relative Error (%)	-2.76	1.06	-1.59
Case 2.3.2	MaPFlow	0.231	0.1866	0.5909
	Experiment	0.245	0.2064	0.6312
	Relative Error (%)	-5.63	-9.6	-6.32
Case 2.3.3	MaPFlow	0.1505	0.1268	0.4664
	Experiment	0.167	0.1362	0.489
	Relative Error (%)	-9.89	-6.88	-4.62

Table 6.6: Comparison of Thrust and Torque Coefficient with experimental values

Beginning from the non-cavitating flow, in Case 2.3.1 the thrust is underpredicted by a relatively small margin and can thus be considered a satisfactory prediction. However, as it is seen for Cases 2.3.2 and 2.3.3, the error in the thrust coefficient prediction grows with larger values of the advance coefficient. This finding has also been documented in past studies carried out with MaPFlow [54] and it can be attributed to the following. According to [3], larger values of J lead to smaller angles of attack while examining propellers with constant pitch, as is the case in the present study.

As far as the cavitating flow is concerned, it can be seen that MaPFlow can very accurately predict the thrust and torque coefficients in Case 2.3.1, where the prediction accuracy is in fact better than the wetted flow. The same improvement in prediction accuracy from the non-cavitating to the cavitating flow can also be found in Case 2.3.3. However, in Case 2.3.2 we come across an opposite pattern, in which the cavitating case shows higher relative error than the non-cavitating one. This can be attributed to the reduction of the cavitation number in this case. The value of $\sigma = 1.424$ produces more intense cavitation phenomena in comparison to the values of $\sigma = 2.024$ and $\sigma = 2$ in Cases 2.3.1 and 2.3.3 respectively. This makes the cavitation phenomenon harder to accurately predict. All in all, from these findings it can be concluded that the ability to predict the open water coefficients in cavitating flow is dependent on two parameters: the advance coefficient J and the cavitation number σ. Larger values of J and smaller values of σ cause a regression on the simulation accuracy.

Finally, as it has been mentioned in the introductory chapter, one of the effects of cavitation is the reduction of the propeller efficiency, the so-called thrust breakdown. However, the numerical results for Case 2.3.1 do not exhibit this kind of behavior. This is pointed to the underprediction of the non-cavitating thrust and not to the inability of MaPFlow to predict the cavitating efficiency of the propeller. For the present set of operating conditions, the experiments noted a 3.49% breakdown in the thrust coefficient for cavitating flow in comparison to wetted flow. This drop-off is quite small and this, in combination with the underprediction of the non-cavitating thrust, leads to a non-reduced propeller efficiency, although such a pattern was expected. In the Cases 2.3.2 and 2.3.3, where the thrust breakdown due to cavitation is more intense, it can clearly be seen that MaPFlow successfully grasps the dynamics of the thrust breakdown due to cavitation. The numerically predicted and experimental values of the aforementioned breakdown are presented in Table 6.7.

		Thrust Breakdown (%)
Case 2.3.1	MaPFlow	0.29
	Experiment	-3.49
Case 2.3.2	MaPFlow	-19.3
	Experiment	-15.76
Case 2.3.3	MaPFlow	-17.84
	Experiment	-18.44

Table 6.7: Thrust breakdown due to cavitation occurrence

6.5.1 Case 2.3.1

In this section the cavitation results for Case 2.3.1 are presented and compared with the available experimental data. In Figures 6.5a and 6.5b the experimental and numerical results regarding the cavitation bubble on a single propeller blade are presented, while in Figure 6.6 the vapor volume on the suction and on the pressure side of the propeller are visualized. In all the figures presented in this section, with blue color is depicted the vapor volume fraction $\alpha = 0.5$, as it was proposed by the organizers of the experiments. The values used in the aforementioned workshop regarding the vapor volume fraction were $\alpha = 0.2$ and $\alpha = 0.5$. In the present work, both were assessed for both cases without any notable differences observed between the two. For all three studied cases, the proposed value was used for the visualization of the cavitation pattern.

Assessing the vapor volume produced by the numerical simulations, the first observation is that MaPFlow successfully reproduces the cavitation bubble at the root as well as at the tip of the blade and at the tip vortex. However, the one spotted discrepancy between the experimental and the computational results includes the presence of vapor at the blade leading edge in the numerical findings, which also coincides with the results of the majority of the participants of the workshop [52].

Firstly, regarding the prediction of cavitation in the leading edge region, the pressure at the leading edge of the propeller blade is predicted to be lower than the saturation pressure of water. As a result, the computational model produces vapor in that area, since pressure is the only factor impacting the occurrence of cavitation in the model. On the other hand, in the experiment the vapor formation depends on other factors too, such as nuclei content and

nuclei residence time in the low pressure area. [44]. Another possible cause of this discrepancy could be the presence of a laminar boundary layer around the model scale propeller. This would hinder the inception of cavitation in that area regardless of the low pressure. In order to fully understand and assess this numerical disparity, experimental data about the actual pressure values of the blade have to be provided. Without this pressure data it is very difficult to determine if the leading edge cavitation produced by the code is caused by an error in the modeling of the flow, differences between the geometrical modeling and the propeller or by some of the conditions listed above. Another aspect determining the existence and extent of the leading edge sheet cavitation seems to be the choice of cavitation model according to the findings of [55] and [11]. The Kunz cavitation model, which is used in the present study, is found to predict larger cavitation patterns.

Secondly, as far as the tip vortex cavitation is concerned, a very high refinement of the mesh in that area is needed in order to capture the vortex physics and accurately preserve them while moving downstream with the flow. The mesh was further refined in the tip vortex area to assess the predictability of the tip vortex cavitation, in a similar way that the local refinement was achieved in [56] and [57]. MaPFlow successfully predicts this behavior although the computational cost needed to achieve this rises significantly.

Another important observation that can be made from the placement of the vapor fraction in Figure 6.5b regards the thrust breakdown which was analyzed in the previous section. In this particular set of operating conditions, the cavitation occurs at the blade tip and the root at the suction side. Both of these areas do not have an important contribution on the thrust production of the propeller. Thus, the low value of thrust breakdown in the experiments is to be expected and it also justifies the absence of the phenomenon in the numerical simulations, also taking the computational error into consideration.

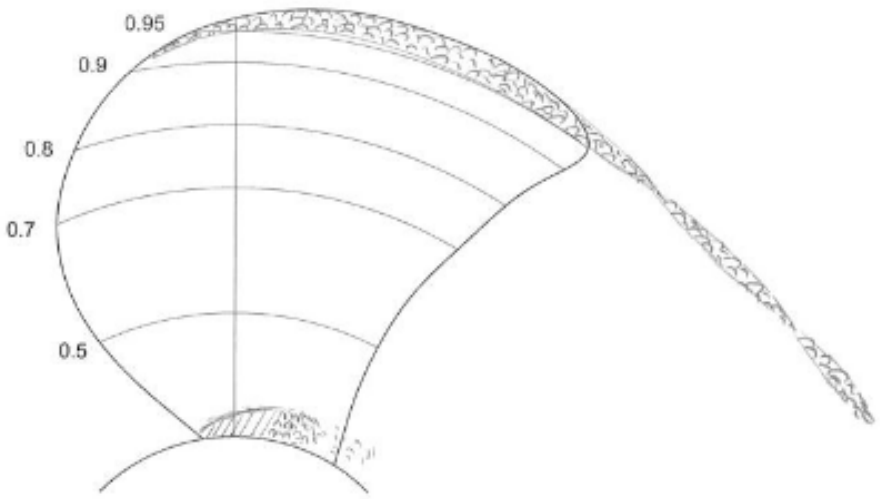

(a) Experiment

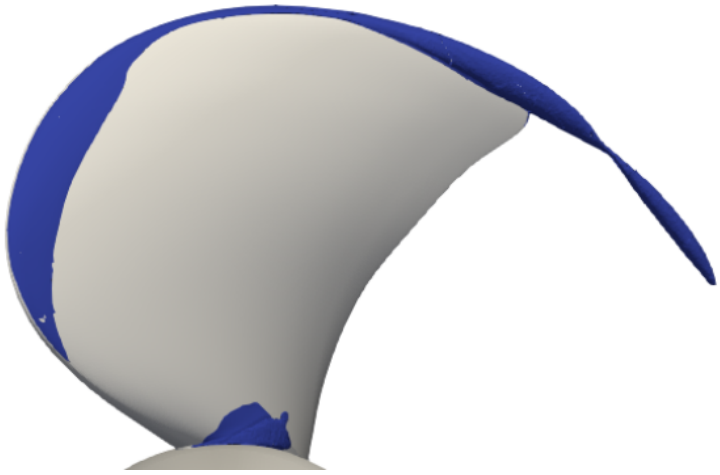

(b) MaPFlow

Figure 6.5: Vapor Volume Fraction, Case 2.3.1

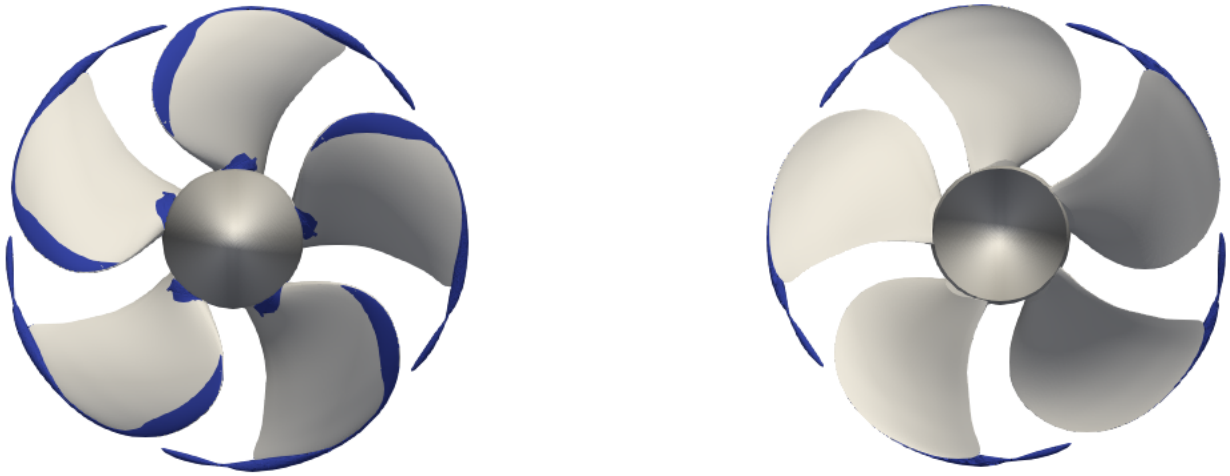

(a) Suction Side (b) Pressure Side

Figure 6.6: 3D View of the cavitating propeller, Case 2.3.1

6.5.2 Case 2.3.2

Similar to the previous case, the cavitation results for Case 2.3.2 are presented in this section. The only difference is that the vapor volume fraction proposed and presented is $\alpha = 0.5$.

Comparing Figures 6.7a and 6.7b it is evident that MaPFlow can accurately predict the reported root cavitation as well as a part of the tip vortex cavitation observed in the experiments. As to the tip vortex cavitation, the reason for this discrepancy in the numerical prediction is the grid refinement. This case requires further refinement than the first test case in order to accurately predict the tip vortex cavitation. This is something that can be attributed to the difference in intensity of tip vortex cavitation between the two test cases.

Another significant difference between the computational and the experimental results is the occurrence of bubble cavitation in the latter ones. The pressure in the area of bubble cavitation is close or even below the vapor pressure, which is also confirmed by the numerical results. However, for pressure values slightly larger than the saturation pressure the employed modeling cannot reproduce cavitation occurrence. So, a part of the bubble cavitation around r/R=0.5 is predicted as sheet cavitation, while the rest is not predicted at all, as in those zones the vapor bubbles stick to areas of slightly larger pressure.

Finally, cavitation occurs also in the face of the suction side and the root of the pressure side, as seen in Figure 6.10. This explains the high level of thrust breakdown predicted.

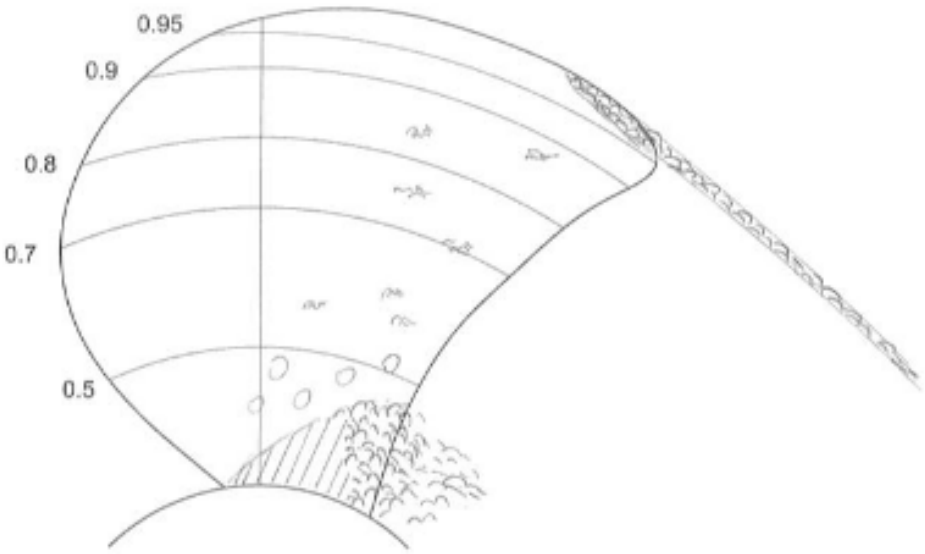

(a) Experiment

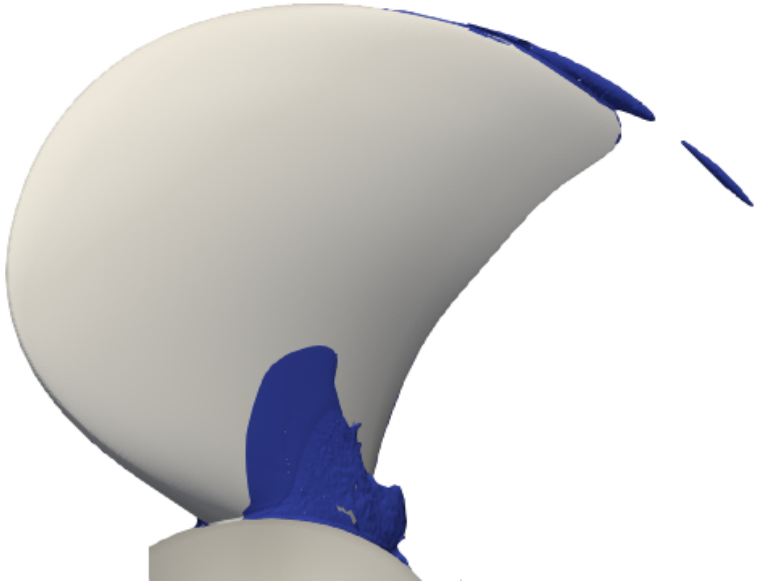

(b) MaPFlow

Figure 6.7: Vapor Volume Fraction, Case 2.3.2

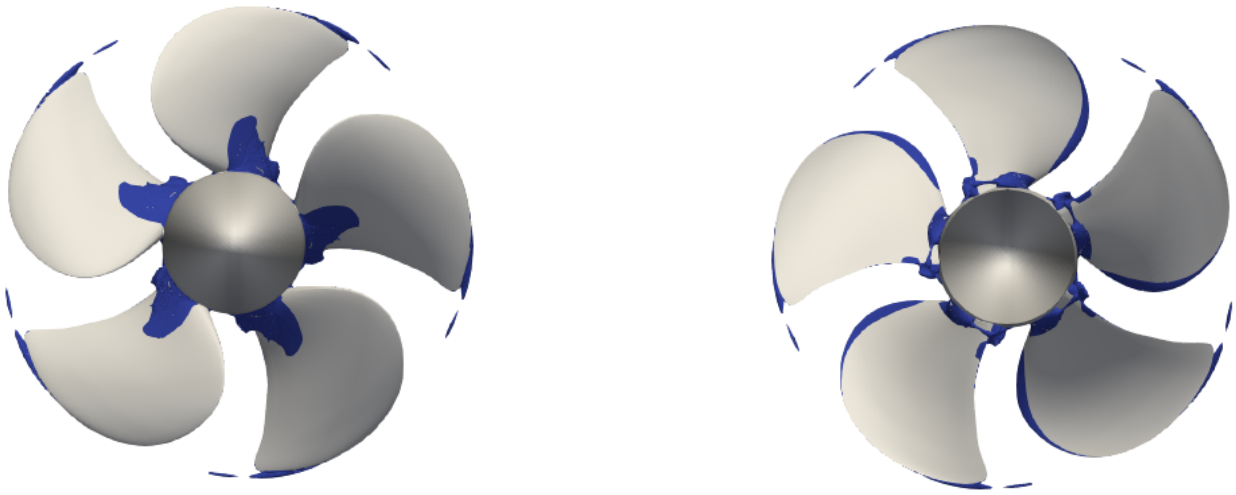

(a) Suction Side (b) Pressure Side

Figure 6.8: 3D View of the cavitating propeller, Case 2.3.2

6.5.3 Case 2.3.3

Identically to Case 2.3.2, for the present case the numerical results for vapor volume fraction $\alpha = 0.2$ were compared to the available experimental data.

This time, the observed cavitation patterns are located on the pressure side of the blade. MaPFlow successfully predicts the root and leading edge cavitation. However, unlike the previous cases, the tip vortex cavitation is not reproduced.It is to be noted that the tip vortex cavitation in this case was not predicted by any of the participants of the workshop. Finally, one discrepancy regarding the bubble cavitation at the root can be observed, with the causes of this discrepancy having been explained.

Furthermore, as cavitation occurs on the pressure side, the thrust breakdown is again predicted at a high rate.

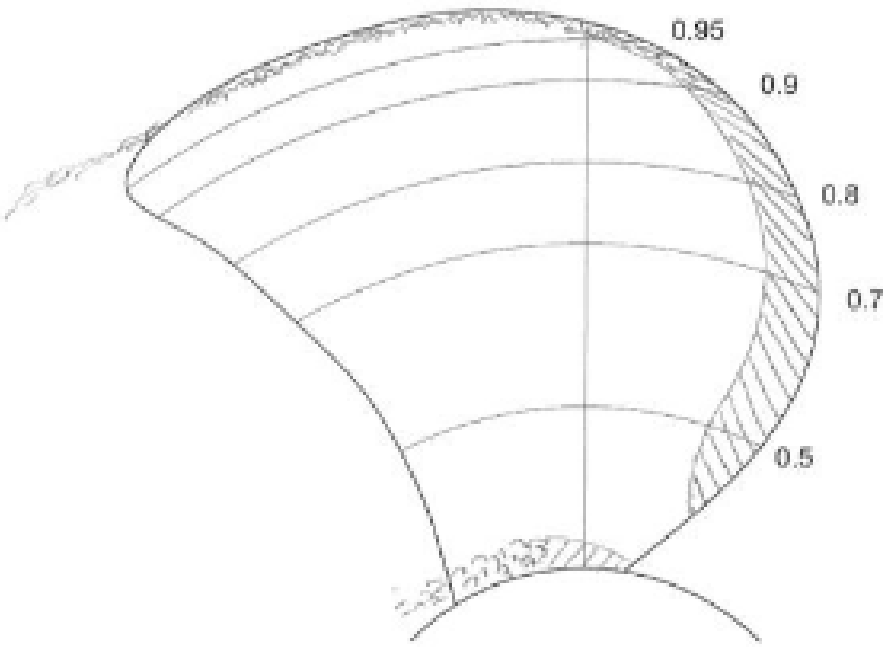

(a) Experiment

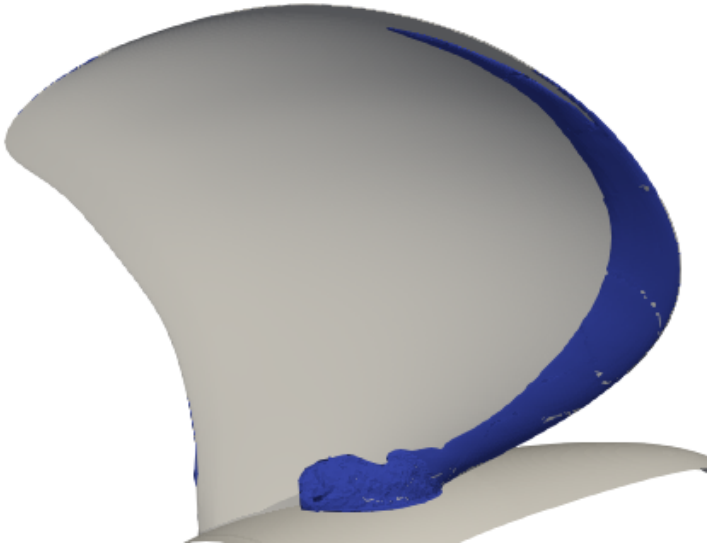

(b) MaPFlow

Figure 6.9: Vapor Volume Fraction, Case 2.3.3

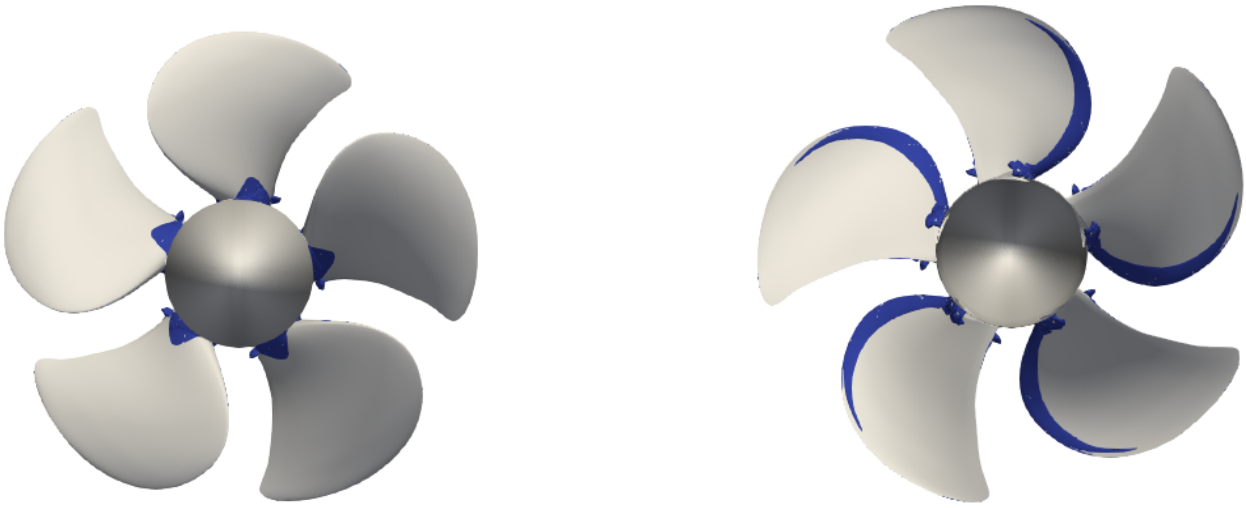

(a) Suction Side (b) Pressure Side

Figure 6.10: 3D View of the cavitating propeller, Case 2.3.3

7 Conclusions and further research recommendations

The intention of the present thesis was the development of an algorithm that can properly model the cavitation phenomenon in various marine applications using an Eulerian RANS solver. Under this scope, the Kunz transport equation model for mass transfer was employed and validated in three different test cases of increasing geometrical complexity. Firstly, a pair of two-dimensional hydrofoils was used, followed by a twisted three-dimensional hydrofoil and a model-scale marine propeller.

Beginning from the two-dimensional hydrofoils, the empirical coefficients included in the Kunz cavitation model were calibrated so as to obtain accurate numerical results. The tuned set of empirical factors was validated on two different two-dimensional hydrofoils for various values of the cavitation number. The agreement between the findings of MaPFlow and the experimental data was very good, particularly in the cases with higher values of the cavitation number. Lower values of σ posed a more difficult challenge for the code and the prediction accuracy deteriorated, however it has to be noted that the agreement remained in satisfactory levels.

The implemented method was then validated on a three-dimensional twisted hydrofoil. Experiments conducted on this geometry had previously shown the periodic character of the cavitation phenomenon around this hydrofoil. The RANS turbulence modeling approach has been found to fail in the prediction of the unsteady cavitation dynamics. In order to overcome this innate issue of the RANS equations, the Reboud modification was also implemented to the turbulence model. The numerical findings of both approaches were compared to the experimental results regarding the mechanism of cavitation shedding and regenerating. The Reboud modification produces more accurate cavitation patterns than the RANS approach and both imitate the basic stages of the mechanism. However, vapor underproduction is notable, as has been with all the RANS-based models validated on this case.

The analysis carried out regarding the cavitating flow around a model-scale marine propeller was twofold. The initial part focused on the hydrodynamic characteristics of the propeller and the second part on the cavitation pattern observed around it for three different values of the advance coefficient.

MaPFlow demonstrated particularly good agreement for the thrust and torque coefficient in cavitating and non-cavitating flow for lower values of the advance coefficient. The relative error grew for higher values of J. The results for the cavitating condition were also heavily dependent on the value of the cavitation number. Identical to the findings about the two-dimensional hydrofoils, lower values of σ led to deterioration of MaPFlow's accuracy. Thus, the accurate numerical prediction of a propeller's open-water characteristics in cavitating flow is a function of both the advance coefficient J and the cavitation number σ. The code also shows capability to correctly model the anticipated thrust breakdown due to the occurrence of cavitation in the 2 cases where this phenomenon is significant.

An integral part of the cavitation prediction around marine propellers is the position of the observed cavitation pattern on the blade. The inception of the cavitation phenomenon in different regions of the propeller blade is associated with different types of cavitation that have to be taken separately into account during the propeller design and testing process. MaPFlow predicts the regions of root and tip cavitation with a very high accuracy, while the main discrepancy to be found regards the bubble cavitation on the suction side. As far as the tip vortex cavitation is concerned, MaPFlow can very accurately reproduce it when the phenomenon is intense. Nevertheless, it has to be noted that in order to capture this cavitation type, a very high grid refinement is required. Moreover, there is an overprediction of vapor in the leading edge region of the blade, which requires further clarification in the available experimental data in order to be interpreted.

Finally, some conclusions regarding the entirety of the numerical analysis are presented. Looking back on the numerical simulations in retrospect, the results produced by MaPFlow regarding cavitation in marine applications are very promising, as the capability to predict the effects of cavitating flow and the cavitation patterns for a plethora of inflows and geometries was clearly demonstrated. One very important finding concerned the empirical coefficients of the employed cavitation model. It was observed that following their calibration around two-

dimensional geometries, the chosen set of factors could produce accurate results for different applications. This is particularly useful, since it enables to carry out the essential cavitation model tuning process for simple geometries without significant computational cost and then to use the model in more challenging applications without the need for recalibration. The calibration results were also tested for the different values of the cavitation number and they were not affected, thus making it clear that the values of the empirical coefficients are not heavily dependent on the variation of σ. These empirical factors seem to have stronger dependency to the used solver than to the geometry and flow, under the condition that they have been scaled to account for the mean flow and the geometry scale as in the present study. As far as the cavitation number σ is concerned, it was determined that for high and moderate values of σ the numerical results show exceptional agreement with the experimental data. In the case of more intense cavitation phenomena, although the model can reproduce the expected increase in intensity of the cavitating flow, there is a drop-off in the prediction accuracy.

As a final note, some recommendations are presented for different paths that future research could follow on the subject of cavitation modeling. The further research ideas include the following:

- It is recommended to implement another volume fraction equation into the equations system, namely the non-condensable gas volume fraction equation. This equation models the dissolved nuclei inside the liquid and the Kunz mass transfer terms also account for it. The assessment of the impact of the third phase in comparison to the simpler two-phase model used in the present study would be of significant interest.
- Another possible consideration regarding the modeling is the implementation of a different cavitation model based on the Rayleigh-Plesset equation and to observe differences between the two types of approaches.
- As far as the twisted three-dimensional hydrofoil is concerned, it would be interesting to test the different available correction methods to the RANS equations in an attempt to limit viscosity overproduction and thus improve the prediction accuracy of unsteady sheet cavitation.

- Another possible investigation area is the influence of the turbulence model in simulations with marine propellers, especially for high values of the advance coefficient. Previous study with MaPFlow documented that the predictions of the hydrodynamic characteristics is improved for these values of J with the use of the $\gamma - Re_\theta$ model. Further investigation is needed to assess its impact in cavitating flows.
- From a marine hydrodynamics perspective, the main topic of interest is ship propeller cavitation, where the effect of the ship wake plays a crucial role in the developed cavitation pattern. A recommendation for further studies would be to simulate a cavitating flow taking the effect of the ship wake into account.
- Last but not least, one of the most dangerous side effects of the cavitation phenomenon is the erosion of the propeller blades that it causes. Computational methods have been developed to predict the erosion due to cavitation. Consequently, a coupling of the present cavitation inception prediction algorithm with a method to predict erosion is a very interesting research path that would allow the full assessment of the danger of cavitation in various marine propellers.

8 Bibliography

[1] Janyce Franc and J. M. Michel. "Fundamentals of Cavitation". In: 2004.

[2] J.S. Carlton. *Marine propellers and propulsion*. Jan. 2018, pp. 1–585. DOI: 10.1016/C2014-0-01177-X.

[3] G.K. Politis. "Ship Resistance and Propulsion". In: *National Technical University of Athens* (2018).

[4] Janyce Franc. "Physics and Control of Cavitation". In: (2006).

[5] Christopher Brennen. "Cavitation and Bubble Dynamics". In: *Cavitation and Bubble Dynamics* 44 (Jan. 1995). DOI: 10.1017/CBO9781107338760.

[6] G. Kuiper. "Cavitation in Ship Propulsion-Course Notes". In: *Technical University of Delft* (2010).

[7] Prof. Dr. Ir. G.Kuiper. "Resistance and Propulsion of Ships". In: *Technical University of Delft* (1994). DOI: CourseMT512.

[8] https://www.hsva.de/our-facilities/cavitation-tunnels.html. "HSVA Conventional Cavitation Tunnels". In: ().

[9] ITTC Recommended Procedures and Guidelines. "Cavitation Induced Erosion on Propellers, Rudders and Appendages - Model Scale Experiments". In: (2011).

[10] Foivos Koukouvinis and Manolis Gavaises. "Cavitation and Bubble Dynamics - Fundamentals and Applications". In: (2021).

[11] Mitja Morgut. "Predictions of Non-Cavitating and Cavitating Flow on Hydrofoils and Marine Propellers by CFD and Advanced Model Calibration". Universita Degli Studi Di Udine. PhD thesis. 2012.

[12] Robert F. Kunz et al. "A preconditioned Navier–Stokes method for two-phase flows with application to cavitation prediction". In: *Computers and Fluids* 29.8 (2000), pp. 849–875. ISSN: 0045-7930. DOI: https://doi.org/10.1016/S0045-7930(99)00039-0. URL: https://www.sciencedirect.com/science/article/pii/S0045793099000390.

[13] Charles L. Merkle, Jian Feng, and Philip E. O. Buelow. "Computational modeling of the dynamics of sheet cavitation". In: (1998).

[14] Inanc Senocak and Wei Shyy. "Interfacial dynamics-based modelling of turbulent cavitating flows, Part-1: Model development and steady-state computations". In: *International Journal for Numerical Methods in Fluids* 44 (Mar. 2004), pp. 975–995. DOI: 10.1002/fld.692.

[15] J. Sauer and Günter Schnerr Professor Dr.-Ing.habil. "Unsteady cavitating flow - A new cavitation model based on a modified front capturing method and bubble dynamics". In: *Proceedings of 2000 ASME Fluid Engineering Summer Conference* 251 (Jan. 2000), pp. 1073–1079.

[16] Philip Zwart, A.G. Gerber, and Thabet Belamri. "A two-phase flow model for predicting cavitation dynamics". In: *Fifth International Conference on Multiphase Flow* (Jan. 2004).

[17] Ashok Singhal et al. "Mathematical Basis and Validation of the Full Cavitation Model". In: *Journal of Fluids Engineering-transactions of The Asme - J FLUID ENG* 124 (Sept. 2002). DOI: 10.1115/1.1486223.

[18] Giorgos Papadakis. "Development of a Hybrid Compressible Vortex Particle Method and Application to External Problems Including Helicopter Flows". National Technical University of Athens. PhD thesis. 2014.

[19] C. Hirt and B Nichols. "Volume of Fluid (VOF) Method for the Dynamics of Free Boundaries". In: *Journal of Computational Phys., 39:201–225* (1981).

[20] S. V. Patankar and D. B. Spalding. "A Calculation Procedure for Heat, Mass and Momentum Transfer in Three-Dimensional Parabolic Flows". In: *Int. J. Heat Mass Transf., 15:1787–1806* (1972).

[21] R. I. Issa, A. D. Gosman, and A. P. Watkings. "The Computation of Compressible and Incompressible Recirculating Flows by a Non-Iterative Implicit Scheme". In: *J. Comput. Phys, 62:66–82* (1986).

[22] A.J. Chorin. "A Numerical Method for Solving Incompresible Viscous Flow Problems". In: *Journal of Computational Physics,12-26* (1967).

[23] Jiri Blazek. "Computational Fluid Dynamics: Principles and Applications". In: *3rd Edition* (2015).

[24] Dimitris Ntouras and George Papadakis. "A Coupled Artificial Compressibility Method for Free Surface Flows". In: *Journal of Marine Science and Engineering* 8.8 (2020).

ISSN: 2077-1312. DOI: 10.3390/jmse8080590. URL: https://www.mdpi.com/2077-1312/8/8/590.

[25] Leonard B.P. "Simple high-accuracy resolution program for convective modelling of discontinuities". In: *Int. J. Numer. Methods Fluids, 8:1291–1318* (1988).

[26] P.L. Roe. "Approximate Riemann Solvers, Parameter Vectors and Difference Schemes". In: *Journal of Computational Physics,357-372* (1981).

[27] R. Biedron, V. Vatsa, and H. Atkings. "Simulation of unsteady flows using an unstructured Navier-Stokes solver on moving and stationary grids". In: *In Proceedings of the 23rd AIAA Applied Aerodynamics Conference, pages 1–17* (2005).

[28] F.R. Menter. "Two-Equation Eddy Viscosity Turbulence Models for Engineering Applications". In: *AIAA Journal,32:1598-1605* (1994).

[29] Sobhi Frikha, Oliver Coutier-Delgosha, and Jacques Andres Astolfi. "Influence of the Cavitation Model on the Simulation of Cloud Cavitation on 2D Foil Section". In: *International Journal of Rotating Machinery* (2008).

[30] Mitja Morgut, Enrico Nobile, and Ignacijo Biluš. "Comparison of mass transfer models for the numerical prediction of sheet cavitation around a hydrofoil". In: *International Journal of Multiphase Flow 37 620–626* (2011).

[31] Mitja Morgut and Enrico Nobile. "Influence of the Mass Transfer Model on the Numerical Prediction of the Cavitating Flow Around a Marine Propeller". In: *Second International Symposium on Marine Propulsors, Hamburg, Germany* (2011).

[32] Zhou et. al. "An Efficient Calibration Approach for Cavitation Model Constants Based on OpenFOAM Platform". In: *Journal of Marine Science and Technology,24:1043-1056* (2019). DOI: https://doi.org/10.1007/s00773-018-0604-9.

[33] Venkateswaran S., Deshpande M., and Merkle C.L. "The application of preconditioning to reacting flow computations". In: *AIAA Paper 95-1673 from Proceedings of the 12th AIAA Computational Fluid Dynamics Conference* (1995).

[34] Chenzhou Lian, Guoping Xia, and Charles L. Merkle. "Impact of source terms on reliability of CFD algorithms". In: *Computers and Fluids 39 1909–1922* (2010).

[35] Youcef Ait Bouziad. "Physical Modelling of Leading Edge Cavitation: Computational Methodologies and Application to Hydraulic Machinery". École Polytechnique Federale de Lausanne. PhD thesis. 2006.

[36] Marko Pezdevšek, Ignacijo Biluš, and Gorazd Hren. "Comparison of cavitation models for the prediction of cavitation around a hydrofoil". In: *Journal of Energy and Technology Volume 14 p.p. 41-55* (2021).

[37] Terry Brockett. "Minimum Pressure Envelopes for Modified NACA-66 Sections with a=0.8 Camber and Buships Type I and Type II Sections". In: *California Institute of Technology* (1966).

[38] Rickard Bensow. "Simulation of the unsteady cavitation on the the Delft Twist11 foil using RANS, DES and LES". In: *Second International Symposium on Marine Propulsors, Hamburg, Germany* (June 2011).

[39] Da-qing Li, Mikael Grekula, and Per Lindell. "Towards numerical prediction of unsteady sheet cavitation on hydrofoils". In: *9th International Conference on Hydrodynamics, Shanghai, China* (October 11-15, 2010).

[40] Reboud J. L., Stutz B., and Coutier O. "Two-Phase flow structure of cavitation: Experiment and modeling of unsteady effects". In: *3rd International Symp. on Cavitation, Grenoble, France.* (1998).

[41] Johansen S. T., Wu J., and Shyy W. "Filter-based unsteady RANS computations". In: *International Journal of Heat and fluid flow , 25(1): 10-21* (2004).

[42] Huang Biao, Wang Guo-yu, and Zhao Yu. "Numerical simulation unsteady cloud cavitating flow with a filter-based density correction model". In: *Journal of Hydrodynamics, 26(1): 26-36* (2014).

[43] Shijie Zhang et al. "A new turbulent viscosity correction model with URANS Solver for unsteady turbulent cavitation flow computations". In: *Journal of Fluids Engineering* (2022).

[44] Abolfazl Asnaghi. "Developing Computational Methods for Detailed Assessment of Cavitation on Marine Propellers". Chalmers University of Technology. PhD thesis. June 2015. DOI: 10.13140/RG.2.1.3817.6480.

[45] Stewart Whitworth. "Cavitation prediction of flow over Delft Twist11 foil". In: *Second International Symposium on Marine Propulsors, Hamburg, Germany* (June 2011).

[46] Vaz, Lloyd, and Gnanasundaram. "Improved modeling of sheet cavitation dynamics on Delft Twist11 hydrofoil". In: *VII International Conference on Computational Methods in Marine Engineering* (2017).

[47] A.H. Koop. "Numerical Simulation of Unsteady Three-Dimensional Sheet Cavitation". University of Twente. PhD thesis. 2008.

[48] D.F. de Lange and G.J. de Bruin. "Sheet Cavitation and Cloud Cavitation, Re-entrant Jet and Three-Dimensionality". In: *Applied Scientific Research, 58:91–114* (1998).

[49] Evert-Jan Foeth. "The Structure of Three-Dimensional Sheet Cavitation". Delft University of Technology. PhD thesis. 2008.

[50] E.J. Foeth and T. van Terwisga. "The Structure of Unsteady Cavitation. Part 1: Observations of an Attached Cavity on a Three-Dimensional Hydrofoil". In: *Sixth International Symposium on Cavitation, Wageningen* (2006).

[51] "Explanation with the experimental data for the "Delft Twist 11" Foil Test case". In: *http://maritimetechnology.tudelft.nl/SHS/* (19-01-2010).

[52] "Proceedings of the Workshop on Cavitation and Propeller Performance, Case 1: Cavitation on foil". In: *Second International Symposium on Marine Propulsors* (6-2011). DOI: http://marinepropulsors.com/proceedings-2011.php.

[53] "1st international workshop on cavitating propeller performance". In: *https://www.sva-potsdam.de/en/pptc-smp11-workshop/* (18-06-2011).

[54] K.N. Kalantzis. "Numerical Simulation of propeller open water characteristics using CFD". In: *National Technical University of Athens* (2020).

[55] Mitja Morgut and Enrico Nobile. "Numerical Predictions of the Cavitating and Non-Cavitating Flow around the Model Scale Propeller PPTC". In: *Second International Symposium on Marine Propulsors, Hamburg, Germany* (June 2011).

[56] Sergey Yakubov et.al. "Cavitation Simulations of the Potsdam Propeller Test Case". In: *Second International Symposium on Marine Propulsors, Hamburg, Germany* (June 2011).

[57] Keita Fujiyama et al. "Performance and Cavitation Evaluation of Marine Propeller using Numerical Simulations". In: *Second International Symposium on Marine Propulsors, Hamburg, Germany* (June 2011).